^{87}Rubidium Bose-Einstein Condensates in Optical Lattices

by

Gretchen K. Campbell

Submitted to the Department of Physics
in partial fulfillment of the requirements for the degree of

Doctor of Philosophy

at the

MASSACHUSETTS INSTITUTE OF TECHNOLOGY

September 2006

Author .....
Department of Physics
September, 2006

Certified by .....
Wolfgang Ketterle
John D. MacAurthur Professor of Physics
Thesis Supervisor

Certified by .....
David E. Pritchard
Cecil and Ida Green Professor of Physics
Thesis Supervisor

Accepted by .....
Thomas J. Greytak
Professor of Physics, Associate Department Head for Education

^{87}Rubidium Bose-Einstein Condensates in Optical Lattices

by

Gretchen K. Campbell

Submitted to the Department of Physics
on September, 2006, in partial fulfillment of the
requirements for the degree of
Doctor of Philosophy

Abstract

Bose-Einstein condensates in optical lattices have proven to be a powerful tool for studying a wide variety of physics. In this thesis a series of experiments using optical lattices to manipulate ^{87}Rb Bose-Einstein condensates are described.

A systematic shift of the photon recoil momentum due to the index of refraction of a dilute gas of atoms has been observed. The recoil frequency was measured interferometrically using a two-pulse Ramsey interferometer. The two pulses were created using a one dimensional optical lattice. By measuring the resulting frequency as a function of the lattice detuning from the atomic resonance, we found a distinctive dispersive shape for the recoil frequency that fit the recoil momentum as $n_r\hbar k$.

A one-dimensional optical lattice was used to modify the dispersion relation of the condensate in order to demonstrate the matter-wave analogue of Optical Parametric Generation (OPG) and Amplification (OPA) of photons. A condensate was loaded into a moving optical lattice with adjustable quasimomentum k_0. As the value for k_0 was varied, we observed elastic scattering into two distinct final momentum states k_1 and k_2. When a small fraction of atoms was first transferred to k_1 before ramping on the lattice, we observed the amplification of scattered atoms into k_1 and k_2.

The superfluid-Mott Insulator transition was studied using microwave spectroscopy in a deep three-dimensional optical lattice. Using the density dependent clock shift we were able to spectroscopically distinguish sites with different occupation numbers, and to directly image sites with occupation number from 1 to 5, revealing the shell structure of the Mott Insulator phase.

Thesis Supervisor: Wolfgang Ketterle
Title: John D. MacAurthur Professor of Physics

Thesis Supervisor: David E. Pritchard
Title: Cecil and Ida Green Professor of Physics

Acknowledgments

During my time at MIT, there are a number of people who have improved my life both inside and outside the lab. From my early days at MIT, the Ketterle-Pritchard group functioned as a family, albeit a slightly dysfunctional one, and I have received a tremendous amount of help and support during my time here.

First, I'd like to thank my advisors, Wolfgang Ketterle and Dave Pritchard. Dave and Wolfgang have very different advising styles, and I've benefited greatly from each of them. Wolfgang has a wonderful ability to make almost anything seem exciting and important. Whenever I was feeling discouraged a few minutes in Wolfgang's office would leave me feeling inspired and ready to jump back into the lab. Even today, when I hear him talking to prospective students it makes me want to join his group all over again.

I've spent many hours in Dave's office discussing physics, as well as a wide variety of other topics. I've both enjoyed and learned quite a bit during these conversations, and have appreciated his frank advice other the years. Dave can always tell when your glossing over details you don't understand, and makes sure you do the end of the conversation. Dave also gave me the opportunity to crew on his sailboat. Not only did this get me out of the lab and into the sun for a few hours each week, but race day was by far my favorite day. I'll miss sailing a great deal out in landlocked Boulder.

When I joined the Rubidium lab, back in the fall of 2001, the lab was just barely one year old. I had the benefit of joining a great group of people: Yoshio Torii, Dominik Schneble, Micah Boyd, Erik Streed and Pavel Gorelik. My early days in the lab were spent working with Dominik Schneble. Dominik took me under his wing, taught me the ways of the lab, and was always full of encouragement and support. He was also great fun to work, I have fond memories of his rapping skills, the days when we spoke only in rhyme, and his awesome use of "Natural voices".

During my time at MIT, I've overlapped the most with Micah Boyd. Micah has been both a great labmate and a great friend. I can't imagine what my experience

would have been like without him. Given the right supplies Micah can fix almost anything, and usually in very creative ways. Micah could always tell when I was having a bad day, and did his best to fix it. I can't thank him enough for his help, support, procrastination ideas and fashion advice, both inside and outside the lab.

Erik Streed has an encyclopedic knowledge of all things physics. Whenever I wanted to know where to look things up, or where to find an obscure part Erik could always point me in the right direction. Erik has a unique way of approaching physics and life in general. My skills as a physicists, and problem solver in general were increased through my interactions with Erik.

A year after I arrived at MIT, Jongchul Mun joined the rubidium lab. Jongchul and I have spent many marathon nights in the lab together. Jongchul is a careful scientist and an excellent running mate, in addition to having a great laugh. I've enjoyed all of our nights watching baseball in the lab, and have a particular fondness for the long nights we spent during the lattice experiments, where we watched live broadcasts of Korean baseball at 5 am in the morning. The most recent addition to the group is Patrick Medley, Patrick brought a huge amount of enthusiasm and energy into the lab. Under Jongchul and Patrick's leadership I'm sure the Rubidium lab will have much success in the future. I'd also like to thank Luis Marcassa, who has spent the last year here on sabbatical. Luis is an incredibly friendly guy, and was willing to do almost anything in order to help out the lab.

In my first years at MIT I benefited from great advice from Ananth Chikkatur, Deep Gupta, and Zoran Hadzibabic, and I was always impressed with Johnny Vogels excitement and enthusiasm. When I first started working late in the lab, every night either Jamil Abo-Shaeer or Aaron Leanhardt would appear and make sure I got home safe. For three years one of them always made sure to either drive or walk me home. Aaron Leanhardt has been a good friend over the years, to the extent of even joining the Rubidium lab. I learned a great deal from him about how to be a scientist, and the recent successes in the Rubidium lab would not have happened without him.

Jamil Abo-Shaeer is the big brother I always wished for. Jamil looked out for me, and made building 26 a fun place to be. Since his graduation the hallway has been a

much quieter (though safer) place to be. Jamil is a good friend and continues to help me in countless ways.

Tom Pasquini has been an excellent officemate, and never once complained about my messy desk. Tom is a good friend, and I've appreciated his sense of humor. He has always helped me to keep things in context and I'll miss our discussions. His handiwork never ceases to amaze me, and he also deserves my gratitude for helping to convince MIT to pay for our health insurance. Dan Miller has taken on the role of group party thrower, as well as all around instigator. From his April Fools day jokes, to his Eco-Dan fall foliage tour, he's helped keep group morale high. I look forward to hiking with Dan (and singing his name) out in Colorado.

Whenever I needed someone to be either incredibly happy or incredibly angry on my behalf, I could always count on Martin Zweirlein. Martin is an amazing scientist and I've enjoyed our countless coffee breaks over the years. His passion for physics is second to none, and I'm glad the hallway will not be without his good cheer for long. Michelle Saba was always full of thoughtful advice and feedback, and was always available to talk physics. He was an invaluable resource for the group, and his presence both on the hallway, and on the soccer field are missed.

Christian Schunck is by far one of the nicest people I know, and his presence has brought a much needed civility to the Lithium lab. In this regard his nemesis would be Andre Shirotzek, Andre has the distinction of being the only graduate student in the group to have his own online fan club. Andre is a great guy, and he's introduced me to a lot of great music which helped to produce this thesis. I shared a memorable trip to Barcelona, with Claudiu Stan, Yong-Il Shin, and Takashi Mukayiama, and had a great time wandering the streets of Barcelona with them.

If the Ketterle-Pritchard group was like a family, the late Carol Costa was our surrogate mother. Carol looked out for everyone, she was always in tune to how people were feeling, and made sure everyone was taken care of. Carol is deeply missed within the group.

I'd also like to thank a few other people with whom I've interacted in the group: Ellenor Emery Barish, Caleb Christensen, Gyu-Boong Jo, Joanna Keseberg, Yingmei

Liu, Sebastian Will, Kaiwen Xu and Peter Zarth. I'd also like to thank the RLE support staff, and in particular Al McGurl and Bill Gibbs. Al and Bill have always been helpful and friendly over the years and have helped us out of many jams.

Much of my first year at MIT was spent doing problem sets and studying for general exams with Cort Johnson, and Qudsia Jabeen Ejaz. Without their help and assistance these times would have been much more difficult, and much less fun. I wish them both the best of luck in the future.

I spent my undergraduate years at Wellesley College where during my first semester I had Ted Ducas as a lab instructor. Ted's excitement about physics was contagious, and when I later decided to major, he became my undergraduate advisor. I thank Ted for both steering me towards ultracold atoms, and for encouraging me to apply to MIT. During my time at MIT, I've enjoyed our Friday afternoon discussions immensely.

During my years at Wellesley, I also had the good fortune of meeting Rachel Lomasky. During large periods of my graduate school career Rachel was the only person I consistently saw outside the lab. Rachel helped to keep me sane, kidnapped me away from the lab when I really needed it, and never got offended when I disappeared and didn't return her calls for months.

Finally, I'd like to thank my family, particulary my sister Heather and her partner Tracy. Whenever I needed a break I could always retreat to their home, they have been a constant source of support and encouragement for me.

Contents

List of Figures

Chapter 1

Introduction

It has been over a decade now since the first experimental observation of Bose-Einstein condensation (BEC) in dilute atomic clouds. The advent of BEC opened up a variety of new research areas. In the early years after the first demonstration of BEC, experiments were focused on studying the fundamental properties of condensation and superfluidity, however today BEC is instead being used as a springboard for studying a number of fields including atom optics, in particular nonlinear atom optics, quantum measurement problems, precision measurements using atom interferometry, and most recently as a quantum simulator to model more complicated condensed matter systems.

Given the large number of theses which have preceded this work, as well as the vast number of review papers and books now available on the subject, for the purposes of this thesis I will limit my introduction of BEC to those aspects which are relevant to the work described here. For a more detailed introduction to Bose-Einstein condensation, and the laser cooling and trapping methods used to realize it, I refer to earlier theses [105, 55], review articles [18, 64, 88, 20, 72, 65], and books [92, 98] on the subject.

1.1 The BEC Phase Transition

The phase transition to Bose-Einstein condensation occurs when there is a macroscopic occupation of a single quantum state, where the quantum state is either the ground state, or a long-lived metastable state. One can think of a Bose-Einstein Condensate as a giant matter wave. For a uniform gas of atoms with number density n, and at temperature T, the spatial extent of an atom can be described by its deBroglie wavelength which is given by

$$\lambda_{dB} = \frac{h}{\sqrt{2\pi m k_B T}}, \tag{1.1}$$

where h is Planck's constant, m is the atomic mass, and k_B is the Boltzmann constant. At room temperature, the deBroglie wavelength is typically much shorter than the interparticle spacing of the atoms, $n^{-1/3}$. However, as the temperature of the gas decreases, the wavelength increases until $n^{-1/3} \approx \lambda_{dB}$, at this point the atoms start to overlap and the system undergoes a phase transition to a Bose-Einstein condensate. We can no longer think of the atoms as being distinguishable and instead there is a single matter wave created by the overlap of all the individual atoms. One can also describe the transition in terms of the phase space density of the gas, $\rho = n\lambda_{dB}^3$, the phase transition to condensation occurs when $\rho \approx 1$.

1.2 Noninteracting Bosons in a Harmonic Trap

For N noninteracting Bosons trapped in an external 3D harmonic trap, with

$$V_{ext} = \frac{m}{2}\left(\omega_x^2 x^2 + \omega_y^2 y^2 + \omega_z^2 z^2\right), \tag{1.2}$$

where ω_i is the trap frequency in the i^{th} direction. The energy levels are given by

$$\epsilon(n_x, n_y, n_z) = \left(n_x + \frac{1}{2}\right)\hbar\omega_x + \left(n_y + \frac{1}{2}\right)\hbar\omega_y + \left(n_z + \frac{1}{2}\right)\hbar\omega_z. \tag{1.3}$$

In the condensed state, the atoms are all in the ground state of the system, and the macroscopic wavefunction for the system is given by $\Phi(\vec{r}_1, ..., \vec{r}_N) = \prod_i \phi_0(\vec{r}_i)$, where

$$\phi_0(\vec{r}) = \left(\frac{m\omega_{ho}}{\pi\hbar}\right)^{3/4} e^{-\frac{m}{2\hbar}(\omega_x x^2+\omega_y y^2+\omega_z z^2)} \tag{1.4}$$

and ω_{ho} is the geometric mean of the trap frequencies. The density distribution is $n(\vec{r}) = N|\psi_0(\vec{r})|^2$ and the radius of the condensate is given by the harmonic oscillator length

$$a_{ho} = \left(\frac{\hbar}{m\omega_{ho}}\right)^{1/2}. \tag{1.5}$$

For noninteracting bosons in thermal equilibrium the average number of particles in a given state can be found using the Bose-Einstein distribution,

$$\langle n(\epsilon)\rangle = \frac{1}{e^{(\epsilon-\mu)/k_B T} - 1} \tag{1.6}$$

where $\langle n(\epsilon)\rangle$ gives the number of particles in the energy level ϵ, μ is the chemical potential of the gas and $\sum_i \langle n(\epsilon)\rangle = N$. For large N, and harmonically confined atoms, this gives a transition temperature of

$$k_B T_c = \hbar\omega_{ho} \left(N/\zeta(3)\right)^{1/3} \tag{1.7}$$

where $\zeta(3)$ ≈1.202 is the Riemann Zeta function. The number of atoms in the condensate N_0, at temperature T is given by

$$N_0 = N\left[1 - \left(\frac{T}{T_C}\right)^3\right]. \tag{1.8}$$

1.3 Atom-Atom Interactions

In the previous section a noninteracting gas of bosons was assumed, however in experiments with alkali atoms this is not the case. Instead atom-atom interactions have to be taken into consideration. Although atom-atom interactions do not significantly effect the transition temperature or the condensate fraction, they do effect the density

distribution of the cloud, as well as the properties of the condensate. In fact, all of the work described in this thesis is due to these interactions.

1.3.1 S-wave Collisions

For the typical densities used in BEC experiments with alkali gases (typically between $10^{12}/cm^3$ to $10^{15}/cm^3$), one must only consider two-body interactions, and in addition at ultracold temperatures only s-wave collisions can occur. For two particles with identical mass m, the interaction can be described by a delta function potential where the potential is given by

$$U(r) = \frac{4\pi\hbar^2 a_s}{m}\delta(r), \tag{1.9}$$

and a_s is the s-wave scattering length [92].

1.4 Weakly Interacting Bosons

The effect of s-wave collisions is to add a nonlinear term to the normal Schrödinger equation. The effective Hamiltonian for the system is

$$H = \sum_{i=1}^{N}\left[\frac{\vec{p}_i^2}{2m} + V(\vec{r}_i)\right] + \frac{4\pi\hbar^2 a_s}{m}\sum_{i<j}\delta(\vec{r}_i - \vec{r}_j), \tag{1.10}$$

and the energy of the system is given by

$$E = N\int dr\left[\frac{\hbar^2}{2m}|\nabla\phi(\vec{r})|^2 + V(\vec{r})|\phi(\vec{r})|^2 + \frac{(N-1)}{2}\frac{4\pi\hbar^2 a_s}{m}|\phi(\vec{r})|^4\right]. \tag{1.11}$$

As in the noninteracting case, in the condensed state all of the atoms occupy the ground state of system, therefore the macroscopic wavefunction is still described by $\Psi(\vec{r}_1, \vec{r}_2, ..., \vec{r}_N) = \prod_{i=1}^{N}\phi(\vec{r}_i)$. Defining $\psi(\vec{r}) = \sqrt{N}\phi(\vec{r})$, the density of condensate is given by $n(\vec{r}) = |\psi(\vec{r})|^2$, and Eq. (1.11) can be rewritten as

$$E = \int dr\left[\frac{\hbar^2}{2m}|\nabla\psi(\vec{r})|^2 + V(\vec{r})|\psi(\vec{r})|^2 + \frac{4\pi\hbar^2 a_s}{2m}|\psi(\vec{r})|^4\right] \tag{1.12}$$

where $(N-1) \approx N$ for large N.

1.4.1 The Density Distribution

A Variational Approach

In the noninteracting case, the ground state wavefunction was given by Eq. (1.4). Using Eq. (1.12) we can use a variational approach to find a new ground state wavefunction for the interacting system. Defining the trial wavefunction

$$\psi(r) = \sqrt{N}\left(\frac{m\omega_r}{\pi\hbar}\right) e^{-m\omega_r r^2/2\hbar}, \tag{1.13}$$

where ω_r is the variational parameter, and where for simplicity we have assumed an isotropic harmonic trap with trap frequency ω_{ho}. Substituting Eq. (1.13) into Eq. (1.12), and integrating we find

$$E(\omega_r, \omega_{ho}) = N\hbar\left[\frac{3}{4}\left(\omega_r + \frac{\omega_{ho}^2}{\omega_r}\right) + Na_s\sqrt{\frac{m\omega_r^3}{2\pi\hbar}}\right] \tag{1.14}$$

minimizing this with respect to ω_{ho}, and rewriting in terms of the harmonic oscillator length $a_{ho} = \sqrt{\frac{\hbar}{m\omega_{ho}}}$, we find

$$\frac{a_r}{a_{ho}} = \left[1 + \frac{Na_s}{a_r}\sqrt{\frac{2}{\pi}}\right]^{1/4}. \tag{1.15}$$

Fig. 1-1 shows this ratio for typical trap parameters as the condensate number N is increased.

Thomas-Fermi Approximation

Alternatively for fixed μ, if $E - \mu N$ is minimized using Eq. (1.12), the result is the time-independent Gross-Pitaevskii equation

$$\left(-\frac{\hbar^2}{2m}\nabla^2 + V(\vec{r}) + \frac{4\pi\hbar^2 a_s}{m}|\psi(\vec{r})|^2\right)\psi(\vec{r}) = \mu\psi(\vec{r}). \tag{1.16}$$

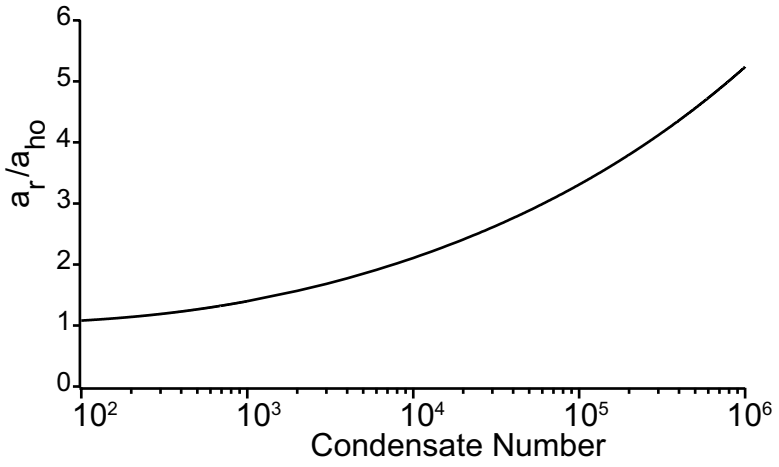

Figure 1-1: Variational calculation of the change in the ground state wavefunction due to interactions. The radius is given with respect to the harmonic oscillator length a_{ho}, the radius of the condensate in the noninteracting case. The radius is found for $\omega_{ho} = 2\pi \times 100\text{Hz}$.

As was derived in the variation approach, for large N the ratio of the kinetic energy to the interaction energy

$$\frac{E_{kin}}{E_{int}} \propto \frac{a_h o}{N|a_s|} \tag{1.17}$$

is very small. Therefore, in the Thomas-Fermi approximation, the kinetic energy term is ignored and the Gross-Pitaevskii equation becomes

$$\mu\psi(\vec{r}) = \left[V(\vec{r}) + \frac{4\pi\hbar^2 a_s}{m}|\psi(\vec{r})|^2\right]\psi(\vec{r}). \tag{1.18}$$

The density of the condensate is given by

$$n(r) = |\psi(\vec{r})|^2 = \frac{m}{4\pi\hbar^2 a_s}\left[\mu - V(\vec{r})\right]. \tag{1.19}$$

For the harmonic potential given in Eq. (1.2), one has a parabolic density distribution, where the Thomas-Fermi radius in the i^{th} direction is given by $R_i = \frac{2\mu}{m\omega_i}$

1.5 The Excitation Spectrum

1.5.1 The Bogoliubov Approximation

Having found the ground state wavefunction of the condensate in a weakly interacting system, we can next derive the excitation spectrum for the condensate. To show this we again start with the hamiltonian for the system given in Eq. (1.10). However, instead of writing the Schrodinger equation in terms of the condensate wavefunction, we instead write the Hamiltonian in terms of the creation and annihilation operators for bosons, $\hat{\psi}^\dagger(\vec{r})$ and $\hat{\psi}(\vec{r})$

$$H = \int d\vec{r} \left[-\hat{\psi}^\dagger(\vec{r}) \frac{\hbar^2}{2m} \nabla^2 \hat{\psi}(\vec{r}) + V(\vec{r}) \hat{\psi}^\dagger(\vec{r}) \hat{\psi}(\vec{r}) + \frac{U_0}{2} \hat{\psi}^\dagger(\vec{r}) \hat{\psi}^\dagger(\vec{r}) \hat{\psi}(\vec{r}) \hat{\psi}(\vec{r}) \right], \quad (1.20)$$

where $U_0 = \frac{4\pi\hbar^2 a_s}{m}$. To find the excitation spectrum, we include fluctuations in the ground state of the wavefunction by defining

$$\hat{\psi}(\vec{r}) = \psi(\vec{r}) + \delta\hat{\psi}(\vec{r}), \quad (1.21)$$

the average value of the operator plus a small fluctuation term. Using the Heisenberg equation of motion for the operator,

$$\imath\hbar \frac{\partial}{\partial t} \hat{\psi}(\vec{r}) = [\hat{\psi}(\vec{r}), \hat{H}] = \left(-\frac{\hbar^2 \nabla^2}{2m} + V(\vec{r}) + U_0 \hat{\psi}^\dagger(\vec{r}) \hat{\psi}(\vec{r}) \right) \hat{\psi}(\vec{r}), \quad (1.22)$$

and linearizing this equation for $\hat{\psi}(\vec{r})$ in terms of $\delta\hat{\psi}(\vec{r})$ gives a set of linear coupled equations for $\delta\hat{\psi}(\vec{r})$. This coupled equation is given by

$$\imath\hbar \frac{\partial}{\partial t} \delta\hat{\psi}(\vec{r}) = \left(-\frac{\hbar^2}{2m} \nabla^2 + V(\vec{r}) \right) \delta\hat{\psi}(\vec{r}) + U_0 \delta\hat{\psi}^\dagger(\vec{r}) \delta\hat{\psi}^2(\vec{r}) + 2U_0 |\psi^2(\vec{r})| \delta\hat{\psi}(\vec{r}), \quad (1.23)$$

and similarly for the hermitian conjugate $\delta\hat{\psi}^\dagger(\vec{r})$. The normal mode solutions can be found from these coupled equations, and as shown by Bogoliubov for a uniform gas

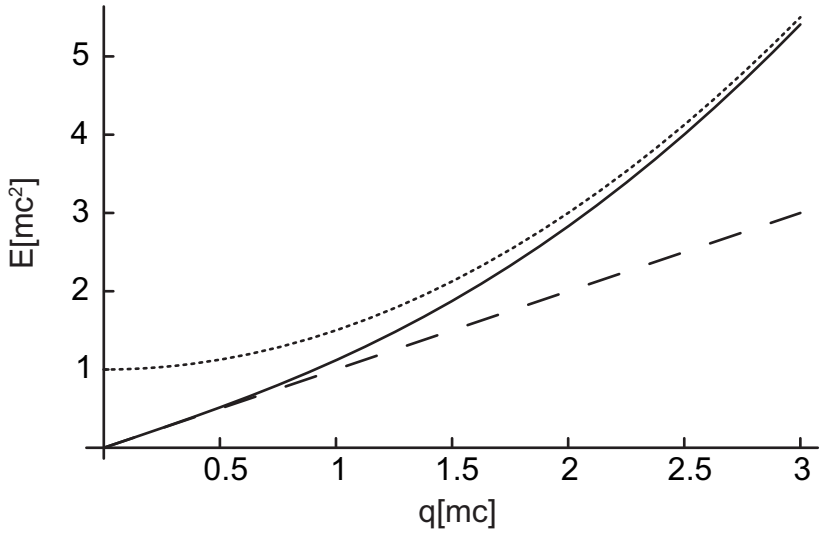

Figure 1-2: Excitation spectrum for the condensate. The dispersion relation for a condensate (solid line), free particles (dotted line), and for phonons (dashed line) is shown. The free particle cure is offset by mc^2. The momentum is in units of $q = mc$, where c is the speed of sound in the condensate.

with $V(\vec{r})$, the Bogoliubov equations become

$$\begin{pmatrix} \epsilon_q + nU_0 - \hbar\omega_q & -nU_0 \\ -nU_0 & \epsilon_q + nU_0 + \hbar\omega_q \end{pmatrix} \begin{pmatrix} u_q \\ v_q \end{pmatrix} = 0, \tag{1.24}$$

where $\epsilon_q = \hbar^2 q^2/2m$ and

$$\delta\hat{\psi}(\vec{r}) = e^{-i\mu t/\hbar} \sum_j \left(u_j(\vec{r})\hat{\alpha}_j e^{-i\omega_j t} + v_j^*(\vec{r})\hat{\alpha}_j^\dagger e^{i\omega_j t} \right), \tag{1.25}$$

where $\alpha_j(^\dagger)$ annihilate (create) bosonic excitations in the normal mode with frequency ω_j. Eq. (1.24) yields the dispersion relation

$$\hbar\omega_q = \sqrt{\epsilon_q^2 + 2nU_0\epsilon_q}. \tag{1.26}$$

As shown in Fig. (1-2) for low momenta, the excitations are phonon like with $E = \hbar kc$ where $c = \sqrt{\frac{nU_0}{m}}$ is the speed of sound in the condensate. For large momenta the excitations are particle like with $E = \epsilon_q + nU_0$.

1.6 BECIV "The Rubidium Lab"

The experiments presented in this thesis were all performed in BECIV, the "Rubidium Lab", the newest of the BEC machines in the Ketterle-Pritchard group. To create Bose-Einstein condensates, one requires ultrahigh vacuum, a stable laser system, and high magnetic fields. The magnetic coils and optics necessary to trap and cool the atoms greatly limits the optical access to the condensate, and the stringent requirements of high vacuum also make switching experiments inside the chamber difficult and time consuming. To overcome these challenges, a new Rubidium Bose-Einstein condensate apparatus was built. The goal of the new lab was to build an apparatus which created condensates in a "production chamber" and then transported them to an auxiliary chamber. The second chamber would allow for better optical access and also allow for the exchange of experiments without breaking vacuum in the main production chamber.

I arrived at MIT in the fall of 2001, just a few months before BECIV realized its first condensate. Building a rubidium BEC apparatus which could both create, and transport condensates posed some unexpected technical difficulties. My early days in the lab focused on optimizing the performance of the new apparatus and implementing the transport of the condensates to the auxiliary chamber. As detailed accounts of the design and construction of the machine can be found in Ref.[111, 110], here I will just highlight some important features of our machine.

Although the majority of Rubidium experiments use double MOTs loaded using either a dispenser or a vapor cell, our machine instead uses an oven and Zeeman slower to load the MOT. The atoms are then loaded into a Ioffe-Pritchard Magnetic trap. After optimizing the performance of the apparatus, rubidium condensates containing 20 million atoms are now consistently produced in the production chamber. This is significantly larger than other labs which produce rubidium condensates of around 1 million atoms. After first trapping and cooling atoms in the "production chamber", ultracold rubidium atoms have been transferred over 30 cm in 1.5 seconds to the auxiliary chamber. The atoms are moved between the chambers by first transferring the

atoms from the magnetic trap to an optical dipole trap created with a single focused laser beam (optical dipole trap, or ODT), and by then translating the focus of the beam from the production chamber to the science chamber. The performance of the transport was optimized to minimize heating and losses that occurred during acceleration so that the atoms could be evaporatively cooled to a BEC by simply lowering the depth of the optical trap after transport. Although the transport of cold atoms with an ODT had been previously demonstrated with sodium condensates [15, 47], the original design of our apparatus had to be improved to compensate for the higher mass and larger 3-body decay rate of rubidium. With the successful production of condensates in the auxiliary chamber, we can now begin loading the condensates onto atom optical devices, such as atom chips, waveguides and mirrors, or create optical lattices with significantly better optical access than that in the main production chamber. Although all the experiments described in this thesis have been performed in the main production chamber, the next generation of lattice experiments will be performed in the science chamber.

1.7 Outline of this thesis

In recent years optical lattices have proven to be a very versatile tool to study a wide variety of physics with Bose-Einstein Condensate, the work presented in this thesis highlights this versatility. All of the experiments presented here use optical standing waves, however the standing waves are used in very different ways and for very different purposes. The experiments performed here fall into two main categories, atom optics, both linear and nonlinear, and strongly correlated systems in optical lattices. The structure of this thesis is as follows: In chapter 2, I give a brief introduction to condensates in optical lattices, and in particular scattering from light gratings in the Kapitza-Dirac and Bragg regimes. Chapter 3 is the first chapter with experimental results. Here I discuss a measurement of the photon recoil momentum in dispersive media, which was performed by diffracting a condensate off of a one-dimensional light grating. In chapter 4 dispersion management is used to demonstrate the matter-wave

analogue of optical parametric generation and amplification of scattered atom pairs. In chapter 5 the superfluid-Mott Insulator transition in a deep three-dimensional optical lattice is discussed, and in chapter 6 two-photon microwave spectroscopy is used to study the superfluid-Mott insulator transition using atomic clock shifts. Chapter 7 briefly discusses the demonstration of Raman superradiance, where a polarization grating is created from a applied light pulse and an end fire mode, leading to self-stimulated Raman scattering. Finally, in chapter 8, I summarize the work presented in this thesis and give a brief outlook. The appendices give reprints of the relevant papers on which this thesis is based.

Chapter 2

Bose-Einstein Condensates in Optical Lattice Potentials

2.1 Atom-Light Interactions

If neutral atoms are placed in an electromagnetic field the atoms develop an induced electric dipole moment μ, where the interaction energy is given by

$$U = -\mu \cdot E, \tag{2.1}$$

where E is the applied electric field. This dipole moment has two main effects, for near-resonant light the effect is to change the atomic state through the absorption and emission of photons. Using this effect one can coherently manipulate both the internal and external states of the atom. For far off-resonant light, the primary effect is an energy shift to the atomic energy levels through the AC stark shift.

In this chapter (and in the rest of this thesis), we focus on optical potentials created with standing light waves. The first part of this chapter focuses on the diffraction of atoms from standing wave potentials where, using near-resonant light, the momentum state of the atom is coherently controlled. In the second we discuss the use of far off-resonant beams to create optical lattices potentials, where atoms are trapped in the nodes of the standing wave potential.

2.2 Atomic Diffraction from Optical Gratings

Atomic diffraction from optical gratings has proven to be an ideal tool for atom optics and atom interferometry. Kapitza-Dirac and Bragg Scattering from optical gratings were both first demonstrated as coherent beamsplitters for atomic beams of Sodium atoms [41, 77], and later demonstrated with Bose-Einstein condensates [70, 106, 86]. In the proceeding sections, diffraction from an optical grating is described using two different models, a more detailed discussion can be found in [46].

2.2.1 The Grating Picture

If a condensate is incident upon a periodic grating, after traversing the grating the condensate will be diffracted. The maxima of the resulting interference pattern can be found from the grating equation

$$\ell\lambda_{dB} = d\sin(\theta), \tag{2.2}$$

where ℓ is the diffraction order, λ_{dB} is the deBroglie wavelength as defined in Eq. (1.1), and d is the grating spacing. Although this equation is typically used to describe material gratings which modulate the amplitude of the wavefunction, it also holds true for phase gratings, where a periodic light grating is used to diffract the atoms. In light gratings, the atoms receive position dependent light shifts, and for wavelength λ the grating spacing is given by $d = \lambda/2$, the spacing of the nodes in the standing wave.

The electric field for a standing wave of light is given by

$$\vec{E}(z,t) = f(t)\left(E_0 sin(kz - \omega t)\hat{e} + E_0 sin(kz + \omega t)\hat{e}\right) \tag{2.3}$$

where $k = 2\pi/\lambda$ is the wavevector of the grating light, and $f(t)$ is the envelope function for the standing wave. The light shifts for this field are given by the AC Stark shift potential,

$$U(z,t) = \frac{\hbar\omega_R^2}{\delta} f(t)^2 \sin^2(kz) \tag{2.4}$$

where $\omega_R = \mu E_0/\hbar$ is the Rabi frequency, with $\mu = \langle e|e\vec{r}|g\rangle \cdot \hat{e}$ the dipole matrix element connecting the ground $|g\rangle$ and excited $|e\rangle$ states of the atom, and δ is the detuning of the beam. Eq. (2.4) is valid in the limit $\delta^2 >> \Gamma^2/4$, where Γ is the natural line width of the excited state.

2.2.2 The Raman Picture

Alternatively, diffraction from the light grating can be described as a stimulated Raman process, where the initial and final states, instead of being internal states, are different momentum states. The momentum of the atoms is changed through the stimulated absorbtion and subsequent emission of photons from the standing wave. The ground, intermediate, and final states for this Raman process are $|g,0\rangle$,$|e,1\rangle$, and $|g,2\rangle$, where $|g(e),\ell\rangle$ is the ground (excited) internal state with momentum $p = \ell\hbar k$. The Hamiltonian for this Raman process is given by

$$H(t) = H_0(t) + H_{int}(t), \tag{2.5}$$

where in the electric dipole approximation

$$H_{int}(t) = -\mu \cdot E = -\imath e^{-i\omega t}\frac{\hbar\omega_R}{2}\left(|e,1\rangle\langle g,0| - |e,1\rangle\langle g,2|\right) + h.c., \tag{2.6}$$

and

$$H_0(t) = \hbar\omega_0|e,1\rangle\langle e,1| + \hbar\omega_{rec}\left(|g,0\rangle\langle g,0| + |g,2\rangle\langle g,2|\right) \tag{2.7}$$

where ω_0 is the transition frequency between the ground and excited state, and $E_{rec} = \hbar\omega_{rec} = \frac{(\hbar k)^2}{2m}$ is the recoil frequency. To avoid scattering atoms into the wrong final state, the fourier width of the applied light pulse with length τ must be smaller than the separation between momentum states

$$\tau >> \frac{\pi}{4\omega_{rec}}. \tag{2.8}$$

When this condition is fulfilled, the scattering is in the Bragg regime. If this condition is not fulfilled than the scattering is described as Kaptiza-Dirac (or Raman-Nath) scattering.

2.2.3 Bragg Scattering

In the Bragg regime, the fraction of atoms scattered into the final state $|g, 2\rangle$ can be found by using the trial wavelength

$$|\psi(t)\rangle = c_0(t)e^{-\imath\omega_{rec}t}|g, 0\rangle + c_1(t)e^{-\imath\omega_0 t}|e, 1\rangle + c_2(t)e^{-\imath\omega_{rec}t}|g, 2\rangle. \tag{2.9}$$

Subbing this into Schrödinger equation, and solving for $c_2(t)$ one finds the transition probability

$$P_2(\tau) = |c_2(t)|^2 = \sin^2\left(\frac{\omega_R^{(2)}}{2}\tau\right), \tag{2.10}$$

where $\omega_R^{(2)} = \omega_R^2/2\delta$ is the two-photon Rabi frequency. This can be extended to an N^{th} order Bragg process where atoms absorb N photons from one direction, and emit N photons into the opposite direction, with Rabi frequency $\omega_r^{(2N)} = \frac{\omega_R^{2N}}{2^{2N-1}\delta_1\delta_2\ldots\delta_{2N-1}}$.

For Bragg scattering to occur energy and momentum must be conserved in the scattering process. Instead of varying the angle and velocity of the condensate relative to the standing wave it is typically easier to vary the standing wave by adding a small detuning, δ_L between the two laser beams used to make the standing wave. The resonance condition is then given by

$$\hbar\delta_L = 2N\frac{\hbar^2k^2}{m}\sin^2(\theta/2), \tag{2.11}$$

where as shown in Fig. 2-1, θ is the angle between the two beams.

Effect of the Mean Field Interaction

As discussed in section 1.5, for particle like excitations in the condensate $\hbar\omega = \hbar\omega_{rec} + nU_0$, and there is a mean field shift to the resonance frequency. Atoms in the initial

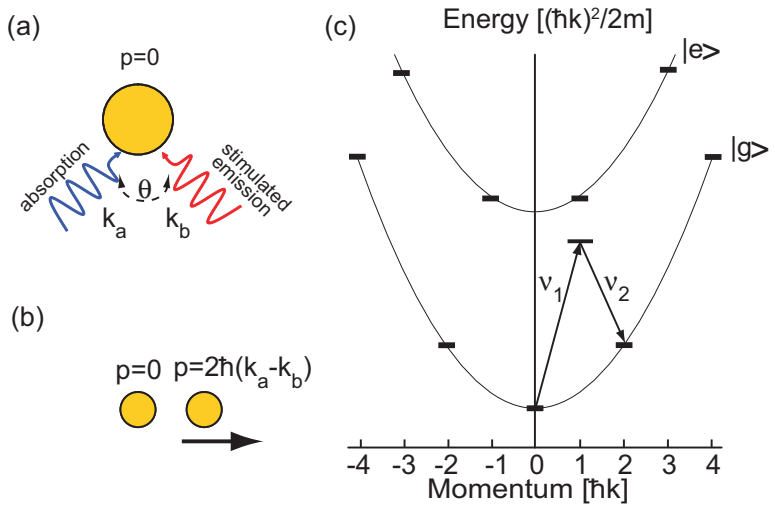

Figure 2-1: Bragg scattering (a) In Bragg scattering the atom absorbs a photon from one beam, and emits the photon into the second. The detuning of the beams are set such that the atom only absorb photons from one of the beams, therefore atoms are only scattered in one direction. (b) Since two photons are scattered, the momentum of the atom changes by $2\hbar k$ (c) Bragg transition diagram. Atoms are only diffracted when the frequency and angle between the beams is tuned such that both energy and momentum are conserved.

condensate are indistinguishable, however once atoms have been scattered into the final momentum state they are distinguishable and have twice the mean field energy due to the exchange term in the interaction potential [106], therefore the resonance frequency is shifted by nU_0, the mean field energy.

2.2.4 Kapitza-Dirac Scattering

In the Kapitza-Dirac, or Raman-Nath regime $\tau << 1/\omega_{rec}$. In this limit, the fourier width of the pulse is larger than the separation between adjacent momentum states, and atoms can be scattered into higher order momentum states. For short interaction times, the motion of the atoms during the pulse can be neglected, therefore the kinetic energy term in Eq. 2.7 can be ignored. The population in a given momentum state $2N\hbar k$ can be found by looking at the phase shift applied to the atoms by the AC Stark shift (Eq. (2.4)) during the interaction time,

$$|\psi\rangle = |\psi_0\rangle e^{\frac{-i}{\hbar}\int dt U(z,t)} = |\psi_0\rangle e^{\frac{-i}{2\delta}\omega_R^2\tau} e^{\frac{i}{2\delta}\omega_R^2\tau\cos(2kz)}. \tag{2.12}$$

Using an identity for Bessel functions, one finds

$$P_N = J_N^2(\omega_R^{(2)}\tau) \tag{2.13}$$

where J_N is the N^{th} order Bessel Function of the first kind. As shown it Fig. 2-2, as the power is increased the fraction of atoms in higher orders increases.

2.3 Bose-Einstein Condensates in Optical Lattices

In the discussion of diffraction from optical gratings, a few assumptions were made: 1) The standing wave was pulsed on for a short period of time. 2) A plane wave was used. These assumptions allowed us to ignore the external trapping potential created by the standing wave, and also allowed us to use the excitation spectrum derived in section 1.5. However if the optical lattice is not pulsed on, but is instead ramped on these assumptions are no longer valid. In recent years Bose-Einstein condensates held in optical lattices has become an active research field, and a review of recent work done with Bose-Einstein condensates in optical lattices can be found in [84]. In the following section the energy spectrum and ground state wavefunction for Bose-Einstein condensates held in optical lattices is discussed. In this chapter only weak lattices are discussed where the system can still be described as a superfluid with a macroscopic wavefunction. In chapter 5 the behavior in deep optical lattices where this is no longer true is discussed.

2.3.1 Optical Dipole Traps

In Bragg and Kapitza-Dirac scattering, near-resonant laser light is used to manipulate the final momentum state of the atoms. For optical lattices if near-resonant light is used the high spontaneous scattering rate leads to short condensate lifetimes. If a condensate is illuminated with a laser beam, the resulting potential due to the AC

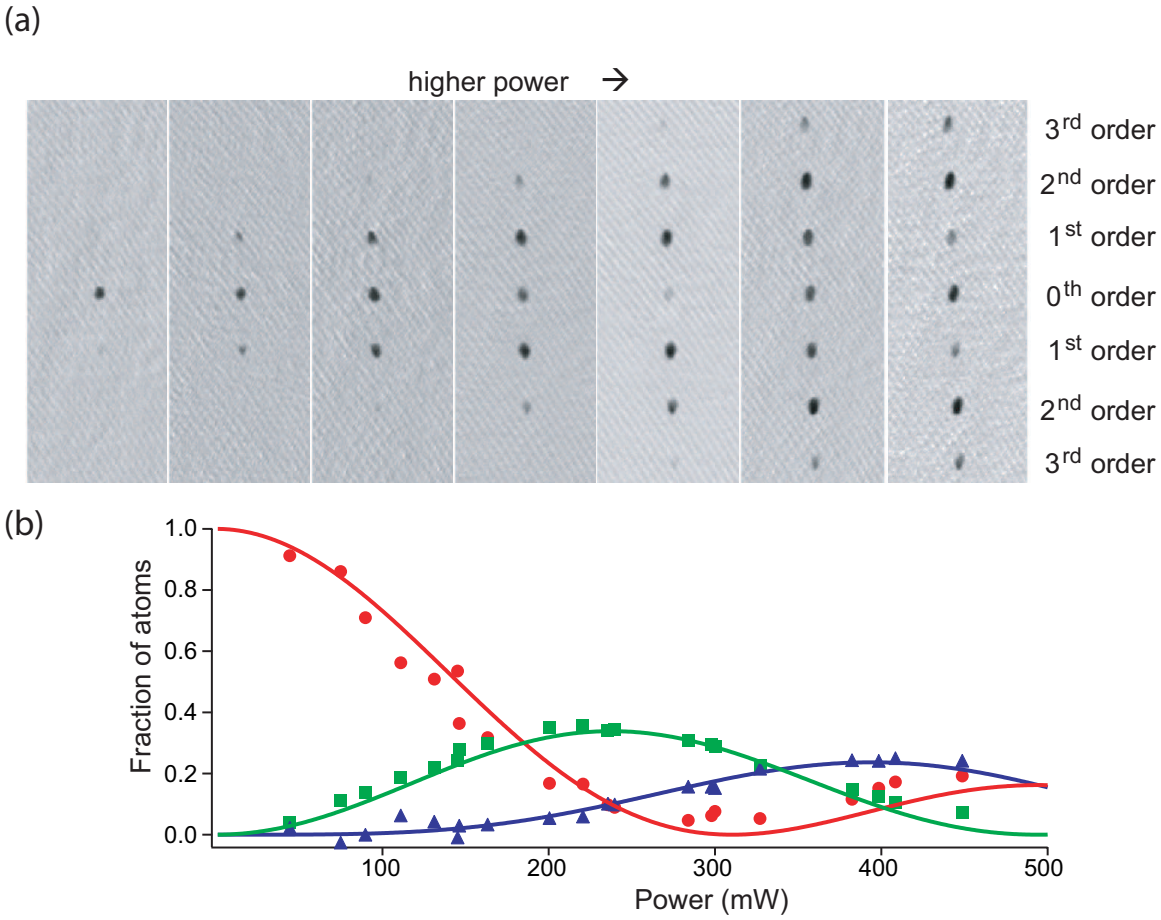

Figure 2-2: Kapitza-Dirac scattering. (a) In Kapitza-Dirac scattering, due to the short length of the pulse the atom can absorb photons from either of the beams, and atoms are symmetrically scattered in both directions. As the power in the pulse is increased atoms are scattered into higher momentum states $2N\hbar k$ where N is an integer. (b) The fraction of atoms in a given momentum state can be fit by Bessel functions as $P_N = J_N^2(\omega_R^{(2)}\tau)$, where $\omega_R^{(2)}$ is the 2-photon Rabi frequency, and τ is the length of the pulse. The fraction of atoms is shown for the 0^{th} (circles), 1^{st} (squares), and 2^{nd} (triangles) order momentum states.

Stark shift can be written as

$$V(r) = \frac{\hbar\omega_R^2}{\delta} = \frac{3\pi c^2}{2\omega_0^3}\left(\frac{\Gamma}{\omega_0 - \omega} + \frac{\Gamma}{\omega_0 + \omega}\right) I(r) \approx \frac{3\pi c^2}{2\omega_0^3}\frac{\Gamma}{\delta} I(r), \tag{2.14}$$

where the natural line width Γ is given by

$$\Gamma = \frac{\omega_0^3}{3\pi\epsilon_0\hbar c^3}\mu^2, \tag{2.15}$$

and I is the intensity of the laser beam. Depending on the sign of the detuning the atoms are either attracted or repelled from the region of maximum intensity. The spontaneous scattering rate from the laser is

$$\Gamma_{SC}(r) = \frac{3\pi c^2}{2\hbar\omega_0^3}\left(\frac{\Gamma}{\delta}\right)^2 I(r) = \frac{\Gamma}{\hbar\delta} V(r) \tag{2.16}$$

for a given potential depth, the spontaneous scattering rate can be decreased by using far off-resonant light. Although the above potential is only for two level atoms, for multilevel atoms the potential can be generalized to

$$V(r) = \frac{3\pi c^2\Gamma}{2\omega_0^3} I(r) \sum_j \frac{c_j}{\delta_j} \tag{2.17}$$

where δ_j is the detuning between the ground $|g\rangle$ and the excited state $|e_j\rangle$, and $c_j = \|\mu\|/mu_j$ is the relative coupling strength.

The simplest way to trap atoms using the AC Stark shift potential is by using a focused red-detuned laser beam [5, 17]. The intensity profile of a focused gaussian laser beam with power P, focused along the z-axis is

$$I(r, z) = \frac{2P}{\pi w^2(z)} e^{-2\frac{r^2}{w^2(z)}} \tag{2.18}$$

where the beam waist along the z-axis is given by $w(z) = w_0\sqrt{1 + (z/z_R)^2}$. The minimum beam waist at the focus is w_0, and $z_R = \pi w_0^2/\lambda_L$ is the Rayleigh length of the focus. If the spatial extent of the condensate is less than the beam waist

($R_{TF} << w_0, z_R$), then the resulting trapping potential can be approximated as

$$V_{ext}(r,z) \approx V\left[1 - 2\left(\frac{r}{w_0}\right)^2 - \left(\frac{z}{z_R}\right)^2\right], \tag{2.19}$$

this potential has cylindrical symmetry with trap frequencies $\omega_r = \sqrt{4V/mw_0^2}$ and $\omega_z = \sqrt{2V/mz_R^2}$ in the radial and axial directions.

If a second, counter-propagating beam is added where the frequency, polarization, and power of the beam are identical to the initial dipole trap, than a standing wave potential is created with

$$V_{lat}(r,z) = 4V\cos^2(kz)\left[1 - 2\left(\frac{r}{w_0}\right)^2 - \left(\frac{z}{z_R}\right)^2\right]. \tag{2.20}$$

As shown in Fig 2-3 the easiest (and most stable) way to create this lattice potential is by retroreflecting the initial dipole beam. Typically the lattice trap depth V_{lat} is given in terms of the recoil frequency E_{rec}. The lattice trap frequency along the axial direction is given by

$$\omega_{lat} = \frac{\hbar k^2}{m}\sqrt{\frac{V_{lat}}{E_{rec}}}. \tag{2.21}$$

2.3.2 Band Structure

Ignoring the external trapping potential, the potential due to the lattice can be written as

$$V_{latt}(z) = sE_{rec}\sin^2(kz) = \frac{sE_{rec}}{2}(1 - \cos(2kz)), \tag{2.22}$$

where sE_{rec} gives the lattice depth in terms of the recoil energy. This potential is invariant under translation, i.e $V_{latt}(z + \pi/k) = V_{latt}(z)$. Therefore from Bloch's theorem (see for example [76]) the eigenstates of this potential are

$$\psi_{nq}(z) = e^{\imath qr}u_{nq}(z) \tag{2.23}$$

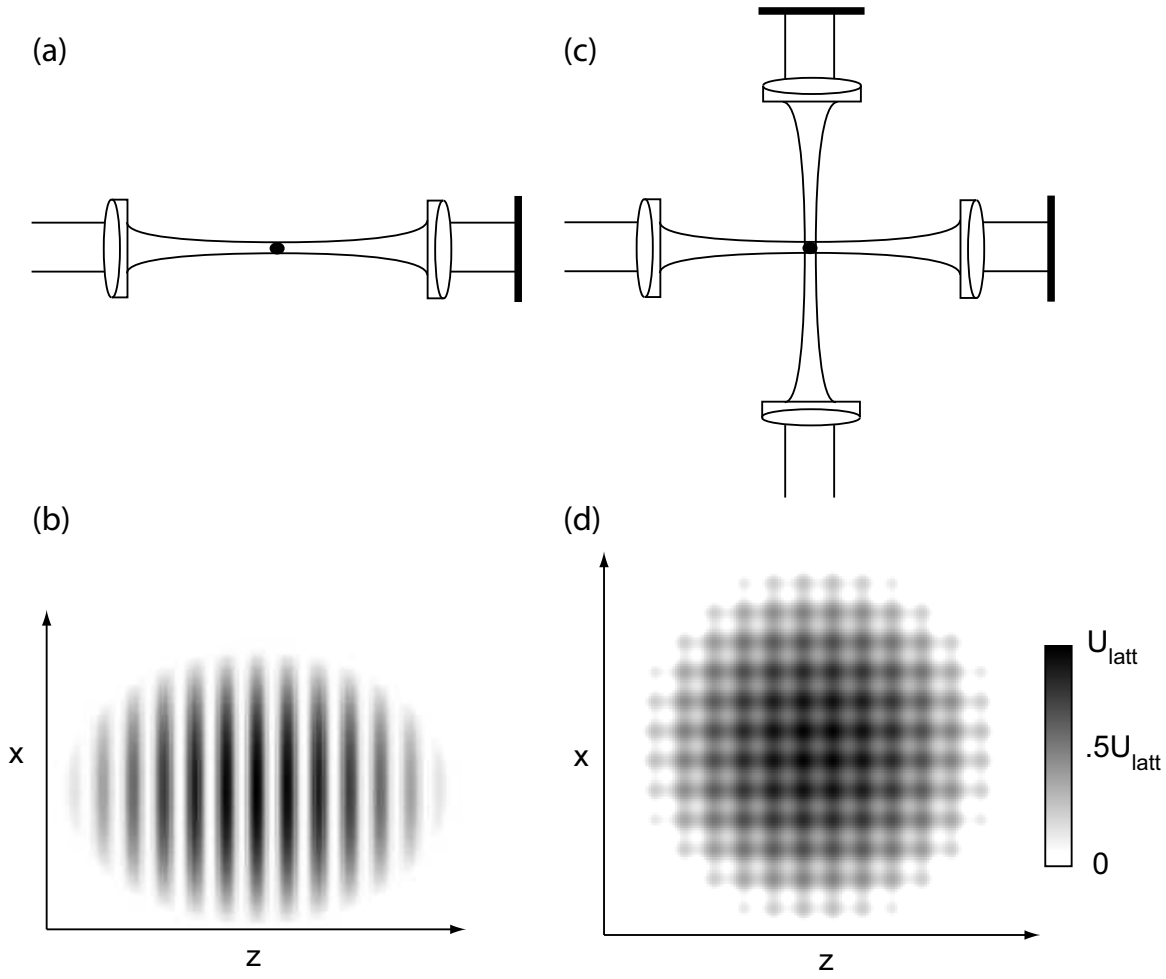

Figure 2-3: Optical lattice potential. (a) Retroreflected one-dimensional lattice using a focused gaussian laser beam. (b) The resulting 1D lattice potential. (c) Experimental setup for retroreflected 2D lattice. (d) Resulting 2D potential, where the two lattice beams have either perpendicular polarization or different frequencies.

where $u(z + \pi/k) = u(z)$. The eigenstates are plane waves whose amplitude are modulated with the same periodicity as the lattice potential. The energy spectrum has a band structure, where q is the quasimomenta, and n is the band index. The band energy is found from the Schrödinger equation,

$$\hat{H}|\psi_{nq}\rangle = E_{nq}|\psi_{nq}\rangle. \tag{2.24}$$

Since both the lattice potential, and u_{nq} are periodic functions, we can write then both as Fourier series

$$\Psi_{nq}(z) = e^{\imath qr} \sum_j c_j^n e^{2\imath jkr} \tag{2.25}$$

$$U(r) = \sum_m U_m e^{1\imath kr}. \tag{2.26}$$

Subbing these into the Schrödinger equation, and truncating the sum at $|j| = j_{max}$, one finds $2(2j_{max}) + 1$ linear equations. For our sinusoidal wavefunction this is simplified as only the $U_{\pm 2k} = U_{latt}/4$ and $U_0 = U_{latt}/2$ terms are non zero in Eq. (2.26). For a given quasimomenta, this leads to $2j_{max}+1$ different eigenenergies, which are the band energies E_n, with $n = 0, 1, ..., 2j_{max}$. If only the first few energy bands are of interest, these equations can be easily solved by truncating j.

Fig 2-4 shows the resulting band structure for a one-dimensional lattice for different lattice depths as a function of the quasimomenta q in the first Brillouin zone. For $0E_{rec}$ (i.e no lattice), the band structure is just the quadratic dispersion relation for free particles. As the lattice depth is increased, a band gap appears between the energy bands and the dispersion relation flattens out.

2.3.3 Wannier Functions

The Bloch functions given above are plane waves, they are completely delocalized over the entire lattice sites. As we will see in chapter 5, it is sometimes more convenient to instead use Wannier functions to describe the behavior of atoms in the lattice. The Wannier functions are an orthogonal set of wavefunctions which in contrast to

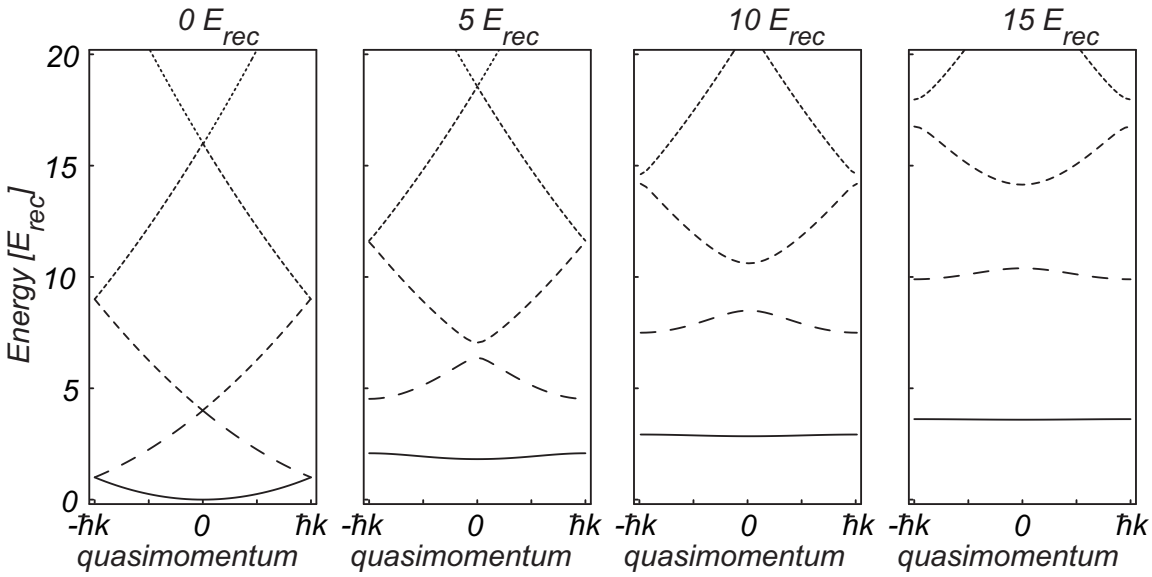

Figure 2-4: Band structure in the optical lattice. Energy of the Bloch state versus the quasimomentum is shown in the first Brillouin zone is shown for the lowest bands. Lattice depths of 0 E_{rec}, 5 E_{rec}, 10 E_{rec}, and 15 E_{rec} are shown. As the lattice depth is increased the band structure flattens out, and the energy gap between the bands increases.

the Bloch functions are localized wavefunctions at individual lattice sites [76]. The Wannier function for an atom in the j^{th} lattice site in the n^{th} energy band can be constructed from the Bloch functions as

$$w_{jn}(z) = \frac{1}{\sqrt{N}} \sum_{q} e^{-\imath q j} \psi_{nq}(z). \tag{2.27}$$

Using the Wannier functions, one can calculate the probability for an atom to tunnel from the j^{th} to the k^{th} site by calculating the overlap integral between the Wannier functions in the two adjacent sites, the tunneling matrix element J is given by

$$J = \int w_{jn}(z) \left(-\frac{\hbar^2}{2m} \frac{\partial^2}{\partial z^2} + V_{latt} \right) w_{kn}(z) dx. \tag{2.28}$$

2.3.4 Adiabaticity

If a condensate is loaded into the optical lattice adiabatically, it will also be loaded into the ground state of the optical lattice. For low lattice depths, where the tunneling

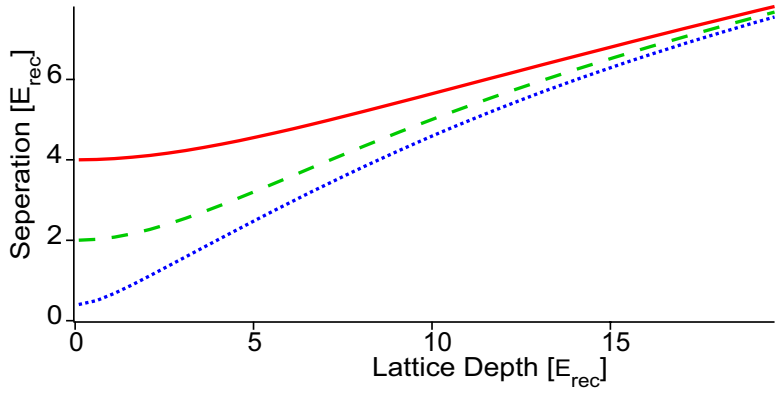

Figure 2-5: Separation between the first two energy bands for $q = 0$ (solid line), $q = 0.5k$ (dashed line), $q = 0.9k$ (dotted line). The adiabatic condition is easily fulfilled for $q = 0$, but becomes more difficult for higher quasimomenta.

rate is high, the condensate can still be described with a macroscopic wavefunction. In a stationary state the chemical potential is constant throughout the lattice, and the condensate has quasimomentum $q = 0$. The adiabaticity condition for loading a condensate with quasimomentum q into the lowest Bloch band, $|0, q\rangle$ of the lattice is given by [96]

$$\left|\langle 1, q|\frac{\partial H}{\partial t}|0, q\rangle\right| << \Delta E^2(q, t)/\hbar, \tag{2.29}$$

where $|1, q\rangle$ is the 1^{st} excited band, and ΔE is the energy gap between the two bands. Fig 2-5 shows the energy separation for three different quasimomenta. For $q = 0$, the adiabaticity condition can be met for $dV_{latt}/dt << (4E_{rec})^2/\hbar$, since the separation between the bands is a minimum at $V_{latt} = 0$ where $\Delta E = 4E_{rec}$. This is the separation from the free particle dispersion curve. However, as the quasimomentum increases, the separation at $V_{latt} = 0$ approaches zero, and the adiabaticity condition becomes more difficult to fulfill.

In addition to being adiabatic with respect to the lattice frequency, as the lattice depth is increased the external trap frequencies also increase due to the gaussian beam profile. The lattice ramp must be adiabatic with respect to the external trap frequencies, and the mean field energy of the condensate.

2.3.5 Atomic Diffraction from Optical Gratings Revisited

In the beginning of this chapter, diffraction from optical gratings was discussed by modeling it both as a classical grating, and also by modeling it as stimulated raman process. After discussing the band structure for condensates loaded into optical lattices it seems useful to revisit Bragg and Kapitza-Dirac scattering in the context of nonadiabatic loading of the lattice. If the lattice potential is abruptly turned on, instead of ramped on adiabatically, the resulting wavefunction is analogous to Bragg and Kaptiza-Dirac scattering [25].

If a condensate, initially assumed to be a plane wave $\phi_q(t)$ with momentum q at $t = 0$ is suddenly loaded into an optical lattice, the wavefunction can be written as a superposition of Bloch states $|n, q\rangle$. Where

$$|\psi(t=0)\rangle = \sum_{n=0}^{\infty} |n,q\rangle\langle n,q|\phi_q\rangle, \tag{2.30}$$

and $\langle n, q|\phi_q\rangle = c_{n,q}(0)$. While the lattice is turned on each Bloch function evolves at its respective eigenenergy, and the condensate wavefunction evolves as

$$|\psi(t)\rangle = \sum_{n=0}^{\infty} c_{n,q}(0) e^{-\imath E_n(q)t/\hbar} |n,q\rangle. \tag{2.31}$$

If the lattice is then suddenly turned off after time τ, the final wavefunction for the condensate is given by mapping the lattice state back onto the plane wave basis. The resulting wavefunction is given by

$$|\psi(\tau)\rangle = \sum_{j=0}^{\infty} d_q(j) |\phi_{q+2j\hbar k}\rangle, \tag{2.32}$$

where

$$d_q(j) = \sum_{n=0}^{\infty} c_{n,q}(0) c_{n,q}(j) e^{-\imath \frac{E_n(q)}{\hbar}\tau}. \tag{2.33}$$

The exponential term produces oscillations in the population of the plane wave momentum states as a function of τ, the time the condensate is held in the optical

lattice. If the condensate is initially created with $q = 0$, then the initial wavefunction is symmetric, and only even energy bands are populated. The population in the $|2j\hbar k\rangle$ states oscillates with time, and this describes Kapitza-Dirac scattering. The observed oscillation period is given by the energy gap between the ground and excited bands at $q = 0$, which for deep lattices ($U_{latt} > 5E_{rec}$) is given by the lattice trap frequency $\hbar\omega_{latt}$. If instead of being initially at rest, the condensate is created with initial momentum, for example in the momentum state $q = \hbar k$, then the odd bands are also populated, and for a shallow lattice this is equivalent to first order Bragg Scattering.

2.3.6 Momentum vs. Quasimomentum

As a final note, a common confusion when loading condensates into optical lattices is the difference between momentum and quasimomentum. Due to the translational symmetry of the lattice, the only physically distinct quasimomenta are in the first Brillouin zone between $q = -k$ to $q = k$. But when the lattice is ramped on or off how does momentum map to quasimomentum and vice-versa? To understand this it is easiest to look at the "band structure" for the free particle shown in Fig 2-4(a). If an atom initially has momentum $q_0 > k$, then the energy for the particle is given by $E_0 = \hbar^2 q_0^2/2m$, and the atom will be in an excited band, as the lattice is ramped on, the atom has quasimomentum $q_0 Mod(2k)$, but will be in an excited energy band. Similarly, if an atom is in the excited energy band n in the lattice, with quasimomentum q_L, if the lattice is adiabatically ramped down the atom will be mapped onto the free particle momentum state $|q_F| = |q_L + nk|$ with energy $E_F = \hbar^2 q_F^2/2m$.

Chapter 3

Photon Recoil Momentum in Dispersive Media

This chapter describes a measurement of the photon recoil momentum in dispersive media, and supplements work previously reported in Ref [63], which is also included in Appendix A

3.1 Momentum in Dielectric Media

The transmission of momenta in dielectric media has raised controversy for over 100 years, starting with the papers of Minkowski [79, 80], and Abraham [2, 3] in 1908 and 1909. The main question is as follows, is the momentum density carried by an electromagnetic wave in dispersive medium given by $(\vec{D} \times \vec{B})/4\pi c$ as suggested by Minkowski, or by $(\vec{E} \times \vec{H})/4\pi c$ as was argued the following year by Abraham. Stated more simply, is the momentum in a dispersive medium given by $p_{min} = n_r h/\lambda$, or $p_{ab} = h/n_r\lambda$, where n_r is the index of refraction of the medium, and λ is the wavelength of the electromagnetic wave in vacuum. If one does a literature search over the last 100 years, numerous papers are found on the subject with each form of the momentum receiving roughly equal support (for a review see [21, 91]) until the 1970's when Peierls [90] building on the earlier work of Gordon[40], argued that both

were incorrect, and the momentum was instead given by

$$p = \frac{h}{n_r \lambda}\left[\frac{1}{2}(1+n_r^2) - \frac{1}{10}(n_r^2-1)^2\right]. \tag{3.1}$$

When an electromagnetic field enters a dispersive media, the frequency of the light ν remains the same, but the wavelength of the light is modified by the index of refraction. The wavelength in the media is given by $\lambda' = \lambda/n_r$, and the electromagnetic momentum carried by the photon is also modified. For momentum to be conserved in the system, this means that the electromagnetic wave must carry mechanical momentum with it as it travels through the medium. The medium is accelerated as the pulse enters the medium, and decelerates as the pulse exits. The total momentum for the system is given by $p = p_{em} + p_{mech}$, however confusion arises when one tries to properly divide the total momentum into the electromagnetic momentum p_{em}, and the mechanical momentum p_{mech}, carried with the wave. As a simple example of the confusion surrounding this question, if one assumes that the electromagnetic momentum is given by the deBroglie wavelength $p = h/\lambda$, then in the medium $p_{em} = n_r h/\lambda = n_r \hbar k$. However, if one assumes that the fundamental relation is given by $E = mc^2$, and $p = E/c$ then one instead finds $p_{em} = h/n_r\lambda$.

3.1.1 Previous Experiments

Early experiments did little to solve the controversy, the first attempts to measure the momentum in dispersive media were made by Jones and Richards [61], and later updated by Jones and Leslie [60]. In their experiments, a beam of light was bounced off of a mirror suspended in a dielectric. The results showed that the momentum transferred to the mirror was given by $2n_r\hbar k$. Although at first glance these results seem to agree with the Minkowski momentum, it was later shown that these results were consistent with both the Abraham and Minkowski pictures. These results can be simply understood by considering the standing wave created by the incident and reflected beam. The standing wave imparts momentum to the medium which remains even after the pulse has left.

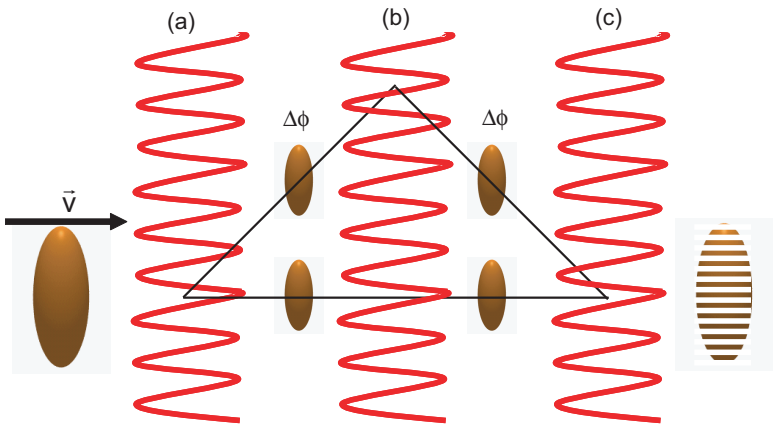

Figure 3-1: Light grating interferometer. (a) The atoms are split into two momentum components using a light pulse. A phase shift can be applied along one of the two arms. (b) A second pulse is applied redirecting one of the momentum components, while leaving the other unchanged. (c) A third light pulse is applied to recombine the components, and the interference pattern is read out.

3.2 Precision Measurements and Atom Interferometry

Recently, there have been discussions about the momentum transferred to a single atom when it absorbs a photon, when that atoms is part of a dilute atomic cloud with index of refraction n_r. Besides answering a fundamental question about the transmission of momenta in dielectric media, this is also an important question for atom interferometry. As was discussed in chapter 2, standing waves can be used in atom interferometry to manipulate the state of atoms, and as shown in Fig.3-1, a phase shift can be applied to one of the arms. As discussed in chapter 2, the outcoupled atoms have momentum $p = 2N\hbar k$, therefore a phase shift will occur just due to the recoil momentum of the outcoupled atoms. In order to understand any phase shift due to external sources, one must therefore first have a clear understanding of the recoil momentum transferred to the atoms.

This is of particular importance for precision measurements of h/m with ultracold atoms. Where precise measurements of the recoil frequency are used to determine a value for h/m, which in turn can be used to derive a value of α, the fine structure constant [112, 119, 120, 45, 6, 71]. This result combined with the value of alpha derived

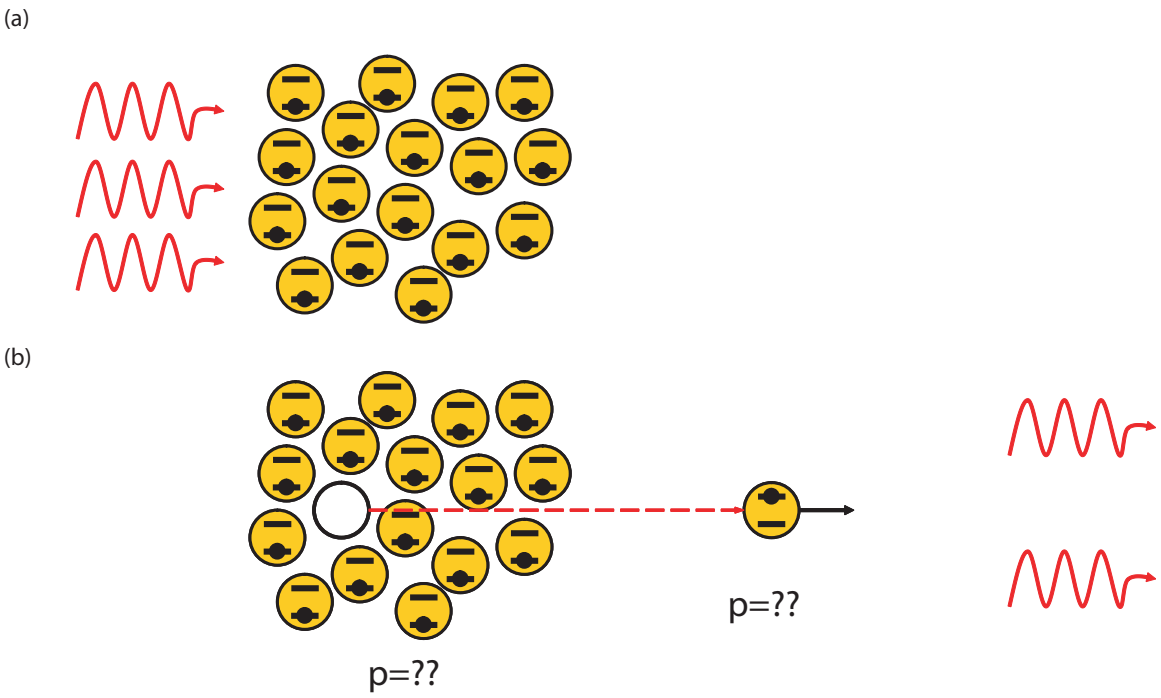

Figure 3-2: The index of refraction in dispersive media. (a) A laser beam is incident on a dilute atomic cloud with index of refraction n_r, initially at rest. (b) An atom within the cloud absorbs a photon. When the atom absorbs the photon what momentum is transferred to the atom, and what momentum (if any) is left in the cloud?

from the (g-2) measurements for the electron and positron [62, 66, 51] provide a test of QED. Currently the largest uncertainty in measurements of the recoil momentum, and the resulting value for α, was due to the uncertainty of dispersive effects on the value for the recoil frequency [120].

What is the recoil frequency when an atom in an atomic cloud absorbs a photon? In illustration of this question is shown in Fig. 3-2. If one assumes that no momentum is left in the medium after the photon is absorbed, then the momentum transferred to the atom should be $p = \hbar k$. One also reaches the same conclusion if one considers a dilute gas, where the absorbing atom is isolated from the surrounding medium by vacuum. However, if one calculates the momentum transferred to the atoms classically using the Lorentz force applied to the atom during the absorption, you find that momentum transferred to the atom is $p = n_r \hbar k$, which would also imply that momentum must be left in the medium after the pulse has passed [49].

3.3 Index of Refraction of a Dilute Atomic Cloud

When a dilute cloud of atoms is illuminated by a laser beam, the index of refraction n_r, can be found from the macroscopic polarization of the gas, $P = \rho\langle d\rangle = \chi\epsilon_0 E$, where ρ is the density of the atomic cloud, $\langle d\rangle$ is the average dipole moment of the atoms, χ is the atomic susceptibility and ϵ_o is the permittivity of free space. The dipole moment for an atom within the cloud is given by $\langle d\rangle = \epsilon_0\alpha(E_L + E_{int})$, where α is the atomic polarizability, E_L is the applied laser field, and E_{int}, the internal electric effect due to the surrounding cloud is given by $E_{int} = \frac{1}{3\epsilon_0}P$. Combining these equations we find[1]

$$\chi = \frac{\rho\alpha}{1 - \rho\alpha/3}. \tag{3.2}$$

For a two level atom, the atomic polarizability

$$\alpha = -\frac{\mu^2}{\hbar\epsilon_0}\frac{1}{\Gamma - i\Delta} = \frac{3\pi\lambda\!\!\!^{-3}\Gamma}{\Gamma - i\Delta}, \tag{3.3}$$

where Γ is the natural line width, and Δ is the detuning of the laser beam. For a dilute cloud, in the limit of $\rho\lambda\!\!\!^{-3} \ll 1$ the polarizability can be approximated as $\chi = \rho\alpha$. For ^{87}Rb, the situation is complicated by the hyperfine structure. In Fig. 3-3 the D_2 transition hyperfine structure is shown.

For a condensate initially in the $|F = 1, m_F = -1\rangle$ state, there are a number of possible excited states however, the situation can be simplified by using π-polarized light. For π-polarized light there are only two allowed transitions, the $5^2S_{1/2}, F = 1 \rightarrow 5^2P_{3/2}, F = 1$ and the $5^2S_{1/2}, F = 1 \rightarrow 5^2P_{3/2}, F = 2$ transition. The index of refraction for the condensate, $n_r = \sqrt{1 + \chi}$ is then given by

$$n_r = \sqrt{1 - 12\pi\rho\left(\frac{\lambda}{2\pi}\right)^3\left(\frac{5}{12}\frac{\Delta_1}{\Gamma}\frac{1}{1 + (2\frac{\Delta_1}{\Gamma})^2} + \frac{1}{4}\frac{\Delta_2}{\Gamma}\frac{1}{1 + (2\frac{\Delta_2}{\Gamma})^2}\right)}, \tag{3.4}$$

where Δ_1 and Δ_2 are the detunings relative to the F=1 $\rightarrow$ F′=1 and F′=2 transitions, respectively.

[1]For dense clouds there is also a correction due to resonant Dipole-Dipole interactions [82].

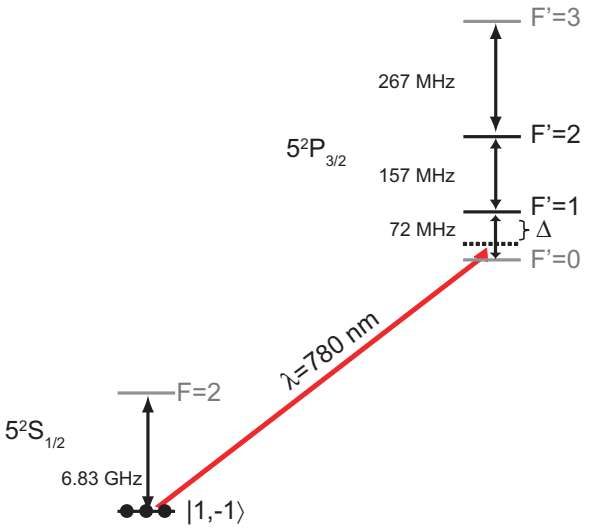

Figure 3-3: Hyperfine structure for the ^{87}Rb D_2 transition. The frequency splitting between the hyperfine energy levels is given. Starting with a condensate in the $|F = 1, m_F = -1\rangle$ state, and using π-polarized light there are only two allowed transitions.

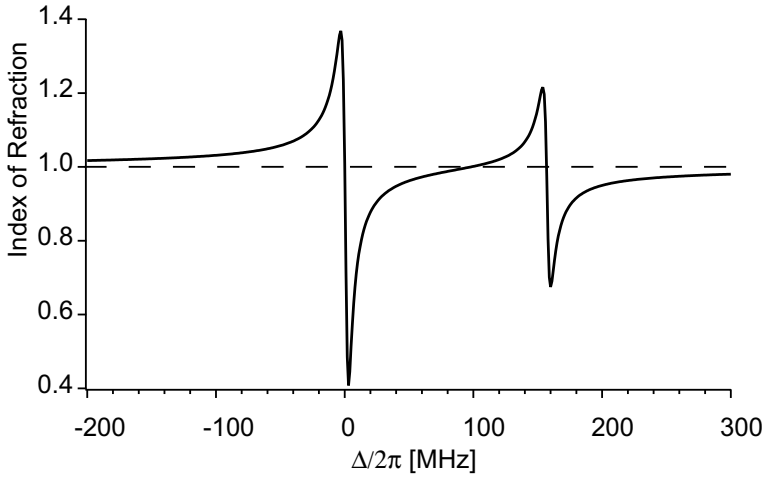

Figure 3-4: The index of refraction for a $|1, -1\rangle$ ^{87}Rb condensate illuminated with π-polarized light, as a function of the laser detuning Δ. The detuning is given relative to the $5^2S_{1/2}, F = 1 \rightarrow 5^2P_{3/2}, F = 1$ transition.

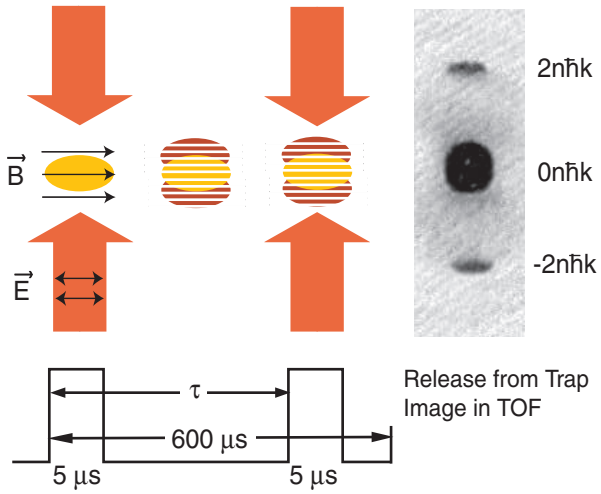

Figure 3-5: . Experimental setup of the two pulse light grating interferometer. The effect of the first pulse was to outcouple a small fraction of atoms into the $|\pm 2\hbar k_{rec}\rangle$ momentum state, where $k_{rec} = n_r k$ is the single photon momentum in the medium. During the delay between pulses the phase of atoms in the$|\pm 2\hbar k_{rec}\rangle$ momentum states evolve at a faster rate than those still at rest due to the recoil energy. After a variable delay time τ, a second pulse was applied recombining a portion of atoms in the $|\pm 2\hbar k_{rec}\rangle$ state with those at rest in the initial condensate. The condensate was then released from the trap and imaged in time of flight. A typical absorption image taken after 43ms time of flight is shown.

3.4 Experimental Setup

To measure the index of refraction of the condensate, a two pulse light grating interferometer was used, as shown in Fig. 3-5. The grating was creating using retroreflected, near-resonant light detuned from the $5^2S_{1/2}, F = 1 \rightarrow 5^2P_{3/2}, F = 1$ transition at 780nm. The light was π-polarized both to minimize the number of allowed transitions, and also to minimize superradiant scattering [53, 100]. The laser had a linewidth γ much smaller than Γ, the natural linewidth for the transition. The laser was aligned perpendicular to the long axis of the condensate.

The two applied pulses were 5 μs in length, this is sufficiently short that we can assume the atoms do not move during the pulse, and therefore describe them using Kapitza-Dirac scattering (as described in Chap.2.2.4).The first pulse outcouples a fraction of atoms into the momentum states $|\pm 2\ell\hbar k_{rec}\rangle$, where the population in

the ℓ^{th} momentum state is given by $P_\ell = J_\ell^2(\theta)$, $\theta = \frac{\omega_R^2 t_p}{2\Delta}$, $k_{rec} = n_r k$ is the single photon momentum in the medium, and t_p is the length of the pulse. For $\frac{\omega_R^2 t_p}{2\Delta} < 1$ a negligible fraction of atoms is diffracted into states with $\ell > 1$, and we can restrict our discussion to the $|\pm 2\hbar k_{rec}\rangle$ momentum states. Given that the initial condensate is at rest, $|\psi_o\rangle = |0\hbar k_{rec}\rangle$. Immediately after the pulse, the wavefunction is given by

$$|\psi(t_p)\rangle = J_1(\theta)|\pm 2\hbar k_{rec}\rangle + J_0(\theta)|0\hbar k_{rec}\rangle. \tag{3.5}$$

During the delay time τ, the phase of the $|\pm 2\hbar k_{rec}\rangle$ states evolves at a faster rate than the $|0\hbar k_{rec}\rangle$ state due to the recoil energy, $E_{rec} = 4\hbar\omega_{rec}$. After the delay τ, the wavefunction will have evolved as

$$|\psi(\tau)\rangle = |\psi_o\rangle \left(J_1(\theta)|\pm 2\hbar k_{rec}\rangle e^{\mp i4\omega_{rec}\tau} + J_0(\theta)|0\hbar k_{rec}\rangle\right). \tag{3.6}$$

At $t = \tau$ we apply a second pulse that partially recombines the momentum states. Immediately after this second pulse the wavefunction is given by

$$\begin{aligned}|\psi(\tau + t_p)\rangle = {} & J_1(\theta)J_0(\theta)\left(e^{\mp i4\omega_{rec}\tau} + 1\right)|\pm 2\hbar k_{rec}\rangle \\ & + \left(J_1^2(\theta)\left(e^{-i4\omega_{rec}\tau} + e^{i4\omega_{rec}\tau}\right) + J_0^2(\theta)\right)|0\hbar k_{rec}\rangle.\end{aligned} \tag{3.7}$$

After applying the two pulses, the probability of finding the atoms in the $|0\hbar k_{rec}\rangle$ momentum state, $\rho_0 = \langle\psi(\tau + t_p)|0\hbar k_{rec}\rangle|^2$ is given by

$$\rho_0 = J_0^4(\theta) + 4\left(J_0^2(\theta)J_1^2(\theta) + J_1^4(\theta)\right) cos(4\omega_{rec}\tau). \tag{3.8}$$

As a function of the delay time τ, the density of the recombined components will oscillate at 4 ω_{rec}.

In addition to the index of refraction shift, the observed recoil frequency will also have a mean field shift [106]; the atoms in the $|\pm 2\hbar k_{rec}\rangle$ state have twice the mean field energy as those at rest due to the exchange term in the interatomic potential. Including both the mean field shift and the index of refraction, the frequency of the

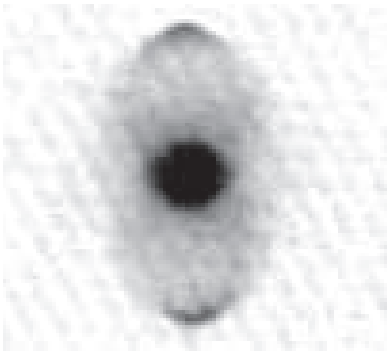

Figure 3-6: S-wave collision halos in time of flight. If the density of the condensate was two high atoms in the $|\pm 2\hbar k_{rec}\rangle$ momentum peaks collided with atoms at rest in the condensate during time of flight.

observed interference fringes should be:

$$\omega = 4n_r^2\omega_{rec} + \frac{\rho U_0}{\hbar}, \tag{3.9}$$

where $\rho U_0 = 4\pi\hbar^2 a\rho/m$, and a_s is the s-wave scattering length. The average density $\rho = 4/7\rho_o$, where ρ_o is the peak condensate density.

As given in Eq. (3.4), the index of refraction n_r is proportional to the density of the condensate ρ. To maximize the index of refraction effects, it would seem that using condensates with high initial density would be beneficial. However, although increasing the density does increase the index of refraction, using high density condensates also introduces a number of problems. Eq. (3.4) is only valid for $\rho\lambda\!\!\!^{-3} \ll 1$, if this condition is not met than additional corrections need to be made to the index of refraction, increasing the uncertainty in the result. In addition, if the condensate density is too high, the condensate becomes collisionally dense. As shown in Fig. 3-6, if the density is too high, in time of flight the outcoupled atoms collide with atoms initially at rest in the condensate creating a "halo" of scattered atoms which have undergone s-wave collisions. The condensate density was chosen to be as high as possible without creating appreciable s-wave collision halos in time of flight. The optimal density was found to be $\rho_o \approx 2 \times 10^{14} cm^{-3}$, which corresponded to a total condensate number of $N_o = 1.5 \times 10^6$ for our trap parameters. For this condensate density $\rho\lambda\!\!\!^{-3} \approx 0.2$.

The intensity of the pulse was set such that $\approx 5\%$ of the atoms were outcoupled into the $|\pm 2\hbar k_{rec}\rangle$ momentum states, this not only made the analysis of the resulting interference pattern easier by limiting the number of states, but also ensured that the condensate density remained approximately constant throughout the measurement. For a density of $\rho_o \approx 2 \times 10^{14} cm^{-3}$, the mean field shift to the resonance was almost 1 kHz, on the same order as the index of refraction effects. Any change in the density of the condensate during the measurement would have potentially masked the index of refraction effects. Due to both the density dependence of the index of refraction, and the mean field shift, it was essential to have consistent atom number from shot to shot, for all of the data the variation in the condensate number was <10% for the duration of the experiment.

3.5 The Recoil Frequency

The recoil frequency was measured by counting the number of atoms in either the $|0\hbar k_{rec}\rangle$ or the $|\pm 2\hbar k_{rec}\rangle$ momentum state and by then normalizing the signal to the total atom number, as a function of the delay time τ between pulses. Interference fringes for a detuning of $\Delta = 520$Hz are shown in Fig. 3-7. In the previous section the motion of the atoms during the delay time τ was ignored, however the amplitudes of the recombined components will only interfere if they spatially overlap. After the first pulse, the atoms in the $|\pm 2\hbar k_{rec}\rangle$ momentum states move within the initial condensate with the recoil velocity (~ 12 μm/ms). As the overlap between the recoiling atoms and those at rest decreases, the interference fringes decay. The overlap integral for this decay can be approximated as a Gaussian with time constant, $\tau_c \approx 0.75\ R_{TF}/v_{rec}$, where R_{TF} is the Thomas-Fermi radius of the condensate, and v_{rec} is the recoil velocity [116]. For our experimental parameters, $R_{TF} = 8\mu m$ in the radial direction giving a coherence time of 500μs. The experiments were performed perpendicular to the long axis of the condensate. The coherence time for the process could have been increased by instead performing the experiments along the long axis of the condensate, however, if the pulse was applied along the long axis the probability for collisions in time of

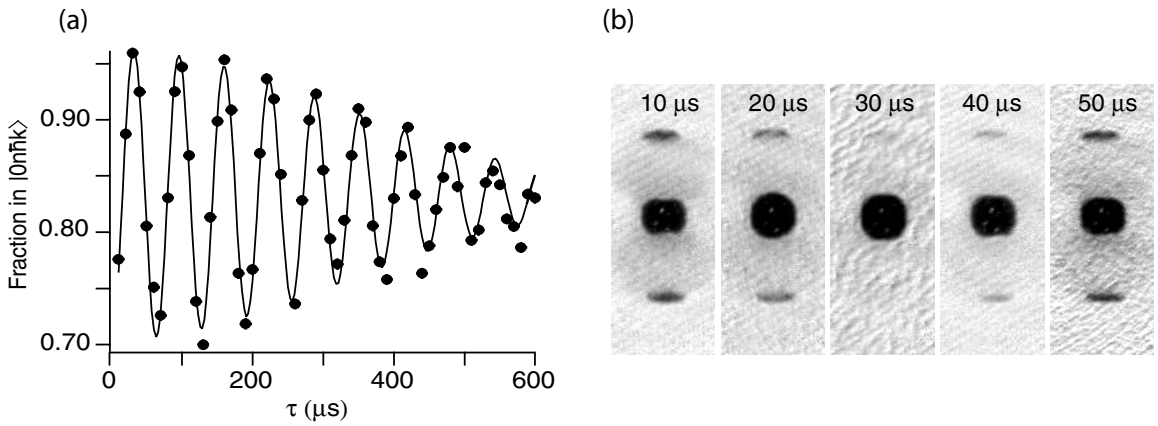

Figure 3-7: Interference fringes for $\Delta = 520$Hz. (b) The atom number in the $|0\hbar k_{rec}\rangle$ momentum state as a function of the hold time τ, showing interference fringes which oscillate at the recoil frequency. The fitted frequency was $\omega = 2\pi \times 156268(39)$ Hz and the decay constant $\tau_c = 461(25)$ μs. The signal was normalized using the total atom number in all momentum states. (a) Absorptions images for τ = 10-50μs showing the first period of the oscillation.The field of view is 0.5 mm $\times$ 1.5 mm

flight increased. To compensate for the increased collisions a lower density must be used negating any advantage to this geometry. The recoil frequency was found by fitting the resulting fringes to a cosine function with a gaussian envelope:

$$A \exp\left(-\frac{\tau^2}{\tau_c^2}\right) \cos(4\omega\tau + \phi) + C. \tag{3.10}$$

The expected values for A and C can be found from Eq. 3.8. The observation of up to ten oscillations provided a precise value of the recoil frequency. The fitted recoil frequency was found as a function of the laser detuning Δ, and the results are shown in Fig. 3-8. As the detuning was varied a shift of over 2kHz was seen across the resonance, whereas the statistical uncertainty in the points was $< 100Hz$ clearly showing that the recoil momentum is given by $|n_r\hbar k\rangle$.

When the pulse was applied the condensate density was lowered slightly due to spontaneous scattering from the laser beam. In order to accurately calibrate the density of the condensate a single 5 μs pulse was first applied to the atoms. The condensate number was then found by fitting a Thomas-Fermi profile to the integrated optical density of the absorption image in time of flight. Although the polarization of

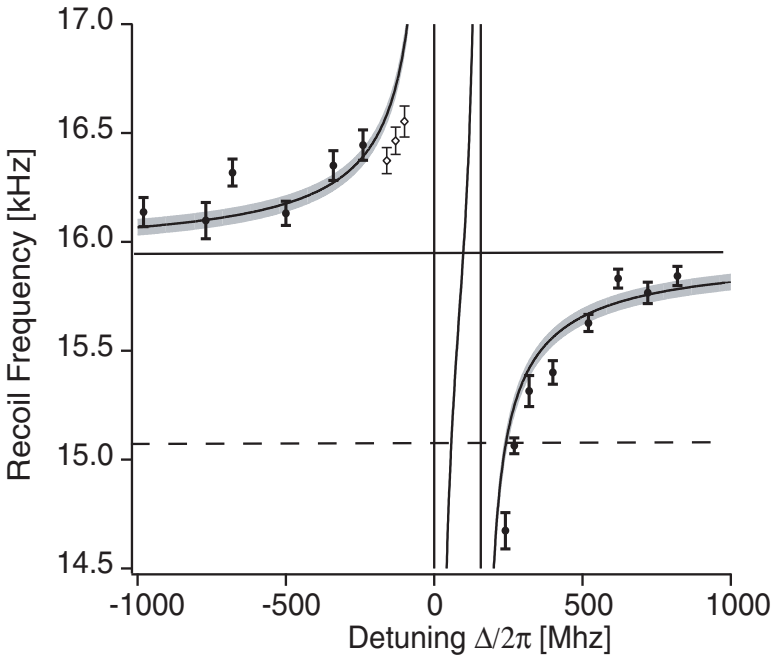

Figure 3-8: Recoil frequency as a function of detuning $\Delta/2\pi$ showing the dispersive effect of the index of refraction. The average density of the condensate for the solid points was $1.14(4) \times 10^{14}$ cm^{-3}, giving a mean-field shift of 880 Hz to the resonance. The shaded area gives the expected recoil frequency including the uncertainty in the density. The dashed line is at $\omega = 4n^2\omega_{rec} + \rho U_0/\hbar$, the expected value without index of refraction effects. The data shown as open diamonds had increased spontaneous light scattering due to $\sigma^{\pm}$ light contamination in the laser beam. The increased light scattering led to a lower initial density in the condensate, thus leading to a smaller mean-field shift and index of refraction. The open points have been scaled upward to correct for this lower density.

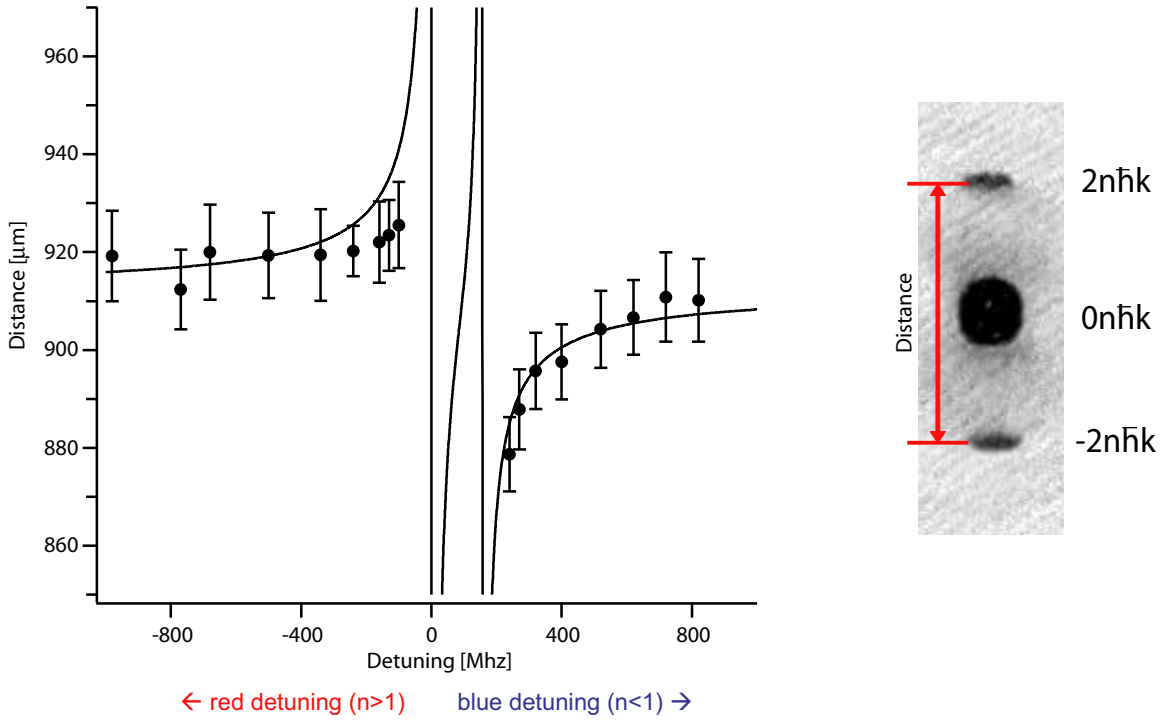

Figure 3-9: Separation between the $|\pm 2\hbar k_{rec}\rangle$ momentum peaks as a function of the laser detuning $\Delta/2\pi$. The separation between the peaks also shows the dispersive effect of the index of refraction.

the beam was set to be π-polarized (and this was optimized by minimizing Rayleigh superradiance), there was still a small amount of $\sigma^{\pm}$ contamination in the pulse. The $\sigma^{\pm}$ contamination allowed $\Delta m_F = \pm 1$ transitions, thus for small detunings the proximity to the $|1,-1\rangle \rightarrow |0',0\rangle$ transition located at $\Delta/2\pi = -72$ MHz resulted in higher spontaneous scattering rates, and a lower initial condensate density. Data points taken at these small detunings were shifted upward in Fig. 3-8 to compensate for this.

In addition to measuring the recoil frequency, one can also measure the separation between the $|\pm 2\hbar k_{rec}\rangle$ momentum peaks in time of flight. Once the atoms have been outcoupled they move with $v_{rec} = n_r \hbar k/m$, therefore the separation should also vary with the index of refraction. The separation as a function of the detuning Δ, is shown in Fig. 3-9. The separation between the peaks also clearly showed a dispersive shape, showing the dependence of the recoil velocity on the index of refraction.

3.5.1 Grating Picture

To understand the quadratic dependence of the recoil frequency on n_r, we can return to the grating picture discussed in section 2.2.1. When the light grating is incident on a dispersive media, the grating spacing goes from λ to λ/n_r. After diffracting off of the grating the velocity imparted to the atoms is also modified by n_r, with $v = n_r\hbar k/m$. When the second pulse is applied, the atoms have both moved farther by a factor of n_r and the grating is smaller by a factor of n_r leading to a change of the beat frequency on the order of n_r^2.

3.5.2 The Lorentz Force

The increase in the momentum transferred to the atoms can also be explained by considering the momentum transferred to atoms by a classical field [49]. Classically, the force applied to an atom with dipole moment $\vec{d}$ during the absorption of the photon can be found using the Lorentz force,

$$\vec{F}(t) = (\vec{d}\cdot\bigtriangledown)\vec{E}(x,t) + \frac{\partial\vec{d}}{\partial t}\times\vec{B}(x,t). \tag{3.11}$$

For a plane wave with π-polarization we have:

$$\vec{F}(t) = \frac{\partial\vec{d}}{\partial t}\times\vec{B}(x,t) \tag{3.12}$$

A two-level atom initially in its ground state will undergo Rabi oscillations with $\omega_R = \mu E_L/\hbar$, where μ is the dipole matrix element connecting the ground $|g\rangle$ and excited $|e\rangle$ states of the atom, and E_L is the Electric field of the applied laser pulse. At $t = \pi/\omega_R$ the atom will have absorbed a photon, and will be in the excited state. The instantaneous dipole moment during this interaction is given by $d \propto \mu\sin(\omega_R t)\exp(i\omega t)$. The change in momentum during the interaction with the field then is given by,

$$\Delta p = \int_0^{\pi/\omega_R} \mu\omega\sin(\omega_R t)B dt. \tag{3.13}$$

Evaluating this we find $\Delta p = \hbar\omega(B_L/E_L)$. The ratio of $B_L/E_L = n/c$, giving $\Delta p = n_r\hbar k$. More qualitatively one can understand this by considering the integration time for Eq. (3.13). If the index of refraction $n_r > 1$, the Rabi frequency ω_R is smaller and the integration time will be longer, thus the change in momentum due to the absorption of a photon in the medium will be larger than the vacuum momentum, the converse holds for $n_r < 1$.

However, the above derivation actually has two errors which luckily cancel each other. In calculating the force applied to the atoms the macroscopic electric field was used, but this is not correct. To calculate the force applied to the atom the microscopic force at the dipole must instead be used. As discussed in the derivation of the index of refraction, in Sec. 3.3, the microscopic electric field at a dipole within the cloud is given by $E_{eff} = E_L + E_{int} = E_L + \frac{1}{3\epsilon_0}P$. If the field is modified, then how is the result the same? In the initial derivation of the Lorentz force another error was made, the Lorentz force is given by

$$F = (d \cdot \bigtriangledown)E_{eff} + \dot{d} \times B_{eff} \tag{3.14}$$

for a nonmagnetic medium, B_{eff} can be replaced by B_L. However, the use E_{eff} in the first term results in a non-vanishing contribution. After much algebra[2], one can show that fortuitously the term due to the gradient of E_{eff} in the first term cancels out the change in the second term due to E_{eff} (which enters Eq. 3.13 through ω_R), and the result is still given by $n_r\hbar k$.

3.6 The Recoil Momentum in Bragg Processes

If the recoil momentum is in fact $n_r\hbar k$, as both the recoil frequency measurement and the separation between the peaks show, then this means that for momentum to be conserved, momentum must be left in the medium. Atoms which do not scatter photons are left with momentum even after the pulse has passed, and that momentum

[2]Which can be found in [90].

can be either parallel (n_r <1) or anti-parallel(n_r >1) to the direction of the light depending on the value of the index of refraction. In the experiments described above the atoms were outcoupled symmetrically using Kapitza-Dirac diffraction, therefore momentum was clearly conserved and this effect was not observable. However, if instead the length of the pulse was increased, and the lattice beams detuned to instead use Bragg scattering, it is possible that this effect could be resolved. In Bragg scattering atoms are only outcoupled in one direction with momentum $p = |2j\hbar k_{rec}\rangle$ for a j^{th} order Bragg process. If a large fraction of atoms are outcoupled, for example using a $\pi/2$ pulse, and for large values of j this effect could potentially be resolved in time of flight. Using a $\pi/2$ pulse, the momentum left in the $|0\hbar k_{rec}\rangle$ state would be $p = 2j(n_r - 1)\hbar k\rangle$. Measuring this with a condensate is complicated by two considerations; for Bragg scattering the length of the pulse is a factor of 100 times longer. Using near resonant light (to maximize the change in the index of refraction), the spontaneous scattering rate can be quite high, to compensate for the longer pulse length the detuning of the beam must be increased. This in turn decreases the index of refraction effect. However, as an example, using a detuning of $\Delta = 1$ GHz, with a j^{th} order Bragg pulse, v_{rec}=0.05j μm/ms for the $|0\hbar k_{rec}\rangle$ momentum state in time of flight. For a 100ms time of flight this is over 5μm! But resolving this change is complicated by mean-field effects. For large outcoupling the position of the $|0\hbar k_{rec}\rangle$ state can also change position due to mean-field repulsion between the outcoupled atoms and those at rest making the index of refraction effects difficult to distinguish.

Chapter 4

Parametric Generation and Amplification of Scattered Atom Pairs

This chapter describes parametric generation and amplification of scattered atom pairs, and supplements work previously reported in Ref [13], which is also included in Appendix B

4.1 Nonlinear Atom Optics

In Chapter 3, a measurement of the photon recoil momentum in dispersive media, an important consideration for atom optics, was discussed. Another rapidly growing field is nonlinear atom optics [73]. In nonlinear optics, since photons are noninteracting a nonlinear medium must be used to provide effective interactions. However, in nonlinear atom optics using Bose-Einstein condensates, the nonlinearity is provided by s-wave collisions within the condensate. Using condensates a number of nonlinear processes first demonstrated with photons have been demonstrated with matter-waves, including four-wave mixing [23, 118], solitons [24, 10, 4, 109], second-harmonic generation [122, 1, 74, 78], and sum-frequency generation [1]. One of the driving forces behind nonlinear atom optics is to find an efficient way to create en-

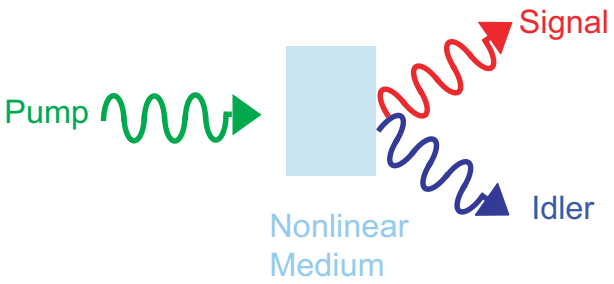

Figure 4-1: Optical parametric generation of photons. A pump beam is incident on a nonlinear medium, creating a signal and idler beams.

tangled pairs of atoms for quantum information processing. In particular four-wave mixing has previously been suggested as a promising way to create pairs of momentum entangled atoms [27, 93, 118].

4.2 Can a Condensate Collide with Itself?

Another possible way to create pairs of momentum entangled beams is the matter-wave analogue of Optical Parametric Generation (OPG)[94]. In optical parametric generation of photons, as shown in Fig. 4-1, a probe laser is sent into a nonlinear medium to create a signal and idler, where $2\hbar\omega_p = \hbar\omega_S + \hbar\omega_I$. Given the nonlinear interaction in condensates, is the matter-wave equivalent to an OPG possible? In the matter-wave analogue, as shown in Fig. 4-2, two atoms in the condensate with velocity v_0, collide to create one "red" atom with lower velocity v_1, and one "blue" atom with higher velocity v_2. Clearly momentum can be conserved in this collision, but as was discussed in Section 1.5, the excitation spectrum for the condensate is quadratic for particle-like excitations. As shown in Fig. 4-2(b), for final states equally spaced in momentum space, energy is not conserved. It would appear that the matter-wave analogue of OPG is not possible. Four-wave mixing has been previously demonstrated with condensates, where two atoms with initial velocity v_1 and v_2 scatter into final states v_3 and v_4. However, in these experiments [23, 118] using condensates in free space, the quadratic dispersion relation for free particles only allowed for the phase-matching condition to be fulfilled when the magnitudes of all four momenta were

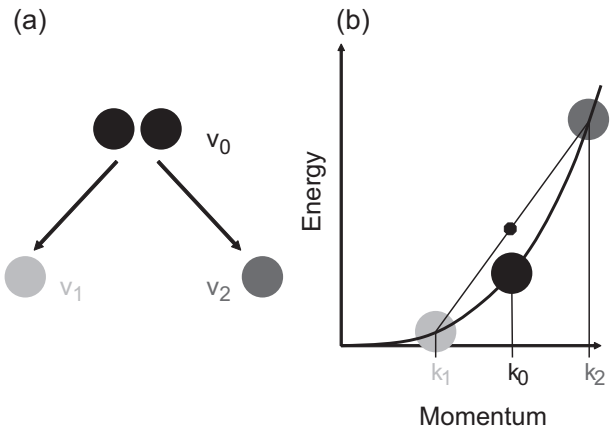

Figure 4-2: Can a condensate collide with itself? (a) In the matter-wave analogue to OPG, two atoms in the condensate with initial velocity v_0 collide and scatter into final states v_1 and v_2. (b) Due to the quadratic dispersion relation, it is not possible to conserve both energy and momentum in this collision. Given final momentum states k_0, k_1, and k_2 equally spaced in momentum space, the average of the final energies clearly exceeds the initial value.

equal (in the center-of-mass frame), and the final momentum states could only be distinguished if the experiments were performed in two dimensions.

4.2.1 Collisions in a 1D Optical Lattice

But what happens if instead a 1D optical lattice is added to the system? As discussed in Chap.2, in a lattice the motion of the atoms is described by a band structure, where for even shallow lattices the dispersion relation is no longer quadratic near the boundary of the first Brillouin zone. As shown in Fig. 4-3 it now becomes possible to find pairs of quasimomentum states k_0, k_1, and k_2 where both momentum and energy can be conserved [50].

The phase matching condition for the scattering process is given by

$$2k_0 = k_1 + k_2 \tag{4.1}$$

$$2\epsilon(k_0) = \epsilon(k_1) + \epsilon(k_2) \tag{4.2}$$

where $\epsilon(k_i)$ is the energy of atoms in the quasimomentum state k_i, determined from a band structure calculation. In the optical lattice the conserved quantity is qua-

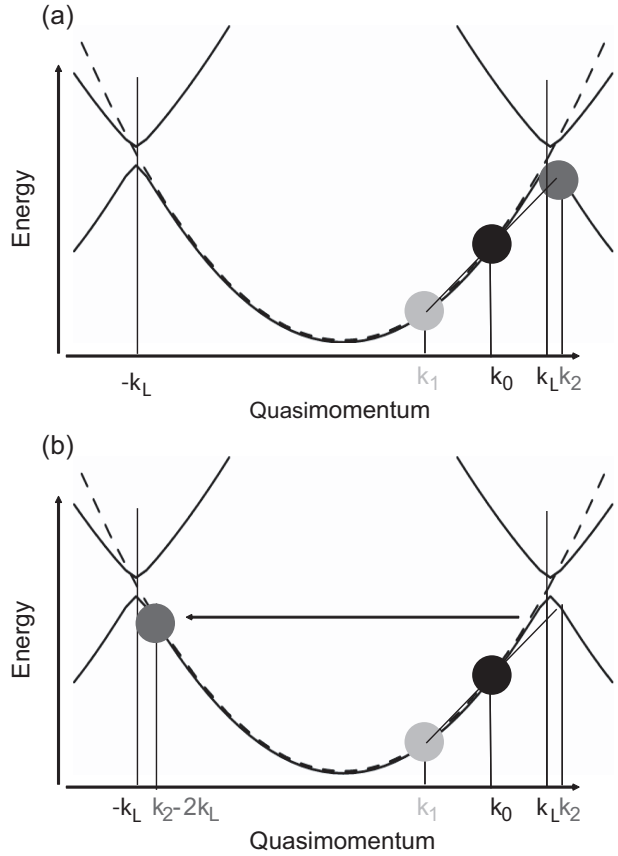

Figure 4-3: Collisions in a 1D optical lattices. If a 1D lattice is added, the dispersion curve is no loner quadratic near the boundary of the first Brillouin zone. It now becomes possible to find phase matched quasimomentum states k_0, k_1 and k_2 where both energy and momentum can be conserved. (a) Phase matched momentum states are shown for a lattice depth of $V_{latt} = 0.5E_{rec}$. The dispersion curve is shown for the ground and first excited band. The boundary of the first Brillouin zone is at $\pm k_L$, where k_L is the wavevector of the optical lattice. (b) Since the phase matched momentum state k_2 is beyond the boundary of the first Brillouin zone, the final momentum state is mapped back into the first Brillouin zone at $k_2 - 2k_L$.

simomentum, and the quasimomentum is restricted to be between values of $\pm k_L$, therefore

$$k_2 = (2k_0 - k_1)\, Mod(2k_L). \tag{4.3}$$

If a one-dimensional optical lattice is added, it becomes possible to realize the matter-wave analogue to OPG, and a condensate can in fact collide with itself!

4.3 Parametric Generation

To demonstrate parametric generation with atoms, the condensate must first be prepared at an initial quasimomentum k_0. To do this one has two options, one can either create a condensate with an initial velocity v_0, or one can instead use a moving lattice. Technically, it is much easier to create a moving lattice, so for our experiments the second option was chosen.[1] As shown in Fig. 4-4, two counter-propagating laser beams with frequency difference $\delta\nu = \nu_2 - \nu_1$ were used to create a moving one-dimensional lattice with velocity $v = \frac{\lambda}{2}\delta\nu$. The lattice was ramped onto a magnetically trapped condensate initially at rest. In the rest frame of the lattice the condensate had quasimomentum $k_0 = \frac{m\lambda}{2\hbar}\delta\nu$. For a given value of k_0, there is only one set of states k_1 and k_2 where the phase matching condition is met, and as the value of k_0 is varied the phase matched momentum states also vary. In Fig. 4-4(b), the phase matched momentum states are shown for two values of k_0.

When a moving lattice was applied to the condensate, as shown in Fig. 4-4(c), as the value of k_0 was varied elastic scattering of atom pairs into final momentum states k_1 and k_2 was observed. As the value of k_0 was increased the final momentum states moved closer towards the edge of the Brillouin zone, as was expected. This process is analogous to Optical Parametric Generation, where instead of scattering two pump photons into one red photon and one blue photon, we have instead scattered two atoms into a higher and lower momentum state. For values of k_0 below $\approx 0.55k_L$, the dispersion relation imposed by the lattice did not allow for phase-matched final

[1] Although as will be discussed in Chapter 6, technical issues due to vibrations can be difficult to overcome in moving lattices.

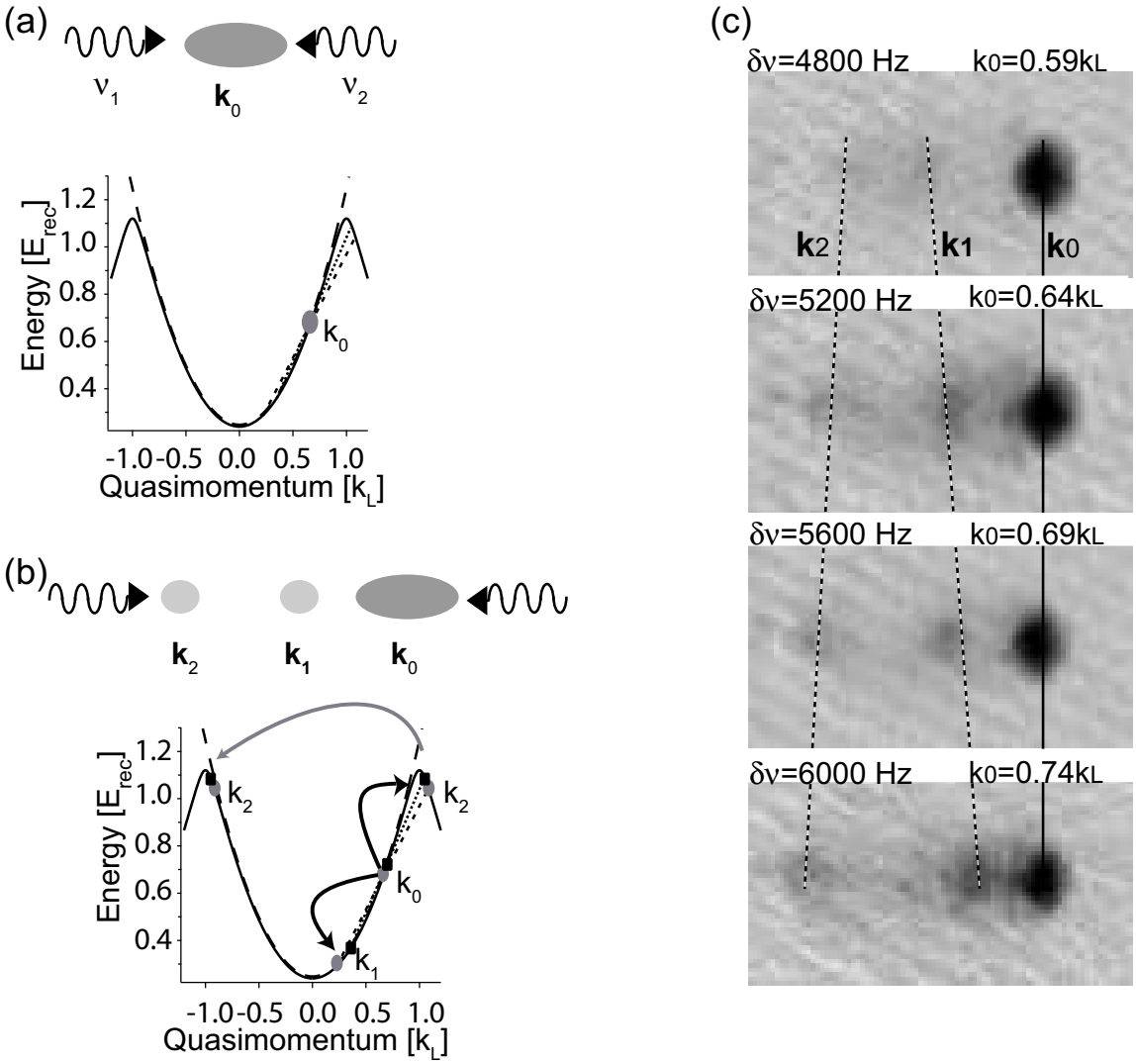

Figure 4-4: Parametric generation of scattered atom pairs. (a) A moving lattice was created using two counter propagating laser beams with frequency difference $\delta\nu = \nu_2 - \nu_1$ between the beams. In the rest from of the lattice the condensate has quasimomentum $k_0 = \frac{m\lambda}{2\hbar}\delta\nu$. (b) For a given value of k_0, there is only one pair of states k_1 and k_2 where the phase matching condition is fulfilled. If k_0 is varied, the allowed values for k_1 and k_2 change. The circles (squares) show allowed states k_0, k_1, k_2 for k_0 =0.66k_L (0.70k_L). As k_0 is increased, the final momentum states move closer together. The lattice depth was V_{latt}=0.5E_{rec}. (c)Absorption images showing parametric generation. As k_0 was varied, elastic scattering into final momentum states k_1 and k_2 was observed. After ramping up the lattice, the atoms were held for 10 ms at a constant lattice depth. The atoms were then released from the trap and imaged after 43 ms time of flight. The field of view is 0.5 mm×0.3 mm.

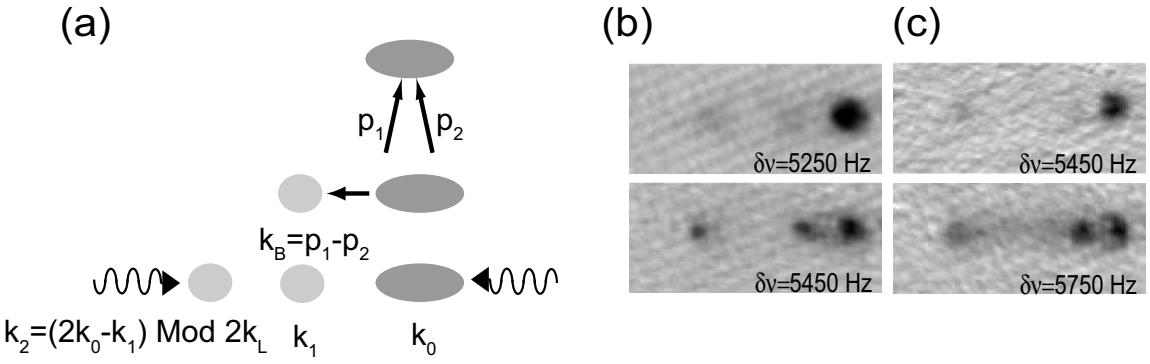

Figure 4-5: Parametric amplification of scattered atom pairs. (a) First, a 2 ms Bragg pulse was applied to the condensate. The Bragg pulse outcoupled a small fraction of atoms along the long axis of the condensate with momentum $k_B = (k_a - k_b)$ in the lab frame. The optical lattice was then adiabatically ramped on and applied for 10 ms. When the phase matching condition was fulfilled, parametric amplification of atoms was observed in the seeded state k_1 and its conjugate momentum state k_2. (b,c) Absorption images taken for two different Bragg angles. In (b) the Bragg wavevector was k_B=0.43k_L, and in (c) the Bragg wavevector was k_B=0.34k_L. In the top two images, the phase matching condition was not met, and only the initial seed and a small amount of spontaneously scattered atom pairs are visible. In the bottom pictures k_0 and k_1 have been tuned to fulfill the phase matching condition by varying the detuning $\delta\nu$. When the phase matching condition was fulfilled amplification of the initial seed and its conjugate momentum state was observed.

momentum states and no scattering was observed. For values of k_0 above $\approx 0.75k_L$, the final momentum states were no longer distinguishable, and the condensate became unstable.

4.4 Parametric Amplification

If the matter-wave analogue to OPG is possible, then if the process is first seeded the matter-wave analogue of Optical Parametric Amplification (OPA) should also be possible. To demonstrate the matter-wave analogue of an OPA, as shown in Fig. 4-5, a small seed of atoms was first created by applying a Bragg pulse to the atoms. The effect of the Bragg pulse was to outcouple a small fraction of atoms into the state k_B. Immediately after applying the pulse the lattice was ramped on. In the rest frame of the lattice, the seed has quasimomentum $k_1 = k_0 + k_B$. As with OPG, for a given

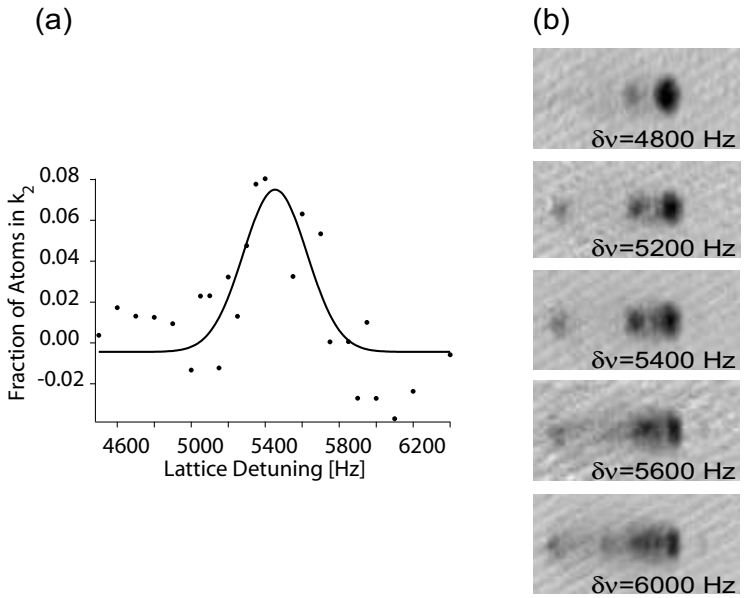

Figure 4-6: Scattering resonance for parametric amplification of atoms. (a) Resonance curve showing amplification of k_2, when k_1 was seeded. Amplification occurred only when the phase-matching condition was met. For a fixed k_B, the resonance condition was found by varying the detuning $\delta\nu$ of the lattice. The data was taken for $k_B = 0.43k_L$. The fraction of amplified atoms was obtained by subtracting images with and without the seed pulse. (e) Absorption images showing amplification of k_1 and k_2 when the phase matching condition is met. The center of the resonance was at $\delta\nu \approx$ 5450Hz, close to the calculated value of $\delta\nu \approx$ 5350Hz. The width of the resonance is determined by the Fourier width of the Bragg pulse. Most of the scattered atoms in the third image were independent of the pulse.

value of k_0, the phase matching condition is only met for one set of states k_1, and k_2. However, to find the phase matching condition k_0 and k_1 could not be varied independently; the difference k_1 - k_0 is set by the initial Bragg pulse. The phase matching condition was found by changing both k_0 and k_1 by varying the detuning $\delta\nu$. As shown in Fig. 4-6, when the phase matching condition was met amplification of the seed k_1 as well as its conjugate momentum k_2 was observed. The growth of k_1 and k_2 as a function of time is shown in Fig. 4-7.

In Fig. 4-7, less than 5% of the initial condensate was outcoupled by the initial Bragg pulse with $k_B = 0.43k_L$. The gain for the process is determined by the strength of the nonlinear interaction, U_0 between atoms in the condensate. For a shallow lattice $U_0 = \frac{4\pi\hbar^2 a_s}{m}$, where a_s is the s-wave scattering length. From this we can estimate the

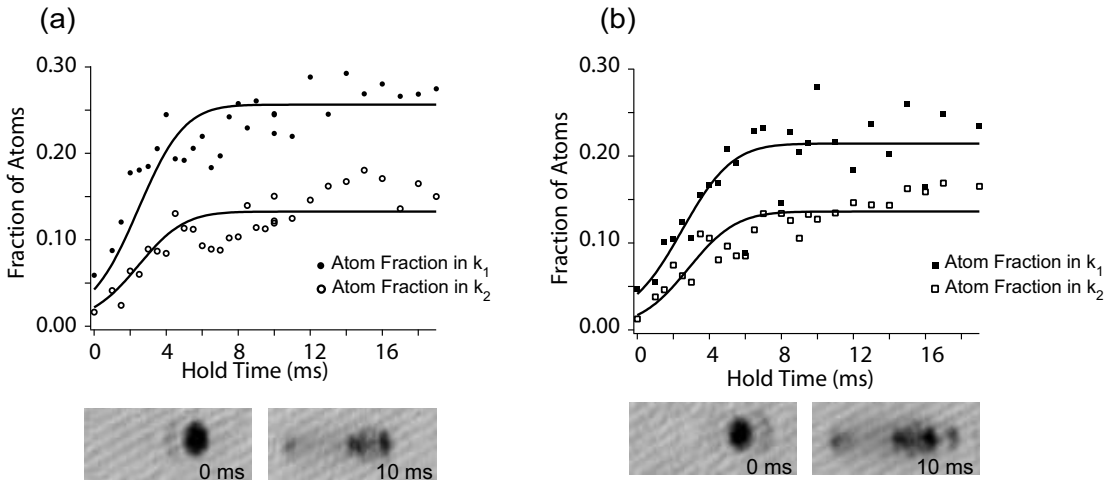

Figure 4-7: (a) Amplification of atoms with quasimomentum k_1 (solid points), and with conjugate momentum k_2 (open points), when state k_1 was seeded. (b) Amplification of atoms with quasimomentum k_1 (solid points), and with the conjugate momentum k_2 (open points), when state k_2 was seeded. The values for k_0,k_1,k_2 were $0.66k_L$,$0.23k_L$,and -$0.92k_L$ respectively. The solid lines shows the expected gain using Eq. (4.4) with variable scale factors for each curve as the only free parameters.

maximum amplification rate to be $\eta = 2\rho_0 U_0/\hbar$ [118], with $\dot{N}_{1(2)} = \eta N_1$, where $N_{1(2)}$ is the number of atoms in the momentum state $k_{1(2)}$. For the data shown in Fig. 4-7, the condensate number was $N_0 = 1.3(3)\times10^5$. For this atom number, the maximum growth rate should be $\eta = 540$ Hz. The amplification rate will decrease as the number of atoms in the initial condensate, in quasimomentum state k_0, is depleted. However, for our small seeds, the amplification was not limited by this depletion of the source but instead, was limited by the loss of overlap between the condensate and the amplified pulses. The Thomas-Fermi radius (R_{TF}) of the condensate in the axial direction was 33 μm, and the recoil velocity (v_{rec}) for the final states k_1 and k_2 with respect to the initial condensate was v_{rec}=1.8 μm/ms and 6.8μm/ms respectively. The overlap integral between the amplified atoms and the initial condensate can be approximated as a Gaussian with time constant $\tau_c \approx 0.75R_{TF}/v_{rec}$, which for our parameters is 3.75 ms. Including this loss of overlap gives us a modified rate equation,

$$\dot{N}_{1,2} = \eta N_1 e^{\frac{-t^2}{\tau_c^2}} \tag{4.4}$$

Since atoms are scattered into states k_1 and k_2 in pairs, the final atom number in those two states (minus the initial seed) should be equal. Instead, the final atom number in k_2 was approximately a factor of 2 smaller than that in k_1. This is due the proximity of k_2 to the boundary of the Brioullin zone. This leads to instabilities where atoms are scattered into other momentum states or into higher bands. Allowing a variable scale factor to correct for this in our model, the experimental data followed Eq. **??**eq:rate).

4.5 Experimental Setup

The experiments were performed using condensates initially prepared in a magnetic trap. The magnetic trap was cigar shaped with a radial trap frequency of 35 Hz, and an 8 Hz axial trap frequency. The condensate, containing between $0.5 - 3.0 \times 10^5$ atoms was produced in the $|5^2S_{1/2}, F = 1, m_F = -1\rangle$ state. The optical lattice was created using two counter-propagating beams derived from the same laser with $\lambda = 1064$nm, and the frequency of the two beams was controlled by two separate acousto-optic Modulators (AOMs) driven with a frequency difference $\delta\nu$. The lattice was also aligned along the long axis of the condensate, and was ramped on in 1 ms using an exponential ramp. The Bragg pulse was created with two laser beams derived from the same laser, which was red-detuned from the $5^2S_{1/2}, F = 1 \rightarrow 5^2P_{3/2}, F = 1$ transition at $\lambda = 780$nm by 400MHz, and was π-polarized to minimize Rayleigh superradiance. As shown in Fig 4-5, the Bragg beams were aligned such that atoms were outcoupled along the long axis of the condensate. The intensity of the Bragg pulse was chosen such that less than 5% of the initial condensate was outcoupled into the state k_B, and the length of the pulse was 2ms. The angle between the Bragg beams could be varied to change the momentum of the outcoupled atoms. After the condensate was held in the lattice for a variable time τ it was then released from the trap and imaged after 43 ms of ballistic expansion.

The time scales for the lattice ramp up and the Bragg pulse were both very important. Due to the coherence length of the condensate, the time scale for the

experiment was limited to $< 10ms$ (as can be seen from Fig. 4-7) therefore, in order to measure the gain it was important to ramp up the lattice as quickly as possible, while still maintaining adiabaticity. As shown in Fig. 2-5, as the initial quasimomentum k_0 is increased this becomes more difficult. For our lattice wavelength of $\lambda = 1064$ nm, $E_{rec} = 2$ kHz setting the lower bound on the ramp time. Our 1 ms ramp time was chosen to be the fastest ramp possible while still being adiabatic with respect to k_0.

Due to the limited optical access of our machine, atoms could not be seeded directly into k_2 = -0.92k_L for the growth curve shown in Fig. 4-7(b). However, due to the proximity of k_2 to the boundary of the Brillouin zone, the 1 ms ramp up was no longer adiabatic. Because of this, if atoms were instead seeded into the state $k = 1.08k_L$, atoms from the seed were loaded into both the second Bloch band (with $k = 1.08k_L$) and the ground state (with k = -0.92$k_L = k_2$). As shown in Fig. 4-7(b), the gain in this case was almost identical to when the atoms were seeded in state k_1.

The 2ms length of the Bragg pulse was also limited by the coherence length of the condensate. The width of the scattering resonance shown in Fig. 4-6 was limited by the Fourier width of the Bragg pulse, therefore it is beneficial to make the Bragg pulse as long as possible. However, once the Bragg pulse has been applied the outcoupled atoms recoil within the initial condensate. Since the length of the Bragg pulse was on the same order as the time scale for the amplification the pulse was applied before the lattice was ramped on.

4.6 Dynamic Instabilities in Optical Lattices

With longer coherence times parametric amplification could be used to produce pairs of momentum entangled atoms, however first the problem of secondary collisions out of the final state k_2 must be solved. Since secondary collisions were primarily caused by the proximity of k_2 to the boundary of the Brillouin zone, one way of addressing this issue is to find phase matched momentum states with k_2 farther from the edge. As shown in Fig. 4-8, this could be accomplished by increasing the lattice depth. However, as the lattice depth is increased the phase matched momentum states also

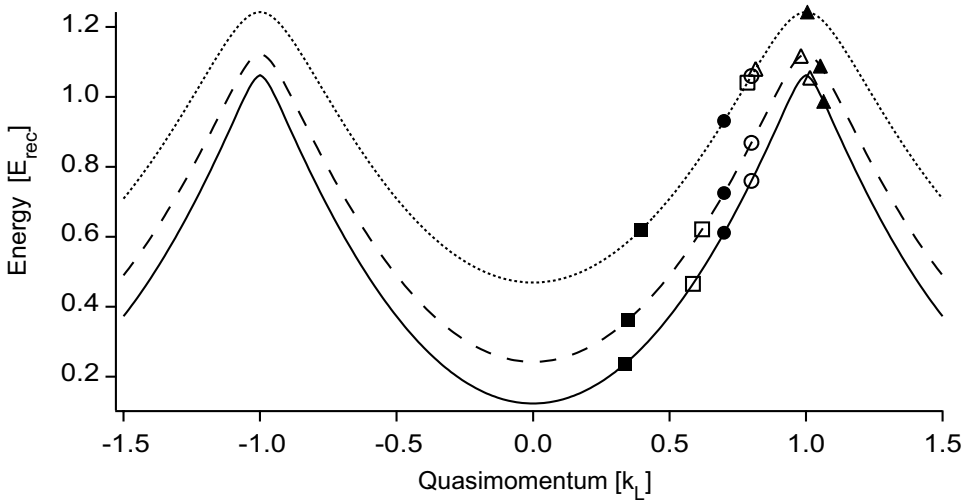

Figure 4-8: Phase matching condition for different lattice depths. The phase matched momentum states are shown for $k_0 = 0.7k_L$ (solid points) and $k_0 = 0.8k_L$. For lattice depths of $V_{latt} = 0.25E_{rec}$(solid line), $0.5E_{rec}$ (dashed line), and 1 E_{rec} (dotted line). As the lattice depth is increased the phase-matched momentum states move closer together.

move closer together, and this leads to dynamic instabilities.

Longer coherence times and larger gain could be created by using condensates with higher atom number.[2] However, when the experiments were performed with either higher atom numbers, or with large values of k_0, the condensate became unstable, and scattered into a broad band of final momentum states. For $k_B = 0.43k_L$, the energy of atoms outcoupled by the Bragg beams was ≈ 370 Hz, whereas the chemical potential of the condensate was ≈ 300 Hz. Because of this, if the atom number was increased significantly the momentum peaks were no longer distinguishable. When the chemical potential of the condensate was larger than the separation between the phase matched momentum states the process was self-seeded, i.e the momentum spread of the initial condensate contained atoms with momentum k_0, k_1,and k_2, and considerable scattering occurred. This can be seen in Fig. 4-9, where the growth is compared for two different condensate numbers.

Similarly, if the atom number was kept constant, and the value of k_0 was increased, the phase-matched momentum states moved closer together until they too were no

[2]The gain is increased due to the higher density, and the coherence time is increased due to the larger radius.

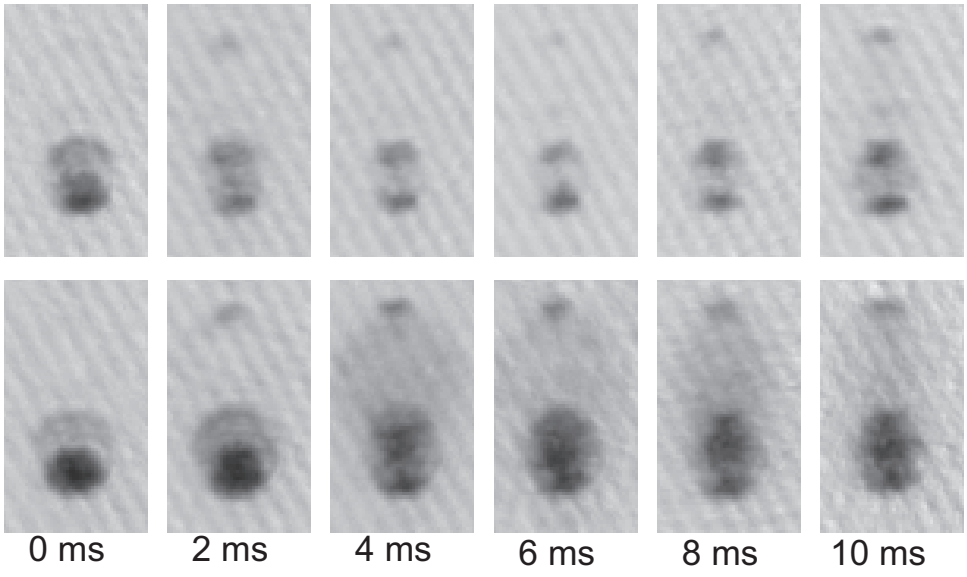

Figure 4-9: Effect of atom number on instabilities. Optical Parametric Amplification is shown for two different atom numbers. (a) For small atom numbers the chemical potential of the condensate was smaller than the energy of atoms outcoupled by the Bragg pulse. The phase matched momentums states were distinguishable and atoms were only scattered into k_0, k_1 and k_2. (b) For larger atom number, the chemical potential become comparable to, or larger than the separation between the phase matched momentum states. The final states were no longer distinguishable, the process became self-seeded and atoms were scattered into a range of final states.

longer distinguishable. For our density, this occurred at values of k_0 above $\approx 0.75k_L$, and we observed a dynamic instability. If the lattice depth is increased the phase matched momentum states also move closer together. For both larger atom number, and higher lattice depth, the critical value of k_0 leading to instabilities decreases. For values of k_0 less than $0.55k_0$ elastic scattering cannot occur, and the system should be stable for all atom numbers. Instabilities of condensates in optical lattices has attracted much attention recently, both theoretically [121, 103, 75, 69, 102, 125, 81, 115] and experimentally [11, 14, 19, 30, 97]. Dynamic instabilities of condensates in moving lattices were observed in Ref. [30, 97], in Ref. [97], the chemical potential was a factor of 3 higher than in our experiment, leading to a dynamic instability for all values of k_0 above $0.55k_L$. Although discrete momentum states could not be observed in those experiments, it is possible that the mechanism for the dynamic instability is self-seeded parametric amplification. Indeed, the phase-matching condition for parametric amplification is identical to the resonance condition for dynamic instability in the noninteracting limit [121].

Chapter 5

The Superfluid to Mott Insulator Transition in Ultracold Atoms

In the previous chapter, a one-dimensional optical lattice was used for nonlinear atom optics, where the lattice was used to modify the dispersion relation. Even though the dispersion curve was modified, the condensate was still delocalized over the entire lattice. The condensate was still a superfluid, and could be described with a macroscopic wavefunction. This is only true for shallow optical lattices where the tunneling energy is large. In this chapter, the behavior of condensates loaded into deep optical lattices is discussed. As the lattice depth is increased, atom-atom interactions start to dominate as the tunneling rate decreases. The system undergoes a phase transition from a delocalized condensate, to a localized insulating state, from a superfluid to a Mott Insulator (MI).

This chapter starts with a simple double well model which qualitatively describes the physics of the superfluid-to-MI transition. The double well model is then generalized to a full lattice, and the Bose-Hubbard model is derived. The phase transition for the superfluid-Mott Insulator (MI) transition with ultracold atoms is also calculated. Finally the effects of the external confinement on the phase transition are discussed.

5.1 The Double Well Model

The behavior of atoms loaded into a deep optical lattice can qualitatively be understood by first examining a double well potential. If the atoms are held in two wells with a potential barrier between the wells, where the height of the barrier can be varied independently, the hamiltonian for the system is given by [85]

$$H = \gamma \left(a_L^\dagger a_R + a_R^\dagger a_L \right) + g\beta/2 \left((a_L^\dagger a_L)^2 + (a_R^\dagger a_R)^2 \right), \tag{5.1}$$

where γ is the tunneling or hopping term between the wells, and $g\beta$ is the mean field energy per atom due to the atom-atom interactions in a single well. The behavior of this system is determined by the ratio of $Ng\beta/\gamma$. When $Ng\beta/\alpha << 1$, the atom-atom interactions are negligible. In the ground state of the system the atoms exist in an equal superposition of the left and right well given by the symmetric state $|S\rangle = 1/\sqrt{2}(|L\rangle + |R\rangle)$. For large N, the ground state of the system is a coherent state, with mean atom number $N/2$ per well, and with number fluctuations $\sigma_n \sim \sqrt{N/2}$, which are Poissonian in this case. For $Ng\beta/\alpha >> 1$ the atom-atom interactions dominate the behavior of the system. The ground state of the system becomes independent Fock states (since there is no longer a coupling term between the wells), where there is a fixed number of atoms per site, $N/2$ and $\sigma_n = 0$. As the value of $Ng\beta/\alpha$ is varied, by increasing the barrier between the wells, σ_n decreases and number fluctuations go to zero.

5.2 Quantum Phase Transitions

In classical phase transitions, the temperature dependent free energy of the system is minimized. The state of the system exhibits a discontinuity, which leads to a phase transition. At zero temperature such classical phase transitions are frozen out, but quantum fluctuations still exist due to the Heisenberg uncertainty relation, and the system can undergo quantum phase transitions [95]. When an external parameter is varied, a ground state with a different symmetry can appear, and the system can

find a new ground state in a finite time due to quantum fluctuations. In contrast, classical phase transitions are driven by temperature fluctuations. An example of a quantum phase transition is the superfluid-MI transition, which is a second order quantum phase transition.

5.3 Bose-Hubbard Model

To model the optical lattice we generalize our double well system to the full lattice system. Starting with the Hamiltonian given in Eq. (1.20), the external potential is now given by $V(\vec{r}) = V_{ext}(\vec{r}) + V_{latt}(\vec{r})$ (where the lattice potential V_{latt} is given in Eq. (2.22)). Expanding ψ in terms of the Wannier functions as $\psi(\vec{r}) = \sum_i a_i w_i(\vec{r})$(the Wanner functions are given in Eq. (2.27)) gives

$$\begin{aligned} H =& \sum_{\langle i,j \rangle} a_i^\dagger a_j \int d\vec{r} w_i(\vec{r}) \left(\frac{\hbar^2}{2m} \nabla^2 + U_{lat} \right) w_j(\vec{r}) \\ &+ \sum_i a_i^\dagger a_i^\dagger a_i a_i \frac{4\pi a_s \hbar^2}{2m} \int d\vec{r} |w_i(\vec{r})|^4 + \sum_i a_i^\dagger a_i \int d\vec{r} |w_i(\vec{r})|^2 U_{ext}. \end{aligned} \tag{5.2}$$

This can be rewritten as the familiar Bose-Hubbard Hamiltonian[58, 32],

$$H = -J \sum_{\langle i,j \rangle} a_i^\dagger a_j + \frac{1}{2} U \sum_i n_i(n_i - 1) + \sum_i (\epsilon_i - \mu) n_i, \tag{5.3}$$

where $J = \int d\vec{r} w_i(\vec{r}) \left(\frac{\hbar^2}{2m} \nabla^2 + U_{lat} \right) w_j(\vec{r})$ is the tunneling term between nearest neighbors, $U = \frac{4\pi a_s \hbar^2}{2m} \int d\vec{r} |w_i(\vec{r})|^4$ is the repulsive onsite interaction, $n_i = a_i^\dagger a_i$ is the number operator for bosons at site i, $\epsilon_i = \int d\vec{r} |w_i(\vec{r})|^2 U_{ext} \approx U_{ext}(\hat{r_i})$, is the energy offset at the i^{th} site due to the external confinement, and μ is the chemical potential. For deep lattices, the Wannier function on a given lattice site $w_i(\vec{r})$, can be approximated as the ground state of the harmonic oscillator, and the numerical values for U and J can be easily calculated[1]. For lower lattice depths, the values can be calculated using the wavefunctions found from the single particle band structure

[1]see Ref. [57] for a comparison of this approximation to numerical calculations of U and J.

calculation shown in Chapter 2.

5.3.1 The Mott Insulator Transition

As in the double well case the kinetic energy, or tunneling term, tends to delocalize particles over the lattice site, and minimizes phase fluctuations. The ground state of the system is a coherent state with N atoms. This is equivalent to the behavior we've seen in previous chapters where the condensate is a superfluid and can be described with a macroscopic wave function

$$|\psi_{SF}\rangle \propto \left(\sum_{i}^{s} a_i^\dagger\right)^N |0\rangle, \tag{5.4}$$

where s is the number of lattice sites, and the site occupation shows Poissonian number statistics. However, as the lattice depth is increased, as in the double well system the behavior changes dramatically. As the lattice depth is increased, the tunneling rate decreases exponentially and atom-atom interactions dominate the behavior of the system. The effect of the interactions is to localize atoms to individual lattice sites, and to minimize number density fluctuations. The system undergoes a phase transition to a MI state, which can no longer be described by a macroscopic wavefunction, but instead is described as a product of Fock states

$$|\psi_{MI}\rangle \propto \prod_{i}^{s} (a_i^\dagger)^n |0\rangle, \tag{5.5}$$

where n is the number of atoms in the lattice site. In the MI phase there are no number fluctuations, the per site occupation number is completely determined and the system has perfect number correlations.

5.3.2 Calculating the Phase Diagram

If we ignore the effect of the external potential (i.e set $\epsilon_i = \mu$ to a constant value), the phase diagram for the Superfluid-to-MI transition can be calculated by minimizing

the ground state energy [32, 95]. To calculate the phase diagram it is easiest to first examine the system when $J = 0$, when there is no tunneling. Minimizing the onsite energy, $H_i = \frac{U}{2}(n_i(n_i - 1) - \mu n_i)$, gives

$$\frac{2H_i}{U} = n_i[n_i - (1 + 2\mu/U)]. \tag{5.6}$$

The solution gives regions with different atom number per site, where the boundary is given by the degeneracy points. The onsite energy is minimized if each site i is occupied by exactly n atoms. For $J \neq 0$ one can use a mean-field parametrization where we construct H as the sum of the single site Hamiltonians

$$H_{MF} = \sum_i \left(-\mu n + \frac{Un(n-1)}{2} - \psi_{MF}^\dagger a - \psi_{MF} a^\dagger \right), \tag{5.7}$$

where ψ_{MF} is a variational parameter which describes the interaction with adjacent sites. Since the MI transition is a second order phase transition, we can expand the ground state energy in terms of ψ_{MF}, the variational parameter, as $E_0 = E + r|\psi_{MF}|^2$. Combining the mean-field and Bose-Hubbard Hamiltonians and using second-order perturbation theory to minimize the energy one finds an expression for r in terms of μ/U [95]

$$r = \frac{X(\mu/U)}{U}\left[1 - zJ\frac{X(\mu/U)}{U}\right] \tag{5.8}$$

$$X(\mu) = \frac{n(\mu) + 1}{n(\mu) - \mu} + \frac{n(\mu)}{(\mu + 1) - n(\mu)} \tag{5.9}$$

where $n(\mu)$ is the number of atoms per site, and z is the number of nearest neighbors which is determined by the dimensionality of the system. For a 3D lattice $z = 6$. For $J = 0$, the value of r changes from positive to negative at the boundary of the phase transition where the occupation number changes by 1. Similarly, for values of $J > 0$, solving $r = 0$ gives the boundaries of the phase transition.

Fig. 5-1 shows the phase diagram as a function of μ/U, the chemical potential to the onsite interaction. As we move towards a boundary by increasing μ, we reach

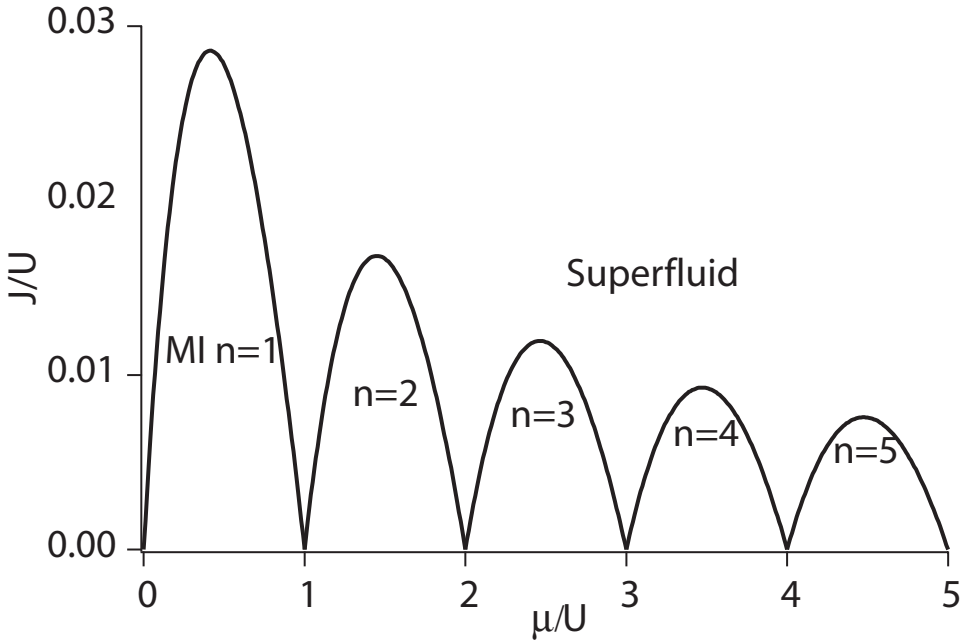

Figure 5-1: Phase diagram for the superfluid-Mott insulator diagram. The phase diagram is calculated using Eq. (5.8). As the ratio of J/U decreases, the system undergoes a phase transition to a MI phase with fixed integer filling. If the chemical potential μ is increased the filling factor n also increases.

a point where the addition of one atom to they system costs no energy; the kinetic energy gained balances the interaction energy. If an atom is added to the system it can tunnel freely, and thus will immediately condense into the superfluid state. If we instead increase J, and approach the tip of the MI state, we reach a point where the ground state changes to a superfluid to minimize energy. Contours of constant onsite number density surround the MI lobes.

Taking the derivative of Eq. (5.8), the critical value for the phase transition can also be found. For a 3D lattice

$$\left(\frac{J}{U}\right)_c = \frac{1}{6}\left(1 + 2n - 2\sqrt{n^2+n}\right). \tag{5.10}$$

In Table 5.1 the critical values are given for filling factors of $n = 1$ to $n = 5$. Although J/E_{rec} is independent of the wavelength of light used, U is proportional to a_s/λ_L, in table 5.1, the values are given for ^{87}Rb and $\lambda_{latt} = 1064$nm.

n	$\left(\frac{J}{U}\right)_c$	U_{latt}
1	0.0286	$14.5E_{rec}$
2	0.0168	$16.5E_{rec}$
3	0.0120	$17.5E_{rec}$
4	0.0093	$18.5E_{rec}$
5	0.0076	$19.5E_{rec}$

Table 5.1: Critical values for $\left(\frac{J}{U}\right)_c$ with different filling factors. The values are calculated using Eq. (5.10). The critical lattice depth U_{latt} is given for λ_{latt} =1064nm.

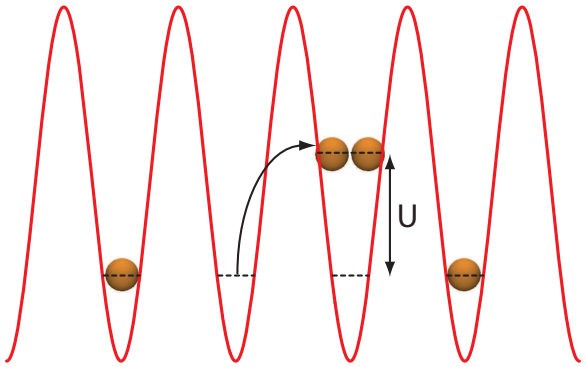

Figure 5-2: Excitations in the MI phase. The first excitation in the Mott insulating phase occurs when an atom tunnels into an adjacent cell, creating a particle hole excitation. The energy of the excitation is given by U, the onsite interaction.

5.3.3 Excitation Spectrum

After the critical lattice depth is reached, another distinctive feature of the MI phase is the excitation spectrum. In the superfluid phase, the excitation spectrum is continuous, and takes the Bogolibov form, (see Eq. (1.26)). Whereas in the MI phase a gap appears in the excitation spectrum. As illustrated in Fig. 5-2, the first excited state for the MI phase occurs when an atom tunnels into an adjacent site, creating a particle-hole excitation. For a MI with n atoms per site, one site has $n+1$ atoms, and one site is left with $n-1$ atoms. The energy of the system increases due to the repulsive onsite interaction, and this increase in energy, due the creation of the particle-hole excitation, is given by the onsite interaction between the atoms, U.

5.3.4 Effect of the External Confinement

In calculating the phase diagram above, the external confinement was set to a constant value. This would be correct if the experiments were performed in a box potential. In such a potential, there is only one MI phase with integer filling factor n. If an additional atom is added to the system the atom is able to tunnel freely, in a box potential the addition of a single extra atom is enough to destroy the MI state. Therefore, the realization of a MI phase in this configuration would be extremely difficult.

In real experiments with cold atoms, the atoms are of course held in an external harmonic trap. The effect of the external trap, and the initial density distribution of the condensate is to instead create a shell structure. Near the edges of the trap there is a $n = 1$ MI phase and as you move towards the center of the trap the occupation number increases. As shown in Fig. 5-3, if we again take a look at the phase diagram for the superfluid-MI transition, instead of sampling a point of this diagram we instead sample a line. To find the occupation number for a given lattice site we can define a local chemical potential which is equal to the chemical potential of the atoms minus the energy offset at a given site [22]. As shown on the phase diagram, as one moves towards the center of the trap, there are shells of increasing occupancy n, separated by small regions of superfluidity between each MI phase. In Fig. 5-3(c) the density distribution for a 2D slice shows this "wedding cake" structure of the MI phase.

The filling factor in a given lattice site i, can be found after defining the local chemical potential, $\mu_i = \mu - \epsilon_i$ in the lattice. The global chemical potential is given by [89, 83, 42]

$$\mu = \left(\frac{15}{16} \frac{(\lambda/2)^3 m^{3/2} N U \omega_{trap}^3}{\sqrt{2}\pi} \right)^{2/5}, \tag{5.11}$$

As shown in Fig. 5-1, the boundary between a n and $n + 1$ MI phase occurs when $\mu_i/U = n$. For a given external potential $U_{ext}(r_i)$, the radius and width of the MI phases can also be calculated.

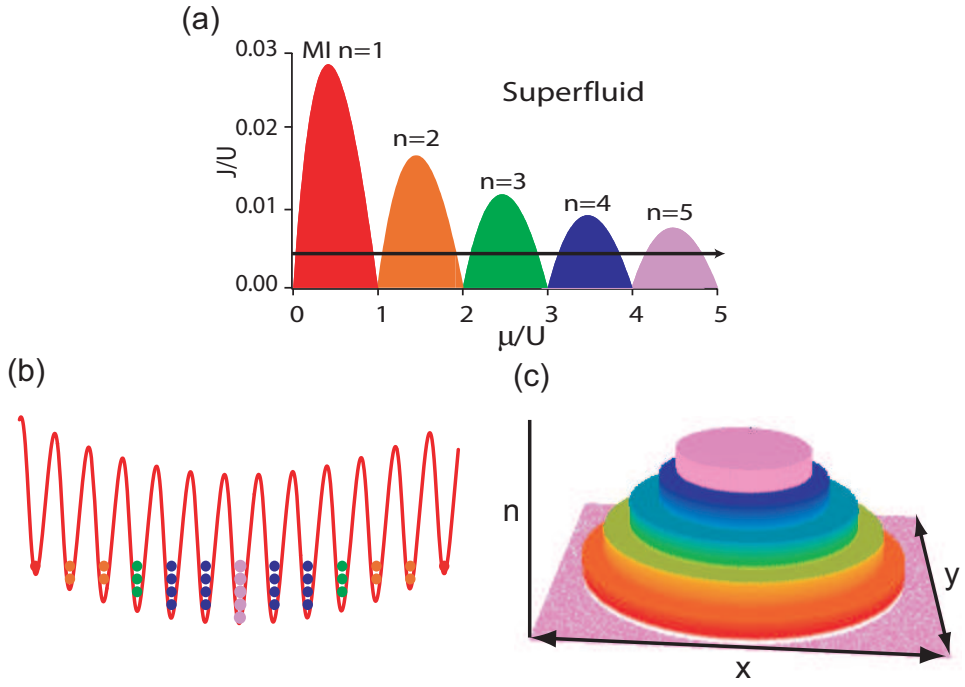

Figure 5-3: Effect of the external confinement on the Mott insulator transition. The external confinement of the trap and the initial density distribution of the condensate lead to a shell like structure, where near the edges of the trap there is a $n = 1$ MI and the occupation number increases as you move towards the center of the trap. (a) On the superfluid-MI phase diagram, instead of sampling a point on the diagram we sample a line. The phase diagram predicts shells of MI phase separated by small regions of superfluid in between each lobe. (b)A cartoon of a 1D slice through the lattice shows the resulting shell structure of the MI phase. (c) The density distribution for a 2D slice through the MI phase is shown.

5.4 Studying Condensed Matter Physics with Ultracold Atoms

The Mott Insulator transition was originally used to describe how electron correlations can lead to insulating behavior even for partially filled conduction bands, not to describe the behavior of neutral atoms. The superfluid-MI transition is just one example of how Hamiltonians (here the Bose-Hubbard model) which have been developed to describe condensed matter systems could be studied using ultracold atoms.

Using ultracold atoms to study model Hamiltonians offers a number of advantageous over typical condensed matter experiments. Ultracold atoms allow for a full range of control over the Hamiltonians. Using the Bose-Hubbard model as an example, we can vary J by tuning the depth of the lattice, or by changing the lattice spacing. U can be varied in similar ways, or by tuning the interaction using either magnetic or optical Feshbach resonances [52, 9, 113], and in addition the dimensionality of the system can be varied from $0D$ to $3D$ by varying the number of lattice beams used. Ultracold atoms also offer easy measurement techniques, one can either take pictures of the atoms in trap to see the spatial distribution, or in time of flight to see the momentum distribution. In addition, optical lattices are defect free and are well isolated from the environment, leading to long coherence times. One difference between ultracold atom realizations of model Hamiltonians, and condensed matter systems is the external potential (the third term in Eq. (5.3)). However, as was discussed above, this can even be advantageous for realizing the Mott insulating phase. A number of model Hamiltonians can be studied by using multiple atomic species or internal states, or by varying the lattice geometry[59, 8]. In recent experiments, in addition to the superfluid-MI transition [43, 107], the Tonks-Giradeau regime has been explored by trapping ultracold atoms in tight 2D optical lattices [39, 87, 67, 114]. The transition to a Bose glass phase was also recently demonstrated [29]. In addition to bosons, a number of groups are also pursuing experiments with ultracold fermions loaded into optical lattices [16, 68], and superfluidity of ultracold fermions loaded into optical lattices was recently demonstrated [16].

Chapter 6

Imaging the Mott Insulator Transition using Microwave Spectroscopy

This chapter describes experiments performed with condensates loaded into three-dimensional optical lattices, and supplements work previously reported in Ref [12], which is also included in Appendix C

6.1 Investigating the Superfluid to Mott Insulator Transition

A number of different diagnostics have been used to characterize the superfluid to Mott insulating (MI) phase transition with ultracold atoms. As discussed in chapter 5, the MI phase is characterized by perfect number states. In our experiments the lattice spacing, $\lambda/2 \approx 0.5$ μm, is much less than our imaging resolution, since individual lattice sites can not be resolved, it is easier to characterize the loss of phase coherence as the system undergoes the phase transition. For low lattice depths, in the superfluid phase, when the atoms are released from the trap and imaged after time of flight, one sees the familiar interference pattern, the atoms are still phase coherent across

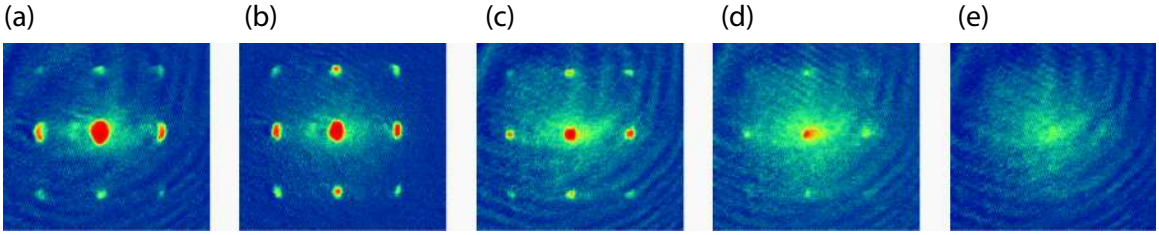

Figure 6-1: Superfluid to MI transition. Absorption images taken during the lattice rampup at lattice depths of: (a) 5 E_{rec}, (b) 9 E_{rec}, (c) 12 E_{rec}, (d) 15 E_{rec}, and (e) 20 E_{rec}. As the system undergoes the phase transition the interference fringes disappear. The images were taken after 41 ms time-of-flight

the lattice. As the lattice depth is increased number fluctuations are suppressed, and phase coherence between the lattice sites is lost. In time of flight, as shown in Fig. 6-1, as one enters the MI phase the interference peaks disappear.

The easiest diagnostic of the superfluid to MI transition is the loss of phase coherence as the lattice is ramped through the MI transition, and the restoration of phase coherence as the lattice is ramped back down to the superfluid phase. However, this loss of phase coherence does not conclusively prove a Mott insulating state as other processes such as quantum depletion [123], or collisions during the time of flight expansion can also lead to similar effects. A further diagnostic must therefore be performed. Previously, groups have measured the gap in the excitation spectrum in the insulating state by either tilting the lattice potential using a magnetic gradient [43] or by using Bragg spectroscopy [108]. In addition, to characterize the MI phase, the Mainz group recently used noise correlations to find correlations in the momentum distribution of the cloud [33]. Although these diagnostics can be used to show a Mott insulating state exists, they are not able to distinguish between sites with different filling factor, and could not resolve the shell structure of the Mott insulating phase in cold atoms. Recently, spin changing collisions [35, 34] in sites with $n = 2$ were selectively addressed, however this method would be difficult to use for higher occupation numbers. In this chapter, two-photon microwave spectroscopy, and in particular the cold-collision "clock" shift is used to spectroscopically resolve, and directly image the shell structure of the MI phase in ultracold atoms.

6.2 Clock Shifts in Magnetically Trapped Condensates

For the past 50 years, the definition of the second has been based on microwave transitions between hyperfine levels in Cesium atomic clocks. The accuracy of these clocks is limited by cold collision shifts [31, 104], because of their importance in atomic clocks, this shift is commonly referred to as the "clock" shift [38]. The clock shift originates from the interaction between atoms in the initial and final hyperfine states. Given an initial state $|A\rangle$ and a final state $|B\rangle$, as described in previous chapters, the interaction is provided by s-wave collisions within the condensate. If the scattering length for the final state differs from the scattering length for the initial state, then atoms in the final state have a different mean field energy. This leads to a shift in the resonance frequency, and the resulting clock shift is given by [48]:

$$\Delta\nu_{AB} = \frac{\hbar}{m}\left(a_{AB}\rho_A + a_{BB}\rho_B - a_{AA}\rho_A - a_{AB}\rho_B\right), \quad [1] \tag{6.1}$$

where m is the atomic mass, a_{AB} is the scattering length between an atom in state $|A\rangle$ and an atom in state $|B\rangle$, and ρ_A is the density of atoms in state $|A\rangle$. In addition to the clock shift, the resonance frequency can also be shifted by the differential Zeeman shift between the two hyperfine levels. For ^{87}Rb, if one uses the states $|1,-1\rangle$ and $|2,1\rangle$ for the initial and final states, at a magnetic bias field of $B_0 \sim 3.23$G the states have the same first order Zeeman shift [48].

6.2.1 Two-Photon Microwave Spectroscopy

The bare transition frequency between the $|1,-1\rangle$ and $|2,1\rangle$ state is $\nu_0 = 6.834\ 682\ 610\ 904\ 29(9)$ GHz [7]. To transfer atoms between the two states a two-photon pulse is used with one microwave pulse at ~ 6.83 GHz and one RF pulse at ~ 1.6 MHz. To find the resonance, the frequency of the RF photon is varied. If only a small fraction

[1] This equation is only true for a coherent mixture, for an incoherent mixture the shift is a factor of two larger.

of atoms are transferred to the final state, then Eq. (6.1) can be simplified to

$$\Delta\nu_{12} = \frac{h}{\pi m}\rho(a_{12} - a_{11}), \tag{6.2}$$

where for ^{87}Rb, the a_{21} and a_{11} scattering lengths are 5.19 nm and 5.32 nm, respectively [117].

When two-photon spectroscopy is performed on a magnetically trapped condensate (at a bias field of 3.23G), in addition to the mean field shift, the resonance is also broadened due to the inhomogeneous density distribution of the condensate. The broadened line shape is given by [106]

$$I(\nu) = \frac{15h(\nu - \nu_0)}{4\rho_0\Delta E}\sqrt{1 - \frac{h(\nu - \nu_0)}{\rho_0\Delta E}}, \tag{6.3}$$

where the mean field energy difference is

$$\Delta E = \frac{h^2}{\pi m}\left(a_{21} - a_{11}\right), \tag{6.4}$$

and ρ_0 is the peak condensate density. This line shape is asymmetric with the center of the line shape at $\nu = \nu_0 + 2\rho_0\Delta E/3h$, and the average frequency at $\nu = \nu_0 + 4\rho_0\Delta E/7h$.

In our experiments, another broadening mechanism was the Fourier width of the two-photon pulse. For a square pulse of length τ, the line shape is given by a sinc function

$$I(\nu) = \left(\frac{\sin(\pi\nu\tau)}{\pi\nu}\right)^2. \tag{6.5}$$

This washes out the asymmetry of Eq. (6.3) and broadens the line further, although the resulting lineshape is a convolution of the above two lineshapes, for our experiments we typically fit the spectra using a symmetric gaussian fit.

In Fig. 6-2(a), spectra are shown for a magnetically trapped condensate at two different densities. As the density of the condensate is increased, as expected, the line is both shifted and broadened. Gaussian fits of the spectra are shown, as well as the calculated lineshape. In Fig. 6-2(b), the center of the line is shown for increasing

density, and in Fig. 6-2(c), the width is shown.

6.2.2 Clock Shifts in Optical Lattices

When the condensate is instead loaded into an optical lattice the density increases as given in Eq. (5.11). If the two-photon resonance is measured for condensates held in a combination of a magnetic and optical lattice trap, then as the lattice depth is increased in the superfluid phase, the line should be shifted and broadened due to the increased density of the condensate. In the MI phase, the spectra will change considerably. For an $n = 1$ MI phase, since there is only one atom per site, there is no onsite interaction, and there will not be a clock shift to the resonance frequency. In addition, the line will no longer be broadened. For MI phases with $n > 1$, the onsite interaction increases by U for each atom > 1, and the resonance frequency will be shifted, but not broadened. The separation in the resonance frequency for the n and $n - 1$ MI phase is given by

$$\delta\nu = \frac{U}{h}\left(a_{21} - a_{11}\right)/a_{11}. \tag{6.6}$$

As the lattice depth is increased from $0E_{rec}$, the line should first be shifted and broadened due to the increased density until the MI phase transition, when discrete peaks should appear corresponding to MI phases with different filling factors.

6.3 Experimental Setup

In previous chapters, the condensate was initially created in a Ioffe-Pritchard magnetic trap, and then the lattice potential was either ramped or pulsed on. To prevent 3-body losses during the lattice ramp it is beneficial to start with low density in the initial condensate. This can be accomplished by either lowering the atom number, or by decreasing the initial trapping frequencies. In order to maintain good signal to noise in the data lowering the initial trap frequencies is the better of these two options. Due to technical limitations in our magnetic trap it was difficult to lower the

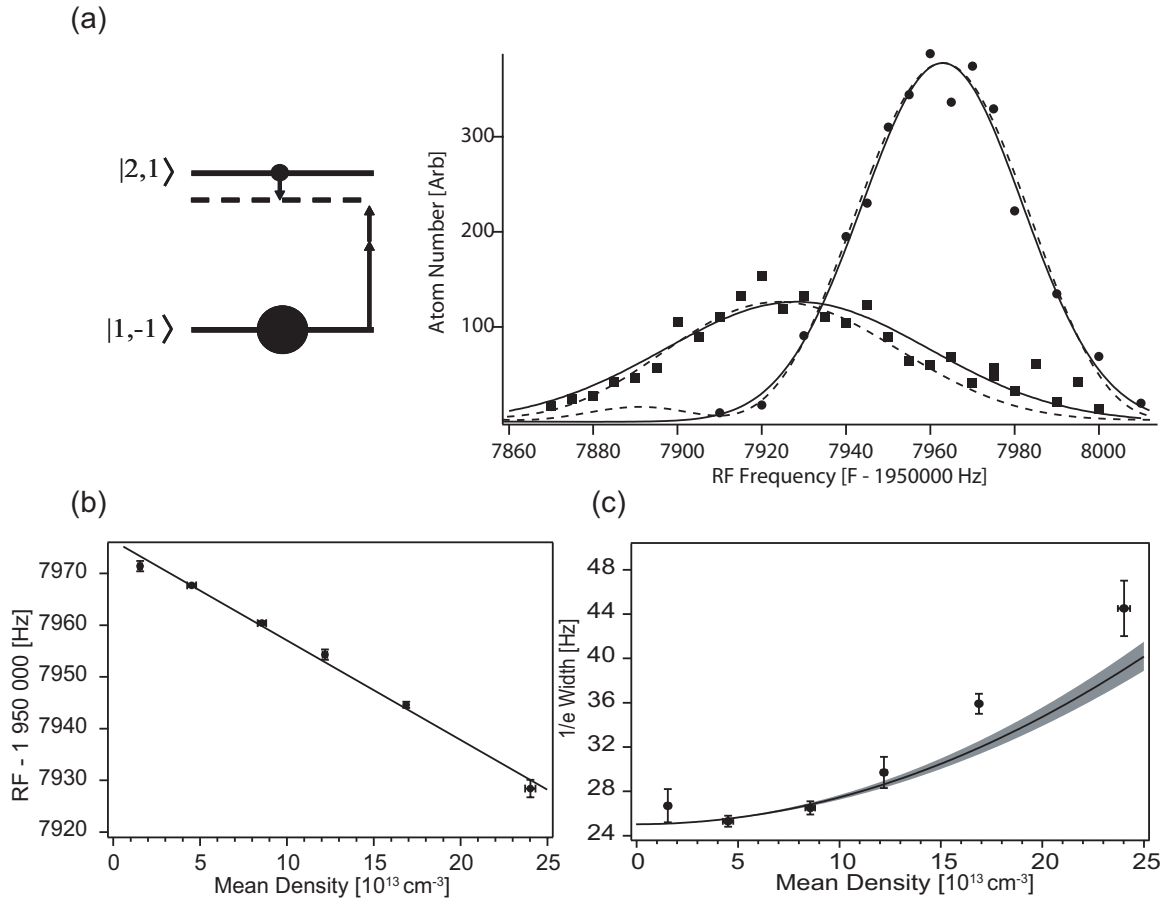

Figure 6-2: Two-photon spectrum of a magnetically trapped condensate. (a) Atoms in a magnetically trapped condensate are transferred from the $|1,-1\rangle$ to the $|2,1\rangle$ state using one microwave photon at ≈ 6.8 GHz and one RF photon at ≈ 1.6 Mhz. The a_{11} and a_{21} scattering lengths differ by a few percent, leading to a density-dependent "clock" shift of the resonance frequency. The resonance is shown for mean condensate densities of 9 $\times 10^{13}$cm^{-3} (circles) and 24 $\times 10^{13}$cm^{-3} (squares), using a 20ms two-photon pulse length. As the density of the condensate is increased the resonance is shifted and broadened due to the inhomogeneous density distribution of the condensate. The solid line shows a gaussian fit to the data, the dotted line shows the calculated lineshape using a convolution of Eq. 6.3 and Eq. 6.5. The spectra were taken at a magnetic bias field of $\sim$3.2 Gauss. (b) Transition frequency and (c) width of two-photon resonance as a function of the mean condensate density. The solid lines in (b) gives a fit to the data. The slope of the line gives a clock shift of $1.9(1)\times 10^{-13}$ Hz/cm^{-3}. The solid line in (c) shows the calculated width of the resonance, calculated using the clock shift found from (b). For low densities, the linewidth is limited by the Fourier width of the pulse, which for a 20ms pulse is $\approx$ 25Hz.

aspect ratio between the radial ω_{rad} and axial ω_{ax} trap frequencies in the magnetic trap to < 10. This meant that when the radial trap frequency was decreased to $\omega_{rad} \approx 20$Hz in order to decrease the density of the initial condensate, the axial trap frequency decreased to < 2Hz. With trap frequencies this low it is extremely difficult to ramp up the lattice potential adiabatically without causing excitations.

In order to create a low density condensate which did not have these limitations we instead used a combined magnetic and optical trap. The magnetic trap frequencies were first lowered as much as possible, and then an optical dipole trap was added perpendicular to weak axis of the magnetic trap increasing the axial trap frequency ω_{ax}. The optical trap was created using a retroreflected laser beam, however the polarization of the retroreflected beam was initially rotated to minimize the interference between the two beams. The polarization was later rotated to create a lattice beam using a liquid crystal waveplate. The intensity in the dipole trap was set such that when the waveplate was rotated to maximize the interference, the desired lattice depth, V_{latt} was reached. RF evaporation was used to create condensates in the combined magnetic and optical trap, however if the optical potential was to deep initially, the evaporation became less efficient and we were not able to produce condensates. This placed an upper limit on the lattice depths which could be achieved in the experiments. Typically, condensates with $N > 1 \times 10^6$ in the $|1, -1\rangle$ state were created, with shot to shot number fluctuations of $< 10\%$. To decrease the density further, a fast RF sweep through the RF resonance was used to decrease the atom number to $N \approx 1 \times 10^5$. The sweep was 5 ms long and ramped from 1.5 MHz to 3.00 MHz. The RF power was varied from 50 to 150mVpp depending on the desired final atom number. The trap bottom was at ≈ 2.35MHz, and varied by $\pm$ 0.05MHz from day to day.

A 3D optical lattice was then adiabatically ramped onto the condensate. As shown in Fig. 6-3, the lattice was created using three perpendicular, retroreflected laser beams. To prevent interference between the three separate lattice beams, the frequency of each beam was shifted by $\delta\nu \gg \Gamma_{las}$, where Γ_{las} is the linewidth of the lattice laser. The polarization of each beam was set to be perpendicular to the other

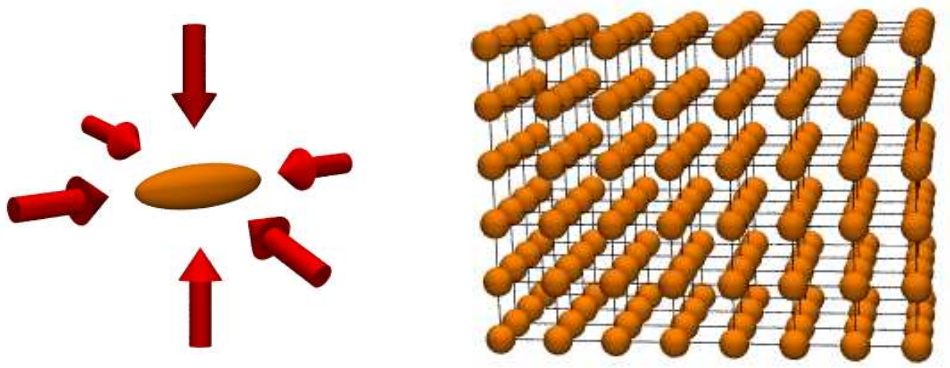

Figure 6-3: Three-dimensional optical lattice. The optical lattice was created with three retro-reflected laser beams using far off resonant light at $\lambda = 1064$ nm. The three beams were perpendicular creating a cubic lattice.

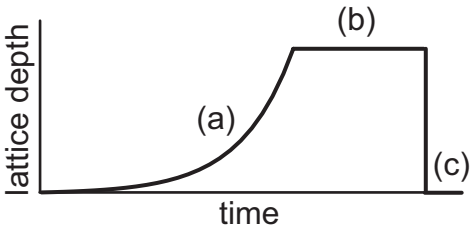

Figure 6-4: Lattice experimental setup. (a) The lattice was adiabatically ramped up by increasing the intensity in two of the beams, and increasing the contrast in the third direction. An exponential ramp with a 40 ms time constant was used. (b) While holding in the lattice a 100 ms two-photon pulse was applied to the atoms, which if on resonance transferred a small fraction of atoms to the $|2,1\rangle$ state. (c) The atoms were then released from the trap, and atoms transferred to $|2,1\rangle$ state were imaged after a 3 ms time of flight.

lattice beams. One of the lattice beams was created using the initial optical dipole trap, the lattice was ramped on adiabatically by rotating the polarization of this beam, while increasing the intensity in the other two lattice beams. An exponential ramp was used with a 40 ms time constant, where for a final lattice depth of 35 E_{rec}, the ramp up time was 200 ms. During the lattice ramp, an RF knife was kept on to remove any atoms from the trap which were heated during the ramp. As shown in Fig. 6-4, after ramping on the lattice, a 100 ms two-photon pulse was applied. If the pulse was on resonance a small fraction of the atoms were transferred to the $|2,1\rangle$ state. The RF power was set such that on resonance, less then 20% of the atoms were transferred to the final state. Immediately after applying the pulse the atoms were

released from the trap and were imaged using light resonant with the $F = 2 \rightarrow F' = 3$ transition. The atoms were typically imaged in 3 ms time of flight to decrease their column density. To image the spatial distribution the atoms were imaged in-situ.

6.4 Two-Photon Spectroscopy of the Superfluid to MI Transition

In Fig. 6-5, two-photon spectra are shown as the lattice depth is increased. The spectra were taken with a 100 ms pulse length, giving a Fourier limited linewidth of $\approx$ 5 Hz. The width of the spectra are shown in Fig. 6-6. At $0E_{rec}$, in only the combined magnetic and optical trap with no lattice, the linewidth of the spectra was 8.3(6) Hz, a convolution of the mean-field broadened lineshape and the Fourier width of the two-photon pulse. As the lattice depth was increased to $5E_{rec}$ the center of the line was shifted and the width broadened to 13(1) Hz due to the increased density of the condensate. At $10E_{rec}$, the line was shifted and broadened further, and in addition became asymmetric as the atom number in lattice sites with small occupation number became squeezed. Fitting the spectra as a double gaussian, the narrower peak originating from number squeezed sites had a linewidth of only 7.5(9) Hz, reflecting the lower number variance, whereas the width of the broader peak increased to 43(3)Hz. At 20 E_{rec}, discrete peaks appeared corresponding to the $n = 1$ and $n = 2$ MI phases, with a third broad peak corresponding to sites with larger occupation still in a superfluid phase. The width of the $n = 1$ MI peaks decreased to 5.0(.7)Hz, whereas the width of the broad superfluid was 18(2)Hz, a decrease from the $10E_{rec}$ width consistent with number squeezing in high occupancy sites. At $25E_{rec}$, discrete peaks corresponding to $n = 1$ to $n = 3$ were observed, with linewidths limited only by the bandwidth of the two-photon pulse, and no superfluid peak was observed. At 35 E_{rec}, peaks corresponding to $n = 4$ and 5 were also observed. Since there is no mean field shift, the center of the resonance frequency for the $n = 1$ peak should not shift as the lattice depth is increased however, as shown in Fig. 6-5, as the lattice

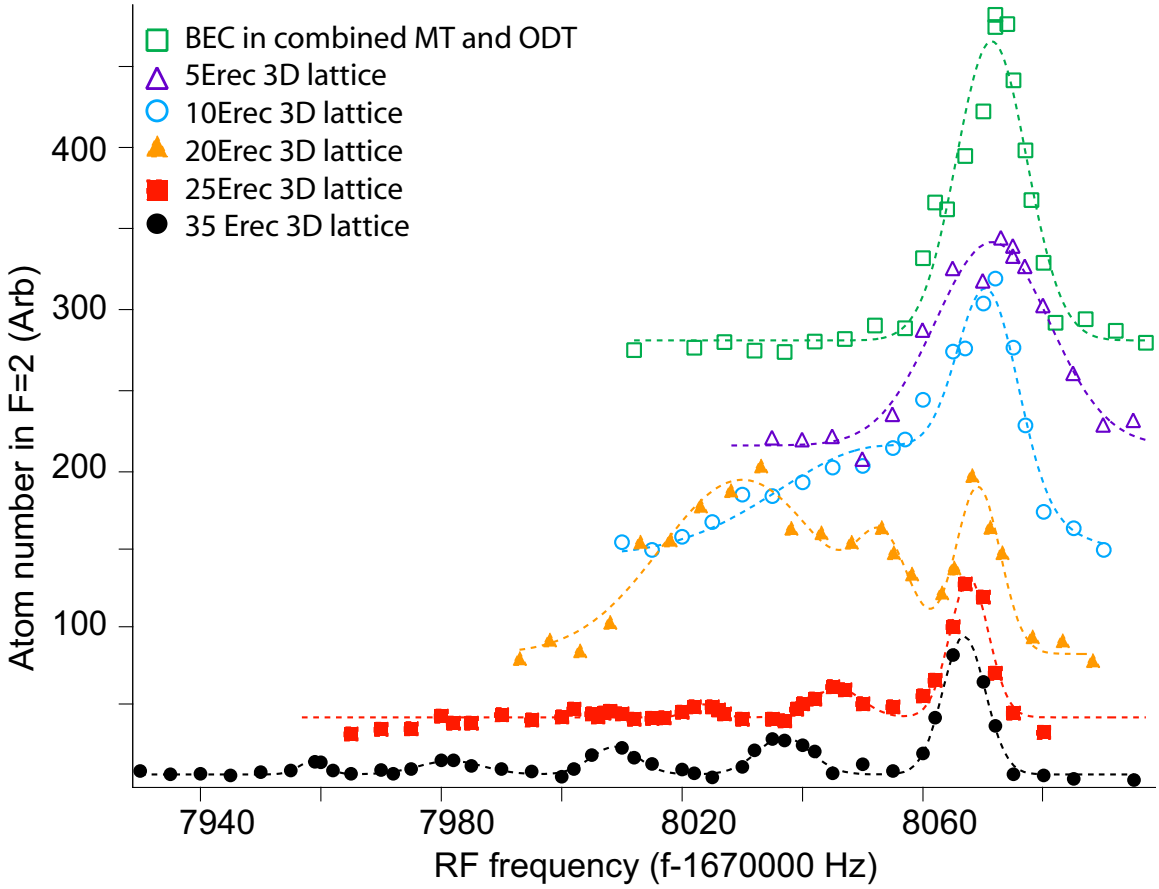

Figure 6-5: Two-photon spectroscopy of the superfluid to MI transition. Spectra for 3D lattice depths of $0E_{rec}$ (open squares), $5E_{rec}$(open triangles), $10E_{rec}$(open circle), $20E_{rec}$(solid triangles), $25E_{rec}$ (solid squares), and $35E_{rec}$(solid circles). The spectra are offset for clarity. The dashed line shows gaussian fits of the peaks. As the lattice depth is increased, the spectra are first broadened and shifted due to the increased density. After crossing the MI transition discrete peaks appear, corresponding to MI phase with integer filling n. The phase transition occurs at higher lattice depths for higher values of n. As the lattice depth is increased in the MI phase, the center of the $n = 1$ peak is shifted slightly due to the differential AC stark shift of the lattice.

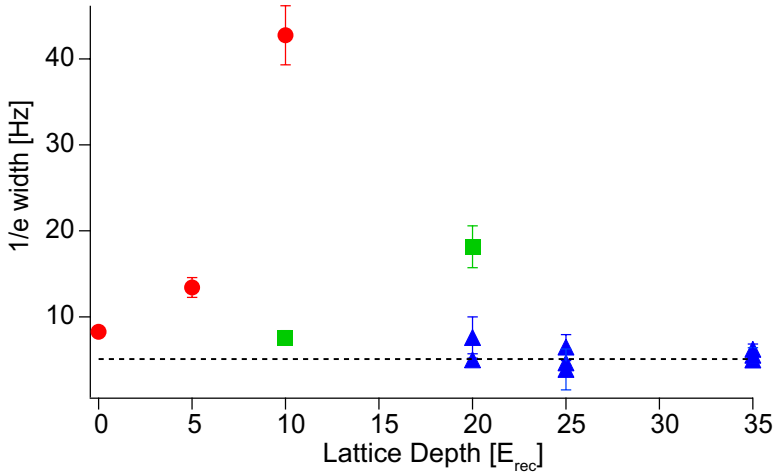

Figure 6-6: Change in the two-photon linewidth as the lattice depth is increased. The 1/e width of each peak in the spectra shown in Fig. 6-5 are plotted. As the lattice depth is increased from $0E_{rec}$, initially the width of the peaks increases (circles), due to the increased superfluid density. As the lattice depth is increased further the peaks start to narrow indicating number squeezing (squares), until finally in the MI phase, the width is only limited by the bandwidth of the two-photon pulse (triangles). The dashed line shows the bandwidth of the two-photon pulse.

depth was increased the center of the $n = 1$ peak shifted slightly to lower values[2], this shift was due to the differential AC stark shift due to the lattice potential. In addition, the center of the resonance could also be shifted by the admixture of particle-hole pairs within the $n = 1$ state [37, 36]. This effect scales with J/U, and should therefore decrease with increasing lattice depths.

The observation of discrete peaks is direct evidence for the suppression of tunneling by interactions when the MI transition is reached. The tunneling of atoms between sites of different occupation number during the microwave pulse would smear out the discrete peaks and eventually lead to peaks reflecting the clock shift at an averaged density. The characteristic energy associated with tunneling between sites is given by the width of the first Bloch band, $4J$. Therefore the tunneling time in a lattice site with n atoms, in the absence of interactions, is given by $h/4Jnz$, where z is the number of nearest neighbors (this can also be approximated using the double-well model). The tunneling rates for $n = 1$ to $n = 5$ are given in Table 6.1 A very deep lattice, where the tunneling rate was less than the length of the two-photon

[2]From 8069.1(4)Hz to 8066.8(1) Hz as the lattice depth was increased from 20 to $35E_{rec}$.

$U_{latt}[E_{rec}]$	$n = 1$ [ms]	$n = 2$	$n = 3$	$n = 4$	$n = 5$
5	0.20	0.10	0.07	0.05	0.04
15	2.1	1.0	0.7	0.5	0.4
20	5.3	2.7	1.8	1.3	1.1
25	12.8	6.4	4.2	3.2	2.5
35	60	30	20	15	12

Table 6.1: Tunneling times in the optical lattice as a function of n, the occupation number

pulse would still localize atoms even for a thermal or non-interacting gas. However as shown in Table 6.1, even at $35E_{rec}$, all of the tunneling times, and in particular the times for high occupation numbers, were shorter than the 100 ms two-photon pulse. With these short tunneling times if the system were not in a MI state, the resulting spectra would be distorted, blurring out the separation between the n and $n + 1$ peak. In addition, for our lattice depths no discrete spectrum were observed when the cloud was heated up during the lattice ramp by misalignment of the lattice beams. A sample spectra taken with a slight lattice misalignment is shown in Fig 6-7. All of our spectra were taken under conditions where the condensate fraction after ramping down the lattice was greater than 80%.

6.5 Imaging the Shell Structure

At 35 E_{rec}, the spectra for individual MI phases were well resolved. Therefore a given RF frequency was on resonance with at most one MI phase, and only atoms from an individual shell were transferred to the $F = 2$ state. By using resonant RF to transfer all of the atoms in a single MI phase to the $F = 2$ state, and by then imaging the atoms in trap, without time of flight, the spatial distribution of the MI phases could be directly imaged. In Fig. 6-8, in-situ absorption images which were taken at RF frequencies corresponding to the peaks in the two-photon spectra are shown. The absorption images are integrated along the line of sight, however they still clearly show the shell structure of the MI phase due the external confinement.

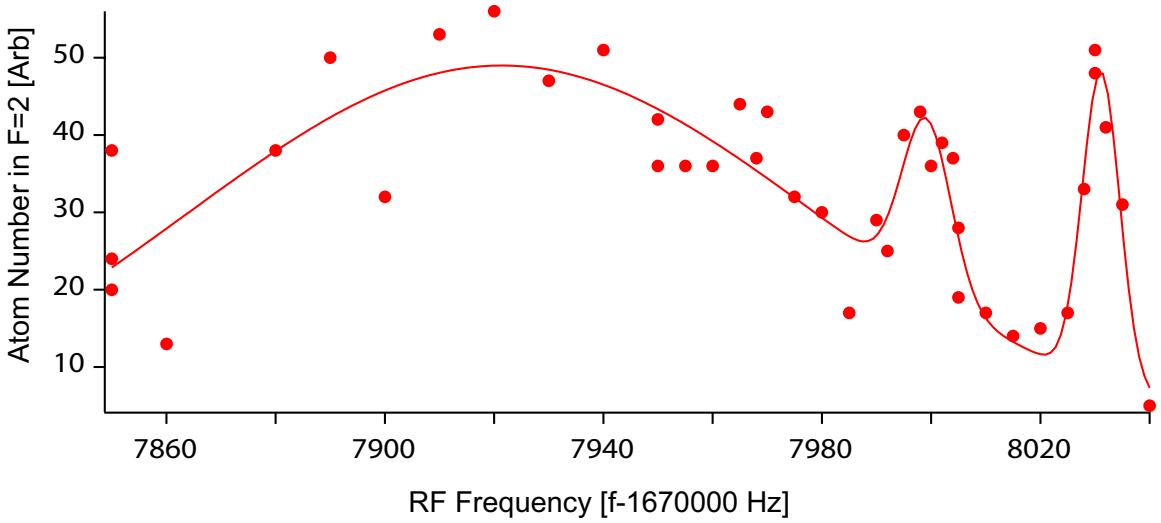

Figure 6-7: Effect of heating on the two-photon spectra. The spectra was taken using a lattice depth of 40 E_{rec}, the rest of the parameters were identical to the spectra shown in Fig.6-5. A slight misalignment of one of the lattice beams led to heating during the lattice ramp, blurring out the discrete peaks shown in Fig. 6-5.

The $n = 1$ phase is shown to originate from the edge of the trap and the radius of the shells decreases until $n = 5$ which originates from the center of the trap. In Fig.6-8, absorption images taken at RF values between the peaks are also shown. Although the signal is significantly less between the resonances a small fraction of atoms are still transferred to the $F = 2$ states. As discussed in Chapter 5, at non-zero values of J/U the phase diagram predicts shells of MI phase separated by regions of superfluid. Absorption images taken in between the resonances could be used to measure the fraction of atoms in these superfluid rings, however in order to study this the signal to noise must first be increased by either using a longer two-photon pulse, or by using deeper lattices to increase the separation between the MI resonances. The fraction of atoms in the superfluid rings could also be used to probe the temperature of the system [22].

In Fig. 6-8, the calculated radius for the MI shells is also shown, the value for the radius of the n^{th} MI phase was calculated using the condition $n - 1 < \left(\mu - \frac{m}{2}\omega_r^2 r^2\right)/U < n$. As discussed in the next section, the measured values of U extracted from the spectra were used to calculate the radius. With the exception of the $n = 1$ peak, the observed radii were in good agreement with the calculated values.

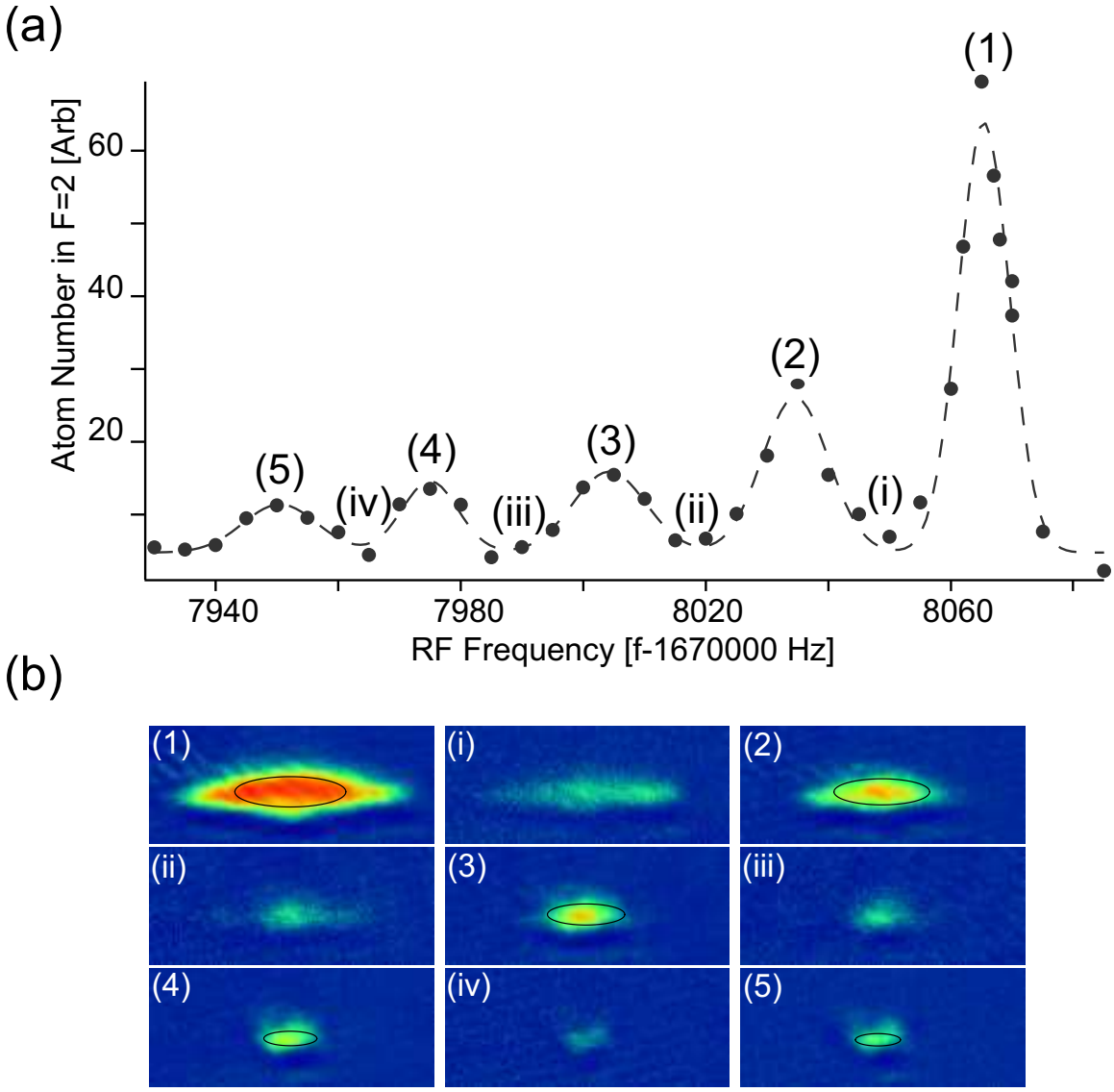

Figure 6-8: Imaging the shell structure. (a) Two-photon spectra at $35E_{rec}$. (b)Absorption images for decreasing RF frequencies. To image the spatial structure of the MI phase the absorption images were taken in trap with no time-of-flight. Images 1 to 5 show the shell structure for the $n = 1$ to 5 MI phase shown in (a). Images taken in between the peaks (i to iv) show a much smaller signal. With better resolution images in between the peaks could be used to determine the extent of the superfluid shells. The field of view was 185 μm by 80 μm

The disagreement with the $n = 1$ peak was most likely due to anharmonicities in the external trap caused by the overlap between the combined magnetic and optical dipole trap. This has since been remedied by increasing the waist of the initial optical dipole trap leading to a more spherical trap.

6.6 Onsite Interaction

As mentioned briefly in the previous section, we can also extract a measurement of U, the onsite interaction from the spectra. As shown in Fig. 6-9, as the lattice depth is increased within the MI phase, the separation between the n and $n + 1$ peaks increased. The separation between the peaks, as given in Eq. 6.6, is dependent on only the scattering lengths and the onsite interaction U. Therefore, the increase in the separation of the peaks as the lattice depth is increased gives us a direct measure of the onsite interaction. In Fig. 6-9(b), the separation between the $n = 1$ and $n = 2$ peak is compared to the calculated values using a band theory calculation. The uncertainty in the calculated values is due to the uncertainty in the a_{12} scattering length, and the uncertainty in the measured points is due to the uncertainty in the lattice calibration. Including these uncertainties, the measured values for the onsite interaction were in good agreement with the expected values.

From a close examination of the two spectra shown in Fig. 6-9, one may notice that although the separation between the $n = 1$,2, and 3 peaks seems to be approximately constant, the $n = 3$,4 and 5 peaks appear to be closer together. As shown in Fig. 6-9(c), if one plots out the separation between the peaks relative to the $n = 1$ peak, they are in fact closer. At $35E_{rec}$, the separation between the $n = 1$ and $n = 2$ peak is 30(1) Hz, whereas the separation between the $n = 4$ and $n = 5$ peak is only 22(2) Hz, a 25(7)% decrease from the expected onsite interaction! For deep lattices, the wavefunction on an individual lattice site can typically be approximated as the ground state of the harmonic oscillator, however this deviation shows that for high filling factors this is no longer a good approximation. As the filling factor in a given lattice site is increased, the repulsive interactions also increase, causing

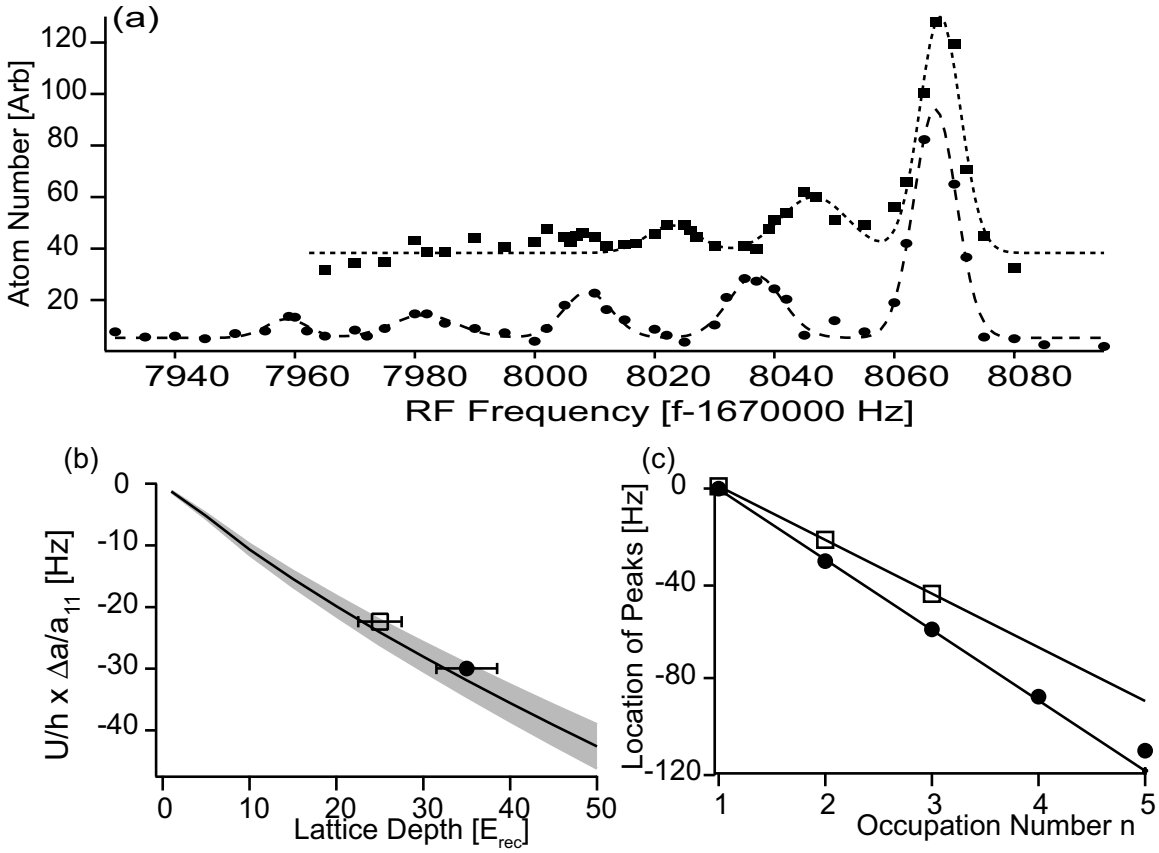

Figure 6-9: Measuring the onsite interaction. (a) Two-photon spectra for lattice depths of 25 E_{rec} (squares) and 35 E_{rec} (circles) as the lattice depth was increased. The separation between the n and $n+1$ resonance increased due to the increased onsite interaction, and the separation between the peaks gives a direct measurement of the onsite interaction. The spectra are offset for clarity. (b) The separation between the $n = 1$ and $n = 2$ peaks for the two spectra shown in (a) are plotted. The separation increased from 22(1)Hz to 30(1)Hz between 25 E_{rec} and 35 E_{rec}. The shaded line area gives the expected value for the onsite interaction including the uncertainty in the a_{11} and a_{12} scattering lengths. (b) The separation for the $n = 1$ to $n = 5$ resonances are shown relative to the position of the $n = 1$ peak. For low occupation numbers the separation was approximately constant, implying a constant U. However for higher occupation the peaks moved closer together showing a decrease in the onsite interaction for higher n. The line is a fit to the separation between the $n = 1$ and $n = 2$ peak.

the wavefunction to "bulge" out slightly, lowering the onsite interaction. Our spectra allow for both a measurement of the onsite interaction, and also allows us to infer how the wavefunction changes for higher filling factors. Using a variational calculation, similar to that shown in Chapter 1.4.1, one can find the change in the harmonic oscillator length due to the increased repulsive interactions. The variation calculation for $n = 5$ predicts a 7% increase in the harmonic oscillator length, leading to an 18% decrease in the onsite interaction, in agreement with our measured value.

6.7 Lifetime of the Shells

In the superfluid phase, the lifetime of the condensate is limited by 3-body recombination. As the lattice is ramped on, as was shown by the two-photon spectra, the condensate density increases dramatically. In order to decrease 3-body related heating during the lattice ramp up, the initial condensate density must be kept as low as possible. Once in the MI phase the lifetime is highly dependent on the filling factor in a given MI shell. By adding a hold time into the experimental sequence after ramping up the lattice, but before applying the two-photon pulse, the lifetime of individual MI phases could be measured.

In Fig. 6-10, two-photon spectra are shown for increasing hold times. For the $n = 1$ MI phase, since collisions cannot occur, (and ignoring technical noise) the lifetime of the atoms should be limited only by spontaneous scattering from the lattice. The spontaneous scattering rate from the lattice potential using Eq. (2.16)is only $\Gamma_{SC} \approx$ .005Hz for a 35 E_{rec} lattice. For the $n = 2$ MI phase 2-body processes are allowed, however for ^{87}Rb the dipolar relaxation rate is quite small, with $\Gamma_{DP} < 10^{-2}$Hz. For sites with $n >$3, 3-body recombination again becomes the limiting factor. For the MI phase the 3-body rate is given by $\Gamma_{3B} = \gamma n(n-1)(n-2)$[56]. For our parameters, $\gamma = \frac{K_3}{12}\int d\vec{r}|w_i(\vec{r})|^6 = 0.026$ Hz, where the Wannier function has been approximated as the ground state of the harmonic oscillator. Using this value, the scattering rate for the MI phases are $\Gamma_{3B} = 0.16$ Hz, 0.63 Hz and 1.58 Hz for the $n = 3$, 4 and 5 MI phase. If we adjust the rate of γ using our variational calculation for the harmonic

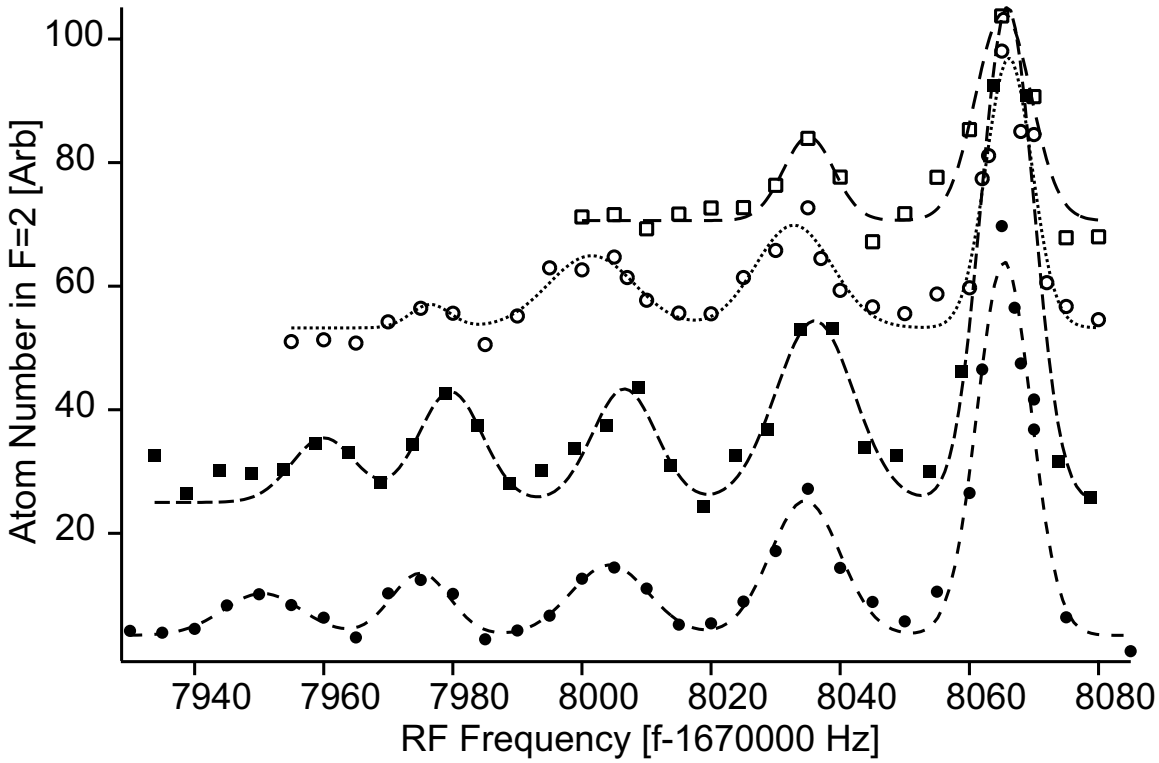

Figure 6-10: Lifetime of the shells. By adding a hold time before applying the two-photon pulse the lifetime of individual MI phases could be measured. Holds of 0 ms (solid circles), 100 ms (solid squares), 400 ms (open circles) and 2000 ms (open squares) are shown. The lattice depth was $35E_{rec}$ except for the 100 ms hold time for which it was $34E_{rec}$. The spectra were offset for clarity.

oscillator length for the $n = 5$ MI phase we find a rate of $\Gamma_{3B} = 1.05$ Hz. Our measured lifetimes derived from Fig 6-10, were $\tau \approx 1$s, 0.5s and 0.2s for the $n = 3$,4 and 5 MI phases. The disagreement between our measured lifetimes and the 3-body rate was most likely due to technical noise in the lattices. For $n = 1$ and 2 lifetimes of over 5 s were observed.

6.8 Lattice Design and Alignment

In the following section I describe the design of the optical lattice setup, and detail some of the technical difficulties that arose during the lattice experiments. The section is primarily meant as a resource for future lab members.

6.8.1 Lattice Setup

The lattice experiments were all preformed in the main "production chamber" where the optical access is severely limited by both MOT optics and by imaging optics. To couple the IR lattice light into these beam paths dichroic mirrors[3], which reflect 1064 nm light and transmit 780 nm light, were used for both the input of the lattice beam and for the retro reflection. Using dichroic mirrors is non-optimal for multiple reasons. For the lattice light (at 1064 nm), a few percent of the beam is transmitted instead of being reflected. For the mirrors before the chamber this has no effect, however for the retroreflected beam this means that the lattice contrast is not 100%. Reflections from the back surface of dichroic can also cause problems. For the 780 nm light <90% of the light is transmitted, leading to unbalanced MOT beams and also imaging problems. However, given our limited optical access the lattice beams had to be aligned on top of 780 nm beams.

The lattice laser was a 20W single frequency Ytterbium fiber laser, purchased from IPG Photonics, a single laser was used for all three lattice beams. The laser was split into three beam paths and then transferred from the optics table to the

[3]The mirrors used at 45° incidence were short wave pass dichroic beamsplitters, the 0°incidence mirrors were Nd:YAG mirrors which only reflected 1064 nm light and act as a window for 780 nm light.

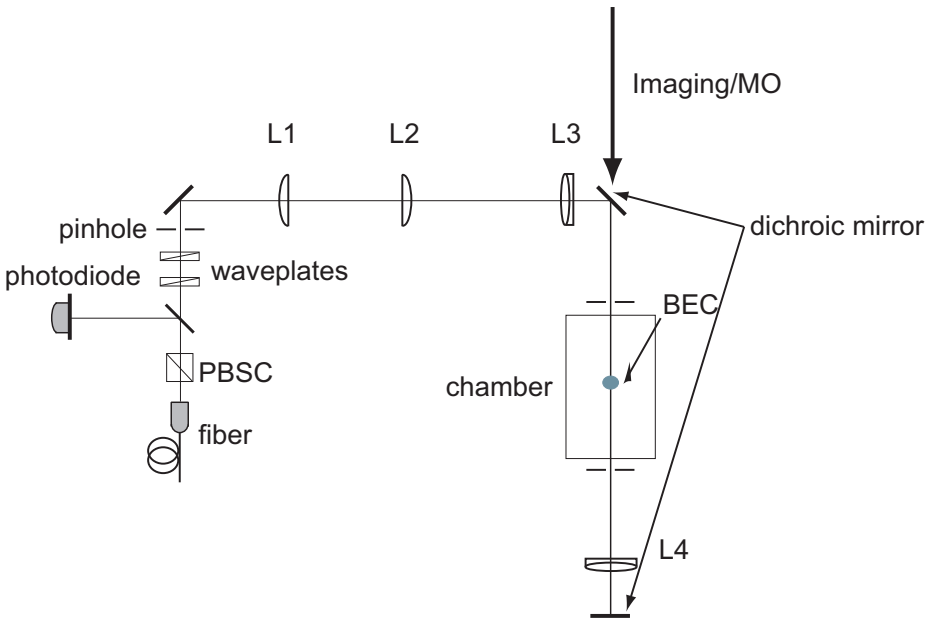

Figure 6-11: Lattice setup. The lattice light is brought to the table using a high power optical fiber (see text for description). Immediately after the fiber a polarizing beam splitting cube (PBSC) is used to clean up the polarization of the light. A pick-off window is then used to send a few percent of the light to a photodiode which is used to stabilize the intensity of the beam. After the pick off, both a $\lambda/4$ and a $\lambda/2$ waveplate are used to set the polarization of the beam. The beam is then expanded using a telescope, and is focused on the condensate using an achromatic lens. The beam is re-collimated after exiting the chamber and is then retro-reflected. Three irises are used to block back reflections from lenses and the vacuum chamber viewports.

experiment table using high power single mode optical fibers made from components also purchased from IPG Photonics. A detailed description of how to make and align light through these fibers is given in [124]. A generalized schematic and description for the lattice setup is shown in Fig. 6-11. The liquid crystal waveplate used to control the polarization of the optical dipole trap used in the combined magnetic and optical trap was purchased from Meadowlark optics (LRC-100 IR2 1" with attached compensator), and was placed immediately after the chamber before the final lens and mirror. The waveplate requires a 2 kHz square wave, and the retardation is determined by the amplitude of the square wave. The response time of the waveplate was between 10 - 50ms for a $\lambda/4$ rotation which was sufficient for our experiments[4].

[4]A $\lambda/4$ retardation rotates the beam by $\lambda/2$ since the beam is transmitted through the waveplate twice, once after exiting the chamber, and once after retroreflection before reentering the chamber.

The lattice lifetime and the quality of the Mott insulating state were highly sensitive to slight misalignments in the lattice beams. In the following section the alignment procedure for the lattice is detailed.

6.8.2 Lattice Alignment

To align the optical lattice, the BEC was first imaged along the lattice direction by transmitting imaging light through the lattice beam path. The dichroic mirror used for the retroreflection was removed to ensure that the imaging beam was not displaced relative to the lattice beam. The BEC was focused onto the imaging CCD camera (an additional lens was added just before the camera to focus the image) by moving the second achromatic lens (the lens used to re-collimate the lattice beam before the final mirror). The pixel position of the focused condensate was then marked on the camera, and the lattice beam was aligned and focused onto the same spot. To focus the lattice beam onto the camera the first achromatic lens was moved. To fine tune the alignment, the laser power was turned up to its maximum value ($\sim$3W), and a BEC was created in the combined magnetic and optical trap (with the initial beam, but no retro-reflected beam). The final lattice mirror before the chamber was then aligned such that the position of the BEC in the combined trap was identical to the position in just the magnetic trap. The position was checked along both directions perpendicular to the lattice. This process was repeated for all three lattice beams.

After aligning the initial beam, the retro-reflected beam was roughly aligned by reflecting the beam back onto itself, and then by maximizing the power coupled back through the fiber coupling onto the optics table. The alignment was then fine tuned using Kapitza-Dirac(KD) diffraction. To align the beam using KD, the lattice was pulsed on for 12.5 μs. The retro-reflecting mirror was then aligned to maximize the diffraction pattern. After alignment, the lattice depth was calibrated by measuring the population in each KD order as a function of the laser intensity as discussed in section 2.2.4.

6.8.3 Technical Issues

To ensure good stability and lifetime in the lattice there are a few essential points:

1. Proper alignment of the beams. Even slight misalignments of the lattice caused substantial center-of-mass oscillations when the lattice was ramped onto the condensate. Although this does not severely affect the lifetime in a 1D lattice, when a 3D lattice was ramped on these oscillations led to considerable heating of the cloud.

2. Back reflections. If back reflected beams were aligned onto the atoms this decreased the lifetime of the lattice significantly. The majority of viewports in our main "production" chamber are not IR coated, in particular, the "penny window" viewports which are parallel to the long axis of the magnetic trap reflect a non negligible amount of light.[5] To limit the effect of back reflections, as shown in Fig. 6-11 irises were placed as close as possible on either side of the chamber. An additional problem from back reflections was on the intensity stabilization. If back reflections were not blocked they formed an interference pattern on the photodiode used to stabilize the intensity of the beam (see Fig. 6-11). The feedback then stabilized the interference signal between the initial and retroreflected beam leading to intensity fluctuations on the atoms. These intensity fluctuations led to heating in the lattice and shortened lifetimes. To minimize this problem, if polished fibers are used, it is essential to use angle polished fibers to avoid near normal reflections off the face of the fiber.

3. Vibrations. Although the retro-reflected lattice is less sensitive to vibrations then the moving lattice described in chapter 4, we have still seen vibrations effect the lifetime of the lattice. In particular, our original CCD camera was air cooled and vibrations from the fan caused significant problems. Suspending the camera from the table increased the lattice lifetime for the retroreflected lattice by approximately a factor of 2, and for the moving lattice by more than an order of magnitude. We have since switched to a water cooled camera which seems to have alleviated these problems. However, due to our lack of optical access, all of our lattice beam paths are quite long. The longest being over 3 m, making vibration isolation difficult. For

[5] We once mistakenly aligned only the back reflection from the penny windows onto the condensate and saw considerable Kapitza-Dirac diffraction.

moving lattices vibrations pose an additional problem, since the lattice is sensitive to any element in the beam path vibrating, not just the retroreflection mirror.

4. Polarization. Besides back reflections, the "penny window" viewports are also birefringent. Because of this, the lattice in this direction is very sensitive to the polarization of the light. In order to maximize the contrast of the lattice, the polarization must be linear.

In the future, first transporting the atoms to an auxiliary chamber, with better optical access, coated windows, and with shorter beam paths allowing for better vibration isolation should make aligning and creating stable lattices a much easier task.

Chapter 7

Raman Amplification of Matter Waves

This chapter briefly introduces Raman superradiance, which was previously described in [99], and is also included in Appendix D

The first research that I made a major contribution to after arriving at MIT was the demonstration of a "Raman Amplifier" for matter waves. Since the majority of this thesis has been focused on the use of optical lattices to manipulate ultracold atoms, I only briefly introduce the experiment here, and refer the interested reader to appendix D for a more detailed description. The Raman superradiance project gives an excellent example as to how "mistakes" in the lab can sometimes lead to new physics.

7.1 Rayleigh Superradiance

I start this chapter with a very simple question, what happens when you illuminate a Bose-Einstein condensate with a single off resonant laser beam? Normally of course, you would expect to just see normal Rayleigh scattering, where an atom absorbs a photon and spontaneously emits a photon. The result is a dipolar emission pattern. However, as was shown in [54], if an elongated condensate is illuminated with an

off resonant laser beam, and if the beam is perpendicular to the long axis of the condensate, instead one sees highly direction scattering into discrete momentum states [Fig. 7-1(b)]. This phenomena of supperradiant scattering was first proposed by Dicke [26], where he showed that spontaneous emission from an ensemble of N localized atoms in a cooperative state is enhanced by a factor of N over the single atom emission rate.

To understand Rayleigh superradiance one can consider the grating formed by the recoiling and stationary atoms. Initially, when the laser beam is first incident on the condensate the first atom can scatter a photon in any direction. Once the atom has scattered a photon it will then recoil within the condensate due to the recoil velocity. The recoiling atoms are still in the ground state, therefore the recoiling atoms and those at rest can still interfere, creating a moving density grating, which can then diffract subsequent photons. This process is self-amplifying, since each diffracted photon creates a recoiling atom, which in turn increases the amplitude of the matter wave grating. If the condensate is elongated, the gain will be largest when the photons are scattered along into the long axis of the condensate, this is the so called "end-fire" mode. Alternatively, one can also think of the probe beam and end-fire mode as an intensity grating, or a moving optical lattice.

In early 2002, the first experiments performed on the newly built "Rubidium" machine at MIT were on Rayleigh superradiance in the short and long pulse regime [101]. In the short pulse (Kaptiza-Dirac) regime atoms were scattered both parallel and anti-parallel to the direction of the incoming beam, and in the long pulse (Bragg) regime only parallel to the beam.

7.2 Raman Superradiance

Rayleigh superradiance is highly depend on the polarization of the incident laser beam. In Rayleigh superradiance, the initial and final state of the atom are the same. The absorbed and emitted photons have the same polarization, and in order to see superradiance we must have emission into the end-fire mode. As shown in Fig. 7-1,

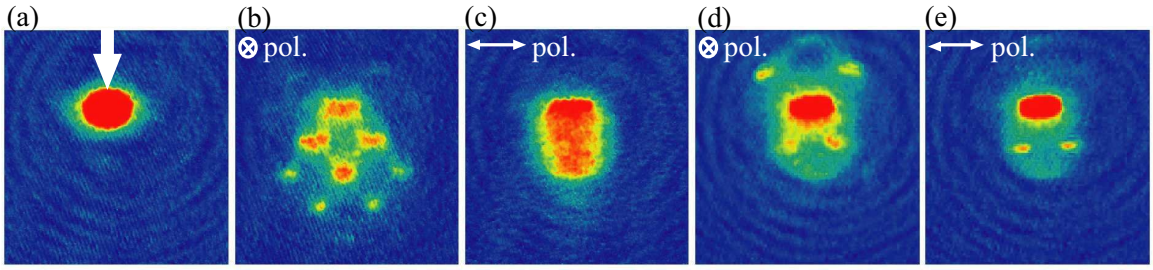

Figure 7-1: Transition from Rayleigh to Raman superradiance. (a) A elongated condensate is illuminated with a single pump beam. The condensate is then released from the trap and imaged after 30 ms time of flight. The field of view is 1.3 mm×1.4 mm. (b) When the pump beam was π-polarized with the electric-field vector **E** perpendicular to the long axis of the condensate supperradiant Rayleigh scattering was observed. (c) When the polarization of the beam was instead parallel to the long axis of the condensate the supperadiance was suppressed, and a "halo" pattern from normal rayleigh scattering was observed. In (b,c) the pulse length was 1 ms, with 40 μW of power. In (d,e) the pulse length was both shortened and the intensity increased by a factor of 100. (d) For **E** perpendicular to the long axis, self-stimulated Kapitza-Dirac scattering was observed. (e) For **E** parallel, superradiant Raman scattering was observed. The pump beam detuning was Δ = -340MHz for all of the images. The detuning is given relative to the $5^2S_{1/2}, F = 1 \rightarrow 5^2P_{3/2}, F = 1$ transition.

this requirement is fulfilled by using π-polarized light, where the polarization of the electric field vector **E** is perpendicular to the long axis of the condensate. However, if you rotate the polarization such that **E** is parallel to the long axis of the condensate then emission into the end-fire mode is suppressed. As shown in Fig. 7-1(c), instead of seeing superradiant scattering one instead sees the dipole emission pattern of normal rayleigh scattering.

One night in early 2002, while finishing up the Rayleigh superradiance experiment, a very strange signal was seen. Instead of a cascade of superradiant states, as seen in Fig. 7-1(b), the condensate was instead depleted into just one order. After checking a variety of parameters it was realized that the polarization of the beam wasn't quite right. The polarization was fixed, and the problem was solved. However, we always wondered what had caused those strange pictures. A year later we returned to the problem and decided to try to reproduce the pictures. The results are shown in 7-1(e). With **E** polarized parallel to the long axis of the condensate, where superradiance should be suppressed, instead when the pulse length was shortened and the intensity

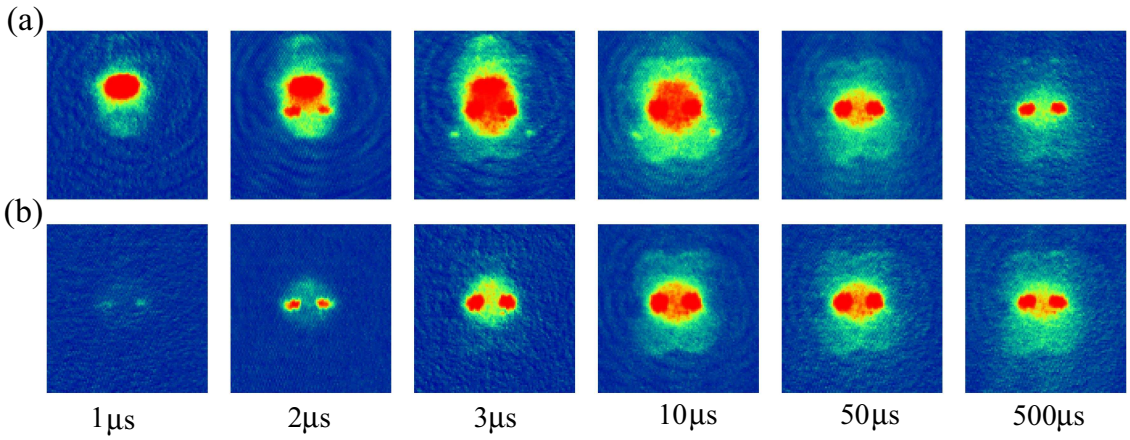

Figure 7-2: Time Evolution of Raman superradiance. Absorption images taken for increasing pulse length. The detuning of the beam was Δ = -340MHz. The pulse had 2.2mW of power. As the pulse length was increased the atoms were scattered into two discrete states. The initial condensate was in the $|1,-1\rangle$ state and the final peaks were in the $|2,-2\rangle$ state. In (a) Absorption images are taken after first repumping the F = 1 atoms into the F = 2 state and by then imaging with light resonant with the F = 2 state. (b) Absorption images of only the F = 2 atoms.

increased, supperadiant peaks appeared. But how could this be? In Fig. 7-3, a time evolution of the process is shown. When the power in the pulse was increased by a factor of 100 from those used in the Rayleigh supperradiance experiments, the scattering became highly directional again and two distinct peaks appeared into which the entire condensate was transferred. Unlike the normal cascade pattern seen in Rayleigh supperadience due to higher order scattering events, the atoms remained in these two peaks, even when the light was left on.

The condensates used in these experiments were initially created in the $|F = 1, m_F = -1\rangle$ state. Imaging the atoms using light only resonant with atoms in the $F = 2$ state, and applying a magnetic field gradient during the time of flight to perform a Stern-Gerlach separation, we discovered that the atoms in the two final peaks were no longer in the $|1,-1\rangle$ state. They had instead been transferred to the $|2,-2\rangle$ state, we had demonstrated Raman superradiance. The atoms absorbed a π-polarized photon from the laser beam, and emitted a σ-polarized photon into the end-fire mode. For the detuning of our probe beam, Δ = -340MHz, the $|2,-2\rangle$ state this was the most probable transition. Once the atoms had scattered a photon and were in the $|2,-2\rangle$

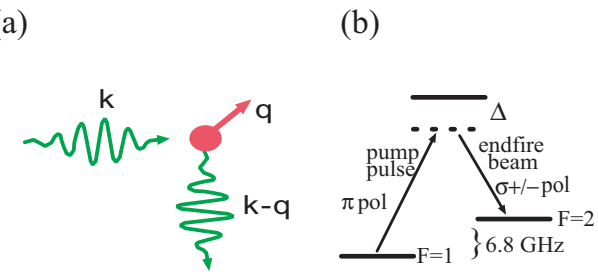

Figure 7-3: Experimental setup for raman superradiance(a) An atom absorbs a photon with momentum k. The atom then emits a photon with momentum $k - q$ into the end fire mode of the condensate, and recoils with momentum q. (b) The absorbed photon has π-polarization, and the emitted photon $\sigma\pm$-polarization leading to a Raman transition to a different hyperfine state. The final state was $\approx$ 6.8GHz detuned from the pump beam.

state, as shown in Fig. 7-3, they were 6.8 GHz out of resonance with the probe beam and no higher order scattering events could occur. By varying the detuning of the probe beam, the final states could also be varied. The fraction of atoms transferred to a given state could be calculated from the two-photon transition matrix for a given detuning. In Fig. 7-4, the results are shown for a detuning of Δ = -140 MHz, where atoms were scattered into $|1, 0\rangle$, $|1, -1\rangle$, as well as the $|2, -2\rangle$ state.

In addition, this process was used to demonstrate a matter wave amplifier where the initial and final states are different. It is really quite amazing the number of different phenomena which can be seen by simply shining a single laser beam onto a condensate. This project also showed how simple "mistakes", here a wrong polarization, can led to unexpected results.

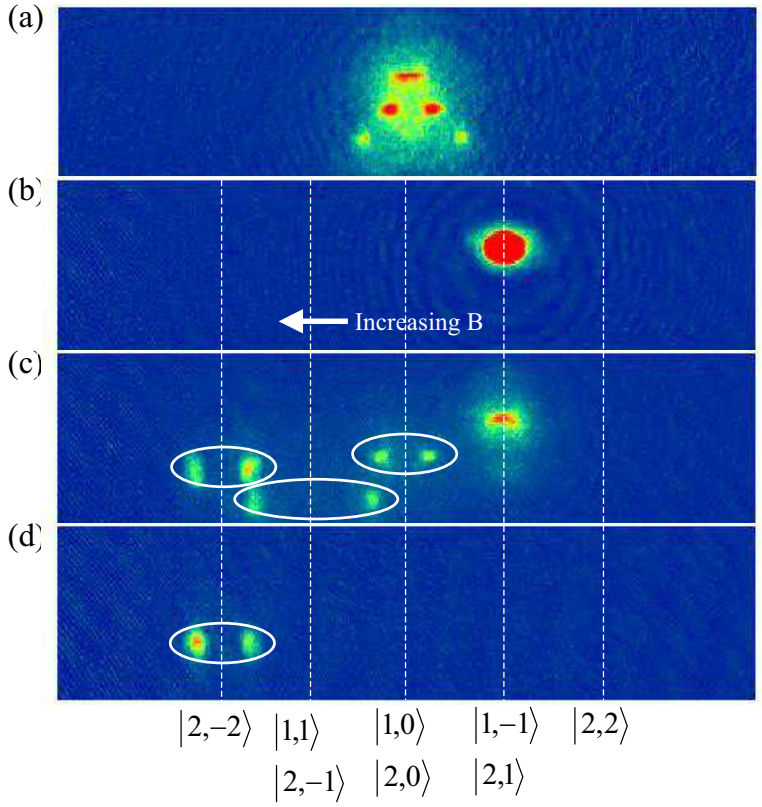

Figure 7-4: Hyperfine state identification of Raman supperradiance. (a) Absorption image showing superradiant Raman scattering. The pump beam had a detuning of Δ = -140MHz. The pulse was 5 μs, with 0.9 mW of power. (b-d) Absorption images taken using a magnetic field gradient to separate the hyperfine states. (b)The initial condensate in the $|1,-1\rangle$ hyperfine state. (c,d) After applying the laser pulse the atoms were scattered into two superradiant orders. (c) Absorption image showing both F=1 and F=2 atoms. (d) Absorption image showing only F=2 atoms. The first order peaks had atoms in the final states $|2,-2\rangle$ and $|1,0\rangle$. Atoms in the $|1,0\rangle$ state were still near-resonant with the pump beam and scattered atoms into the second order peak which was in state $|1,1\rangle$. The field of view was 4.6 mm $\times$ 0.2 mm

Chapter 8

Conclusion and Outlook

The unifying theme of this thesis has been the use of optical lattices to manipulate Bose-Einstein condensates. However, in each experiment the lattice has been used in very different ways and to study very different physics.

Precision Measurements and Atom Interferometry - A pulsed optical lattice was used to measure the photon recoil momentum in dispersive media. Not only did this answer a fundamental question about momentum in dielectric media, but it will also hopefully improve the accuracy of precision measurements made using ultracold atoms.

Nonlinear Atom Optics - A shallow one-dimensional optical lattice was used to modify the dispersion relation for the condensate in order to demonstrate the matter-wave analogue of both optical parametric generation and amplification of photons.

Strongly Interacting Systems - A deep three-dimensional optical lattice was used to demonstrate the superfluid-to-Mott insulator transition. Two photon microwave spectroscopy was then used to resolve and directly image the shell structure of the MI phase.

8.1 The Future of BEC IV

The superfluid to MI transition with ultracold atoms, is just one example of how ultracold atoms can be used to simulate more complicated condensed matter systems

([8], and references therein). As we start to study more complicated systems, the microwave spectroscopy detailed in this thesis should prove to be an excellent diagnostic. In future experiments with the MI transition one could precisely measure the number statistics as the system undergoes the phase transition. Although at low lattice depths the tunneling rate is still high, the lattice depth can be suddenly increased, freezing in the population [44], which can then be probed using high-resolution microwave spectroscopy. In addition, by applying a magnetic gradient across the lattice, tomographic slices could be selected, combining full 3D resolution with spectral resolution of the site occupancy.

The addressability of individual shells described here could be used to create systems with only selected occupation numbers (e.g., by removing atoms in other shells). Such a preparation could be important for the implementation of quantum gates, for which homogenous filling is desirable. The ability to address sites with unit occupancy can also be used to make improved precision measurements [28].

In the near future, our optical lattice experiments will move from being preformed in the main "production" chamber, to the auxiliary "science" chamber. The improved optical access and vibration isolation of the science chamber should lead to better stability and longer lifetimes in the optical lattice, and in general should make the experiments much easier to setup and perform. New lattice geometries, such as triangular lattices, spin-mixtures, and disordered potentials will all be possible to realize in the new science chamber, leading to almost endless possibilities. I am leaving the Rubidium lab in very capable hands, and look forward to hearing of their future successes, of which I'm sure there will be many.

Appendix A

Photon Recoil Momentum in Dispersive Media

This appendix contains a reprint of Ref. [63]: G.K. Campbell, A.E. Leanhardt, J.M. Mun, M. Boyd, E.W. Streed,W. Ketterle, and D.E. Pritchard, *Photon Recoil in Dispersive Media*, Phys. Rev. Lett. **94**, 170403 (2005).

Photon Recoil Momentum in Dispersive Media

Gretchen K. Campbell, Aaron E. Leanhardt,* Jongchul Mun, Micah Boyd, Erik W. Streed, Wolfgang Ketterle, and David E. Pritchard†

MIT-Harvard Center for Ultracold Atoms, Research Laboratory of Electronics and Department of Physics, Massachusetts Institute of Technology, Cambridge, Massachusetts 02139, USA

(Received 31 January 2005; published 4 May 2005)

A systematic shift of the photon recoil momentum due to the index of refraction of a dilute gas of atoms has been observed. The recoil frequency was determined with a two-pulse light grating interferometer using near-resonant laser light. The results show that the recoil momentum of atoms caused by the absorption of a photon is $n\hbar k$, where n is the index of refraction of the gas and k is the vacuum wave vector of the photon. This systematic effect must be accounted for in high-precision atom interferometry with light gratings.

DOI: 10.1103/PhysRevLett.94.170403 PACS numbers: 03.75.Dg, 39.20.+q, 42.50.Ct

The momentum of a photon in a dispersive medium is of conceptual and practical importance [1–6]. When light enters a medium with an index of refraction n, the electromagnetic momentum is modified [3–5]. Momentum conservation requires then that the medium also has a mechanical momentum. When a pulse of light enters the medium, the particles in the medium are accelerated by the leading edge of the pulse and decelerated by the trailing edge [5]. As a result, no motion is left in the medium after the pulse has passed. When light is absorbed or reflected in the medium, the momentum transfer occurs in units of $\hbar k$ or $n\hbar k$, where k is the vacuum wave vector. An absorbing surface is equivalent to photons leaving the medium without reflection and would therefore receive a momentum of $\hbar k$ per incident photon. In contrast, as shown in Ref. [5], a reflecting surface within the medium will recoil with a momentum of $2n\hbar k$ per photon. In this case, the standing wave formed by the incident and reflected light pulse transfers momentum to the medium which remains even after the light pulse has left. This modification of the recoil momentum has so far been observed only for light being reflected from a mirror immersed in a liquid [7,8].

Recently, there have been discussions about what happens when an atom within an atomic cloud absorbs a photon. If one assumes that after absorbing the photon, no motion is left in the medium, then the recoil momentum should be $\hbar k$ [9]. The same conclusion is reached when one assumes a very dilute, dispersive medium with the absorbing atom localized in the vacuum space between the particles of the medium [10]. However, Ref. [6] argues that the atom will recoil with a momentum of $n\hbar k$, which requires particles in the medium to receive a backward momentum (for $n > 1$) due to the interaction of the oscillating dipole moments of the particles in the dispersive medium and the absorbing atom. So both for reflection by a mirror and absorption by an atom, a photon in a dispersive medium behaves as if it has a momentum of $n\hbar k$.

In this Letter, we examine this issue experimentally, showing that the atom recoils with momentum $n\hbar k$. This has important consequences for atom interferometers using optical waves to manipulate atoms by the transfer of recoil momentum. High-precision measurements of the photon recoil are used to determine the fine-structure constant α [11–16]. Further improvements in the accuracy of photon recoil measurements, combined with the value of α derived from the $(g-2)$ measurements for the electron and positron [17–19], would provide a fundamental test of QED. At low atomic densities, where atom interferometers usually operate, the index of the refraction effect is relatively small. However, the accuracy of the best photon recoil measurements is limited by the uncertainty in the correction to the photon recoil due to the index of refraction. Here we operate an atom interferometer with Bose-Einstein

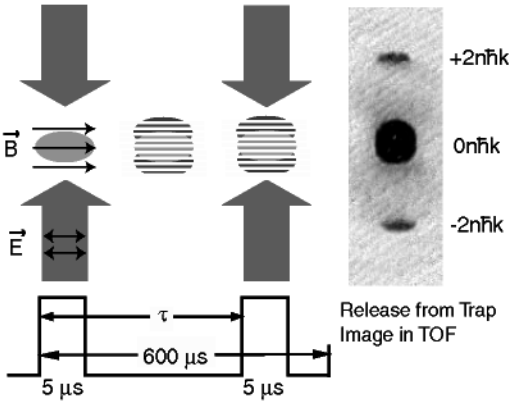

FIG. 1. Kapitza-Dirac interferometer. The first pulse outcoupled a small fraction of atoms into the $|\pm 2n\hbar k\rangle$ momentum states. The outcoupled atoms moved within the initial condensate. After a variable delay τ, a second pulse was applied, and atoms outcoupled by the second pulse interfered with those outcoupled by the first pulse. The laser beam was applied perpendicular to the long axis of the condensate; the polarization, $\vec{E}$, was parallel to it and to the applied magnetic field bias, $\vec{B}$. The atoms were imaged after 38 ms of ballistic expansion. The field of view is 0.5 mm × 1.5 mm.

condensates, which have a much higher density than laser cooled atomic clouds, and observe how the index of refraction modifies the atomic recoil frequency $\hbar\omega_{\rm rec} = \frac{\hbar^2 k^2}{2m}$, where m is the atomic mass.

The essential idea of our experiment is to measure the recoil frequency interferometrically using a two-pulse Ramsey interferometer. The two pulses are optical standing waves separated by a delay time τ (Fig. 1). The first pulse diffracts the atoms in a ^{87}Rb condensate into discrete momentum states. During the delay time τ the phase of each momentum state evolves at a different rate according to its recoil energy. The second pulse recombines the atoms with the initial condensate. The recombined components have differing phases leading to interference fringes that oscillate at the two-photon recoil frequency. By measuring the resulting frequency, ω as a function of the standing wave detuning from the atomic resonance, we found a distinctive dispersive shape for ω that fits the recoil momentum as $n\hbar k$.

The experiment was performed using an elongated ^{87}Rb Bose-Einstein condensate (BEC) created in a cloverleaf-type Ioffe-Pritchard magnetic trap previously described in Ref. [20]. The condensate, containing 1.5×10^6 atoms, was produced in the $|5\,^2S_{1/2}, F = 1, m_F = -1\rangle$ state, and had a Thomas-Fermi radius of 8 (90) μm in the radial (axial) direction, and the magnetic trap had a radial (axial) trap frequency of 81 (7) Hz.

The BEC was illuminated with an optical standing wave created by a retroreflected, π-polarized laser beam. Losses in the retroreflected beam were negligible. The polarization of the beam was optimized by suppressing Rayleigh superradiance [20]. The laser was detuned from the $5\,^2S_{1/2}, F = 1 \rightarrow 5\,^2P_{3/2}, F = 1$ transition at $\lambda = 780$ nm, and had a linewidth γ much smaller than Γ, the natural linewidth of the transition. The intensity of the 5 μs long pulse was set to outcouple $\approx 5\%$ of the atoms into each of the $|\pm 2n\hbar k\rangle$ momentum states with no appreciable population in higher momentum states. This ensured that the density of the original condensate was nearly constant throughout the measurement. After a variable time τ, a second identical pulse was applied. The time between the first pulse and the shutoff of the magnetic trap was fixed at 600 μs, which was less than a quarter of the radial trap period. The momentum distribution of the condensate was imaged after 38 ms of ballistic expansion, long enough for the momentum states to be resolved. The images were obtained using resonant absorption imaging after first optically pumping the atoms to the $5\,^2S_{1/2}, F = 2$ state. To measure the effect of spontaneous light scattering from the standing wave, the density of the condensate (and associated mean-field shift) was determined after applying a single 5 μs pulse to the condensate, and then immediately releasing it from the magnetic trap. The number of atoms in the condensate was determined by integrating the optical density of the absorption image, which in turn was calibrated by fitting the Thomas-Fermi radius of unperturbed condensates in time of flight [21].

The recoil frequency was found by fitting the oscillations in the fraction of atoms in the $|0n\hbar k\rangle$ momentum state as a function of the delay τ (Fig. 2) with a cosine function and a Gaussian envelope:

$$A \exp\left(-\frac{\tau^2}{\tau_c^2}\right)\cos(\omega\tau + \phi) + C. \quad (1)$$

The observation of up to ten oscillations provided a precise value of the recoil frequency. The origin of the damping time τ_c and of the offset C will be discussed later.

Figure 3 shows our measured values for $\omega/2\pi$ as a function of the detuning, $\Delta/2\pi$. The measured values for the frequency clearly follow the dispersive shape of the index of refraction. The variation in $\omega/2\pi$ as a function of the detuning was 2 kHz across the resonance, much larger than the statistical error on the frequency fits of less than 100 Hz. This conclusively shows that the momentum transferred to the atom when a photon is absorbed is $n\hbar k$.

We now discuss in more detail how the atoms interact with optical standing waves. For the short duration of the applied pulses (5 μs) we can assume that the atoms do not move during the pulse and ignore the kinetic energy of the atoms (Raman-Nath approximation). The interaction can then be described by the application of the ac Stark potential due to the standing wave $V(z) = \frac{\hbar\omega_R^2}{\Delta}\sin^2(nkz)$, where

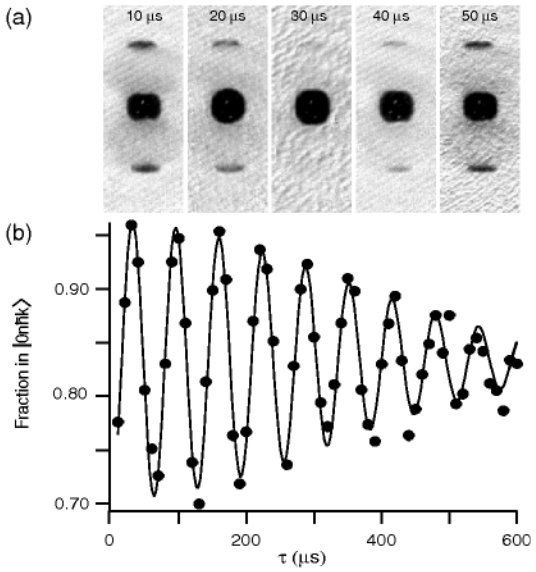

FIG. 2. Interference fringes oscillating at the recoil frequency. (a) Absorption images for $\tau = 10$–50 μs. The detuning was $\Delta/2\pi = +520$ MHz. The field of view is 0.5 mm $\times$ 1.5 mm. (b) Fraction of atoms in the $|0\hbar k\rangle$ momentum state as a function of τ. The fringes were fit using Eq. (1). The fitted frequency was $\omega = 2\pi \times 15\,627(39)$ Hz with decay constant $\tau_c = 461(25)$ μs. The signal was normalized using the total atom number in all momentum states. The systematic scatter of the data from the fit indicates the reproducibility of the single shot measurements.

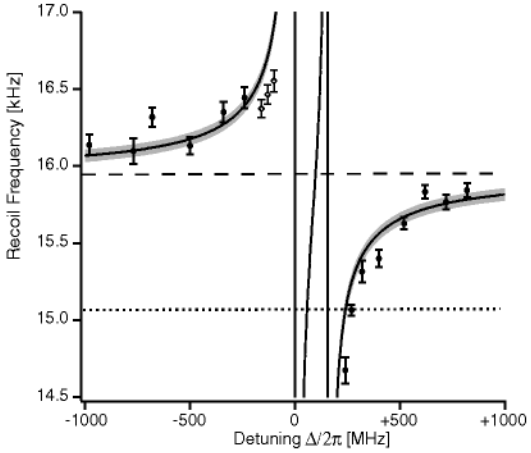

FIG. 3. Recoil frequency as a function of detuning, $\Delta/2\pi$, showing the dispersive effect of the index of refraction. The average density of the condensate for the solid points was $1.14(4) \times 10^{14}$ cm^{-3}, giving rise to a mean-field shift of 880 Hz. The shaded area gives the expected recoil frequency including the uncertainty in the density. The dashed line is at $\omega = 4\omega_{\rm rec} + \rho U/\hbar$, the expected value without index of refraction effects. The dotted line is at $4\omega_{\rm rec} = 15\,068$ Hz, the two-photon vacuum recoil frequency. The data shown as open diamonds had increased spontaneous light scattering due to $\sigma^{\pm}$ light contamination in the laser beam. The increased light scattering led to a lower initial density in the condensate, thus leading to a smaller mean-field shift. The $\sigma^{\pm}$ contamination allowed $\Delta m_F = \pm 1$ transitions, thus for small detunings the proximity to the $|1,-1\rangle \rightarrow |0',0\rangle$ transition located at $\Delta/2\pi = -72$ MHz resulted in higher spontaneous scattering rates. The open points have been scaled upward to correct for this lower density.

Δ is the detuning between the optical frequency and the atomic transition, and $\omega_{\rm R}$ is the Rabi frequency. This equation is valid for large detuning, $\Delta^2 \gg \Gamma^2/4$. The short pulse limit, describing Kapitza-Dirac scattering, is valid for short interaction times $t_p \ll 1/\omega_{\rm rec} \approx 40$ μs. The first pulse outcouples a fraction of atoms into the momentum states $|\pm 2\ell n\hbar k\rangle$, where the population in the ℓth momentum state is given by $P_\ell = J_\ell^2(\theta)$ [22,23], where for a square pulse, $\theta = \frac{\omega_{\rm R}^2 t_p}{2\Delta}$, and J_ℓ is the ℓth-order Bessel function of the first kind. For $\theta < 1$ a negligible fraction of atoms is diffracted into states with $\ell > 1$, and we can restrict our discussion to the $|\pm 2n\hbar k\rangle$ states. For our experimental parameters $\theta = 0.45$. During the delay time τ the phase of the $|\pm 2n\hbar k\rangle$ states evolves at a faster rate than the $|0n\hbar k\rangle$ state due to the recoil energy, $E_{\rm rec} = 4n^2\hbar\omega_{\rm rec}$; hence, the wave function evolves as

$$|\psi(\tau)\rangle = |\psi_o\rangle[J_1(\theta)|\pm 2n\hbar k\rangle e^{-i4n^2\omega_{\rm rec}\tau} + J_0(\theta)|0n\hbar k\rangle]. \quad (2)$$

At $t = \tau$ a second pulse is applied that partially recombines the momentum states. After applying the two pulses, the probability of finding the atoms in the $|0n\hbar k\rangle$ state, $\rho_0 = |\langle\psi(\tau + t_p)|0n\hbar k\rangle|^2$, is given by

$$\rho_0 = J_0^4(\theta) + 4[J_0^2(\theta)J_1^2(\theta) + J_1^4(\theta)]\cos(4n^2\omega_{\rm rec}\tau). \quad (3)$$

As a function of τ the density of the zero momentum peak oscillates at $4n^2\omega_{\rm rec}$.

So far, we have ignored the motion of the atoms during the delay time τ. The amplitudes of the recombined components interfere only where they spatially overlap. After the first pulse, the atoms in the $|\pm 2n\hbar k\rangle$ states move with the recoil velocity ($v_{\rm rec} \sim 12$ μm/ms). As the overlap between the recoiling atoms and those at rest decreases, the interference fringes decay. The overlap integral for this decay is approximated as a Gaussian with time constant, $\tau_c \approx 0.75 R_{\rm TF}/v_{\rm rec}$, where $R_{\rm TF}$ is the Thomas-Fermi radius of the condensate [24].

The index of refraction for the condensate is derived from its macroscopic polarization P. For a two level system, $P = \chi\epsilon_o E = i\rho\frac{\mu^2}{\hbar}\frac{E}{\Gamma - i\Delta}$, where χ is the atomic susceptibility, ϵ_o is the permittivity of free space, μ is the dipole matrix element, ρ is the atomic density of the condensate. In this experiment the light was π polarized and detuned by Δ from the $5\,^2S_{1/2}, F = 1 \rightarrow 5\,^2P_{3/2}, F' = 1$ transition. For this polarization the selection rule is $\Delta m_F = 0$, and there are two allowed transitions from $|F = 1, m_F = -1\rangle \rightarrow |1',-1\rangle$ and $|1,-1\rangle \rightarrow |2',-1\rangle$ that are separated by 157 MHz. Including both transitions in the derivation, the index of refraction, $n = \sqrt{1+\chi}$, is given by

$$n = \sqrt{1 - 12\pi\rho\lambda^3\left(\frac{5}{12}\frac{\Delta_1}{\Gamma}\frac{1}{1+(2\frac{\Delta_1}{\Gamma})^2} + \frac{1}{4}\frac{\Delta_2}{\Gamma}\frac{1}{1+(2\frac{\Delta_2}{\Gamma})^2}\right)}, \quad (4)$$

where Δ_1 and Δ_2 are the detunings relative to the $F = 1 \rightarrow F' = 1$ and $F' = 2$ transitions, respectively. This equation is valid in the limit $\rho\lambda\!\!\!^{-3} \ll 1$ [25], where $\lambda\!\!\!^{-} = \lambda/2\pi$. For our experimental parameters $\rho\lambda\!\!\!^{-3} \approx 0.2$. In addition to the index of refraction shift, the observed recoil frequency has a mean-field shift [26]; the atoms in the $|\pm 2n\hbar k\rangle$ state have twice the mean-field energy of those at rest due to the exchange term in the interatomic potential. Including both the mean-field shift and the index of refraction, the frequency of the observed interference fringes should be

$$\omega = 4n^2\omega_{\rm rec} + \frac{\rho U}{\hbar}, \quad (5)$$

where $\rho U = 4\pi\hbar^2 a\rho/m$, and a is the s-wave scattering length. The density $\rho = (4/7)\rho_o$, where ρ_o is the peak condensate density and the factor of 4/7 is due to the inhomogeneous condensate density.

When the interference fringes were fit using Eq. (1), the average values for the amplitude A and offset C for all of the data points were 0.12(3) and 0.82(4), respectively. This is in reasonable agreement with the expected values of $A = 0.18$ and $C = 0.81$ for $\theta = 0.45$. For a Thomas-Fermi radius of 8 μm we would expect a decay time $\tau_c \approx 500$ μs. There was an unexplained shift in the fitted value

for τ_c between the red and blue side of the resonances: on the red side the average value was 347(20) μs and on the blue, 455(40) μs.

The quadratic dependence in Eq. (5) on the index of refraction can be understood by considering the diffraction of atoms from the light grating created by the standing wave. When the first pulse is applied, the standing wave creates a grating with a periodicity $d = \lambda/2$. Within the condensate the index of refraction modifies the grating period by n, since $\lambda' = \lambda/n$. The momentum of atoms that diffract off the grating is changed by $\pm 2\hbar k'$, again within the condensate $k' = nk$, and the velocity of the atoms is modified. Assuming $n > 1$, when the second grating is applied the atoms have moved farther by a factor of n and the grating is shorter by n, changing the time scale for the interference fringes by a factor of n^2.

The increase in the momentum transferred to the atoms can also be explained by considering the momentum transferred to atoms by a classical field. A derivation using the Lorentz force applied to the atoms during the absorption of a photon can be found in [6]. In a dielectric medium with $n > 1$, the magnetic field and therefore the Lorentz force are not modified. However, the electric field is weaker, and therefore it takes longer for the atom to perform half a Rabi cycle and be transferred to the excited state. During that longer time, the Lorentz force imparts a momentum to the atom which is larger than $\hbar k$.

For Kapitza-Dirac scattering, atoms are diffracted symmetrically into the $|\pm 2\ell n\hbar k\rangle$ momentum states, so momentum is clearly conserved. However, for processes such as Bragg scattering, where the atoms are scattered in only one direction, the index of refraction has an additional effect. Assuming a $\pi/2$ pulse with counterpropagating beams, where half the atoms are diffracted, for $n > 1$ the recoil momentum is a factor of n higher than in vacuum. For momentum to be conserved, the remaining atoms must recoil backwards with momentum $p = 2(n-1)\ell\hbar k$. For small fractional outcoupling the effect is negligible, since the extra momentum is distributed among the remaining condensate. However, if a large fraction of the condensate is outcoupled and ℓ is large, this effect could potentially be resolved in ballistic expansion.

We have discussed here the dispersive effect on the photon momentum near a one-photon resonance. An analogous effect occurs near two-photon resonances. In this case, the atomic polarizability is determined in third-order perturbation theory, and the resulting index of refraction has a sharp, narrow dispersive feature near the two-photon resonance [27]. In recent experiments at Stanford [13], such two-photon effects have been the leading source of uncertainty in high-precision determinations of atomic recoil frequencies and the fine-structure constant α.

In conclusion, we have measured a systematic shift in the photon recoil frequency due to the index of refraction of the condensate. This is the first direct observation of the atomic recoil momentum in dispersive media. For high atomic densities, this shift can have a significant effect on atom interferometers, and is of particular importance for precision measurements of h/m and α with cold atoms [13,16].

The authors thank A. Schirotzek, S. Chu, S. Harris, and H. Haus for insightful discussions, and M. Kellogg for experimental assistance. This work was supported by NSF and ARO.

*Present address: JILA, Boulder, CO 80309, USA.
†Electronic address: http://cua.mit.edu/ketterle_group/

[1] H. Minkowski, Nachr. Ges. Wiss. Göttingen 53 (1908).
[2] H. Minkowski, Math. Ann. **68**, 472 (1910).
[3] M. Abraham, Rend. Circ. Mat. Palermo **28**, 1 (1909).
[4] M. Abraham, Rend. Circ. Mat. Palermo **30**, 33 (1910).
[5] J. P. Gordon, Phys. Rev. A **8**, 14 (1973).
[6] M. P. Haugan and F. V. Kowalski, Phys. Rev. A **25**, 2102 (1982).
[7] R. V. Jones and J. C. S. Richards, Proc. R. Soc. London A **221**, 480 (1954).
[8] R. V. Jones and B. Leslie, Proc. R. Soc. London A **360**, 347 (1978).
[9] J. M. Hensley, A. Wicht, B. C. Young, and S. Chu, in *Atomic Physics 17, Proceedings of the 17th International Conference on Atomic Physics*, edited by E. Arimondo, P. D. Natale, and M. Inguscio (AIP, Melville, NY, 2001).
[10] This argument has been made previously by one of the authors (W. K.).
[11] B. Taylor, Metrologia **31**, 181 (1994).
[12] D. S. Weiss, B. C. Young, and S. Chu, Phys. Rev. Lett. **70**, 2706 (1993).
[13] A. Wicht, J. M. Hensley, E. Sarajlic, and S. Chu, Phys. Scr. **T102**, 82 (2002).
[14] S. Gupta, K. Dieckmann, Z. Hadzibabic, and D. E. Pritchard, Phys. Rev. Lett. **89**, 140401 (2002).
[15] R. Battesti *et al.*, Phys. Rev. Lett. **92**, 253001 (2004).
[16] Y. L. Coq *et al.*, cond-mat/0501520.
[17] R. S. Van Dyck, P. B. Schwinberg, and H. G. Dehmelt, Phys. Rev. Lett. **59**, 26 (1987).
[18] T. Kinoshita, Phys. Rev. Lett. **75**, 4728 (1995).
[19] V. W. Hughes and T. Kinoshita, Rev. Mod. Phys. **71**, S133 (1999).
[20] D. Schneble *et al.*, Science **300**, 475 (2003).
[21] Y. Castin and R. Dum, Phys. Rev. Lett. **77**, 5315 (1996).
[22] P. Meystre, *Atom Optics* (Springer-Verlag, New York, 2001).
[23] S. Gupta, A. E. Leanhardt, A. D. Cronin, and D. E. Pritchard, C.R. Acad. Sci. IV Phys. **2**, 479 (2001).
[24] M. Trippenbach *et al.*, J. Phys. B **33**, 47 (2000).
[25] O. Morice, Y. Castin, and J. Dalibard, Phys. Rev. A **51**, 3896 (1995).
[26] J. Stenger *et al.*, Phys. Rev. Lett. **82**, 4569 (1999).
[27] A. Schirotzek, Diploma thesis, Universität Hamburg, 2004.

Appendix B

Parametric Amplification

This appendix contains a reprint of Ref. [13]: G.K. Campbell, J.M. Mun, M. Boyd, E.W. Streed,W. Ketterle, and D.E. Pritchard, *Parametric Amplification of Scattered Atom Pairs*, Phys. Rev. Lett. **96**, 020406 (2006).

Parametric Amplification of Scattered Atom Pairs

Gretchen K. Campbell, Jongchul Mun, Micah Boyd, Erik W. Streed, Wolfgang Ketterle, and David E. Pritchard*

MIT-Harvard Center for Ultracold Atoms, Research Laboratory of Electronics and Department of Physics, Massachusetts Institute of Technology, Cambridge, Massachusetts 02139, USA

(Received 12 September 2005; published 19 January 2006)

We have observed parametric generation and amplification of ultracold atom pairs. A ^{87}Rb Bose-Einstein condensate was loaded into a one-dimensional optical lattice with quasimomentum k_0 and spontaneously scattered into two final states with quasimomenta k_1 and k_2. Furthermore, when a seed of atoms was first created with quasimomentum k_1 we observed parametric amplification of scattered atoms pairs in states k_1 and k_2 when the phase-matching condition was fulfilled. This process is analogous to optical parametric generation and amplification of photons and could be used to efficiently create entangled pairs of atoms. Furthermore, these results explain the dynamic instability of condensates in moving lattices observed in recent experiments.

DOI: 10.1103/PhysRevLett.96.020406 PACS numbers: 03.75.Kk, 03.75.Lm, 05.45.−a

Nonlinear atom optics is a novel research area born with the advent of Bose-Einstein condensates of alkali atoms [1]. Unlike photons, ultracold atoms have a very strong nonlinearity directly provided by s-wave collisions, and therefore they do not need a nonlinear medium to provide effective interaction. A number of nonlinear processes first observed with photons have been demonstrated with matter waves such as four-wave mixing [2,3], solitons [4–7], second-harmonic generation [8–11], and sum-frequency generation [9]. Nonlinear atom optics, and, in particular, four-wave mixing, has previously been suggested as an ideal way to create entangled pairs of atoms [3,12,13]. However, in previous four-wave mixing experiments [2,3] using condensates in free space, the quadratic dispersion relation for free particles only allowed for the phase-matching condition to be fulfilled when the magnitudes of all four momenta were equal (in the center-of-mass frame). This is the only way in which two particles can scatter off each other and conserve energy and momentum. In particular, in free space, if a condensate is moving with momentum k_0, atoms within the condensate cannot elastically scatter into different momentum states, and therefore the analog to optical parametric generation of photons is not possible.

The situation is very different when an optical lattice is added. The lattice delivers energy in the form of the ac Stark effect and momentum in units of $2\hbar k_L$ to the atoms, where k_L is the wave vector of the optical lattice. The motion of atoms in this periodic potential is described by a band structure, which deviates from the quadratic free particle dispersion curve. In a lattice, as recently suggested [14], it becomes possible for two atoms in the condensate to collide and scatter into a higher and lower quasimomentum state and conserve energy. As we discuss below, this can lead to dynamic instabilities of the condensate, but also enables nondegenerate four-wave mixing and the atom-optics analog of optical parametric generation.

Phase matching is essential for high efficiency in nonlinear processes in quantum optics including optical parametric generation of photons [15], and a modification of the dispersion curve has been used to demonstrate optical parametric amplification in semiconductor microcavities [16]. In atom optics, dispersion management was used to modify the effective mass of atoms [17], and to create bright gap solitons [18]. Here we demonstrate that by modifying the dispersion curve using an optical lattice, scattering processes which cannot occur in free space become possible, and we realize the matter-wave analogue of an optical parametric generator (OPG) and an optical parametric amplifier (OPA).

To demonstrate the matter-wave analogue of an OPG, a ^{87}Rb Bose-Einstein condensate with quasimomentum k_0 was loaded into a one-dimensional optical lattice. To load the atoms at a given quasimomentum relative to the Brillouin zone, a moving optical lattice was adiabatically applied to a magnetically trapped condensate initially at rest in the lab frame. The lattice was created using two counter-propagating laser beams with frequency difference $\delta\nu$, giving the lattice a velocity of $v = \frac{\lambda}{2}\delta\nu$, where λ is the wavelength of the optical lattice. In the rest frame of the lattice, the condensate has quasimomentum $k_0 = \frac{m\lambda}{2\hbar}\delta\nu$, where m is the atomic mass. By changing the detuning between the lattice beams, $\delta\nu$, k_0 could be varied. As shown in Fig. 1(d), as the value of k_0 was varied we observed elastic scattering of atom pairs into final states k_1 and k_2. The range of possible final states varied with k_0 due to the phase-matching condition. For values of k_0 less than $\approx 0.55k_L$ the dispersion relation imposed by the Bloch structure of the optical lattice does not allow elastic scattering to occur. For our lattice depth of $V = 0.5E_{\mathrm{rec}}$, where $E_{\mathrm{rec}} = \hbar^2k_L^2/2m$, the values of k_2 which satisfied energy and momentum conservation were beyond the first Brillouin zone. Since the scattering process occurs within the first Bloch band, the atoms in state k_2 have a quasimomentum $k_2 = (2k_0 - k_1)\mathrm{Mod}\,(2k_L)$ [see Fig. 1(a)]. As the value for $\delta\nu$ (and the resulting value of k_0) is increased, the separation between k_0 and the allowed states k_1 and k_2 decreases as is clearly observed in Fig. 1(d). For values of

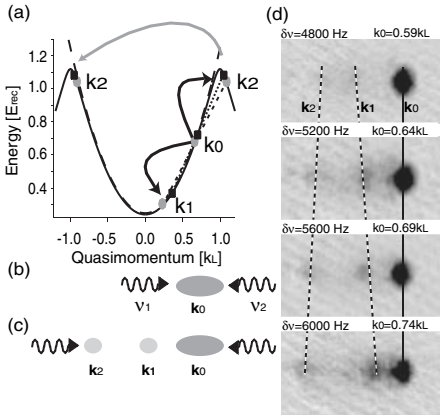

FIG. 1. Dispersion curve for the optical lattice and experimental setup. (a) Band structure for a lattice depth of $V = 0.5E_{\mathrm{rec}}$. The dashed line shows the free particle dispersion curve. The dispersion relation of the lattice allows two atoms with momentum k_0 to elastically scatter into the final momentum states k_1 and k_2. Energy and quasimomentum are conserved when k_0 is the average of k_1 and k_2 and the three points on the dispersion curve lie on a straight line. If k_0 is varied, the allowed values for k_1 and k_2 change. For values of k_0 below $\approx 0.55k_L$, where k_L is the wave vector of the optical lattice, atoms cannot scatter elastically into different momentum states. The circles (squares) show allowed states k_0, k_1, k_2 for $k_0 = 0.66k_L$ ($0.70k_L$). As k_0 is increased, the final momentum states move closer together. Since the scattering occurs within the lowest band of the lattice, the final momentum is $k_2 = (2k_0 - k_1)\mathrm{Mod}\,(2k_L)$. (b) A ^{87}Rb Bose-Einstein condensate is illuminated by two counter-propagating laser beams with detuning $\delta\nu$, which create a moving optical lattice. The condensate is initially held at rest. In the rest frame of the lattice, the condensate has quasimomentum $k_0 = \frac{m\lambda}{2\hbar}\delta\nu$. (c) As k_0 was varied, we observed elastic scattering into states k_1 and k_2. (d) Absorption images for different lattice detunings, $\delta\nu$, showing parametric generation. After ramping up the lattice, the atoms were held for 10 ms at a constant lattice depth. They were then released from the trap and imaged after 43 ms of ballistic expansion. The field of view is 0.5 mm $\times$ 0.3 mm.

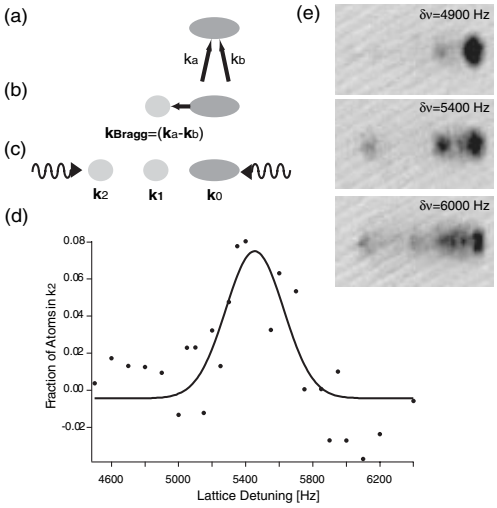

FIG. 2. Parametric amplification of scattered atom pairs in a 1D optical lattice. (a) First, a 2 ms Bragg pulse was applied to the condensate. (b) The Bragg pulse seeded atoms along the long axis of the condensate with momentum $k_{\mathrm{Bragg}} = (k_a - k_b)$ in the lab frame. (c) The optical lattice was then adiabatically ramped on and applied for 10 ms. When the phase-matching condition was fulfilled, parametric amplification of atoms in the seeded state k_1 and its conjugate momentum state k_2 was observed. (d) Resonance curve showing amplification of k_2, when k_1 was seeded. Amplification occurred only when the phase-matching condition was met. For a fixed k_{Bragg}, the resonance condition was found by varying the detuning $\delta\nu$ of the lattice. The data was taken for $k_{\mathrm{Bragg}} = 0.43k_L$. The fraction of amplified atoms was obtained by subtracting images with and without the seed pulse. (e) Absorption images showing amplification of k_1 and k_2 when the phase-matching condition is met. The center of the resonance was at $\delta\nu \approx 5450$ Hz, close to the calculated value of $\delta\nu \approx 5350$ Hz. The width of the resonance is determined by the Fourier width of the Bragg pulse. Most of the scattered atoms in the third image were independent of the seed pulse.

k_0 above $\approx 0.75k_L$, the final momentum states were no longer distinguishable, and the condensate became unstable.

To demonstrate the matter-wave analogue of an OPA, we first created a small seed of atoms with quasimomentum k_1 before ramping on the moving lattice (see Fig. 2). To create the seed we applied a Bragg pulse to the magnetically trapped condensate, outcoupling a small fraction of atoms into the momentum state k_{Bragg} [19]. Immediately after applying the pulse, the optical lattice was adiabatically ramped on. In the rest frame of the lattice, the seed has quasimomentum $k_1 = k_{\mathrm{Bragg}} + k_0$. The phase-matching condition for a given seed k_{Bragg} was found by varying the frequency difference $\delta\nu$ of the lattice, and therefore the quasimomenta k_0 and k_1 of the atoms. As shown in Fig. 2(d), when the phase-matching condition was fulfilled, we observed amplification of the seed k_1 as well as its conjugate momentum k_2. The growth of k_1 and k_2 as a function of time are shown in Fig. 3.

The experiments were performed using an elongated ^{87}Rb condensate created in a magnetic trap previously described in Ref. [20]. The magnetic trap had a radial (axial) trap frequency of 35(8) Hz. The condensate, containing between 0.5–3.0 $\times 10^5$ atoms, was produced in the $|5^2S_{1/2}, F = 1, m_F = -1\rangle$ state. The Bragg pulse was created with two laser beams derived from the same laser, which was red detuned from the $5^2S_{1/2}, F = 1 \rightarrow 5^2P_{3/2}, F = 1$ transition at $\lambda = 780$ nm by 400 MHz, and was π polarized. As shown in Fig. 2, the Bragg beams were aligned such that atoms were outcoupled along the long axis of the condensate. The intensity of the Bragg pulse was chosen such that less than 5% of the initial condensate was outcoupled into k_{Bragg}, and the length of the pulse was 2 ms. The angle between the Bragg beams could be varied to change the momentum of the outcoupled atoms. The optical lattice was created using two counter-

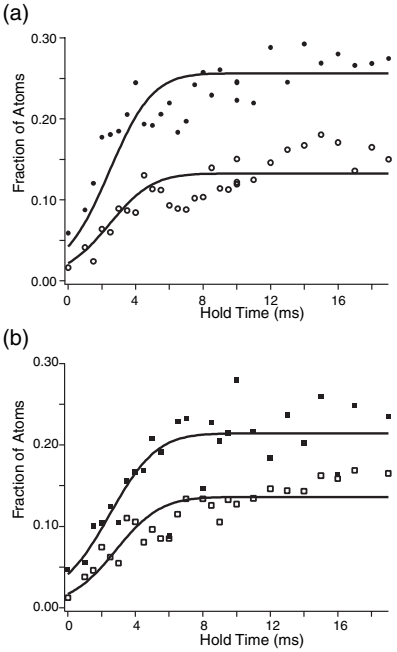

FIG. 3. Growth curve for atomic population in quasimomentum states k_1 and k_2 when the process was seeded. (a) Amplification of atoms with quasimomentum k_1 (solid points), and with the conjugate momentum k_2 (open points), when state k_1 was seeded. (b) Amplification of atoms in k_1 (solid points), and k_2 (open points), when k_2 was seeded. The values for k_0, k_1, k_2 were $0.66k_L$, $0.23k_L$, and $-0.92k_L$ respectively. The solid lines shows the expected gain using Eq. (1) with variable scale factors for each curve as the only free parameters.

propagating beams derived from the same laser with $\lambda = 1064$ nm, and the frequency of the two beams were controlled by two separate acousto-optic modulators (AOMs) driven with a frequency difference $\delta\nu$. The lattice was also aligned along the long axis of the condensate, and was ramped on in 1 ms using an exponential ramp. After the condensate was held in the lattice for a variable time τ it was then released from the trap and imaged after 43 ms of ballistic expansion.

For all of our experiments, the depth of the optical lattice was $V = 0.5E_{\mathrm{rec}}$ with a band structure shown in Fig. 1. When the process was not seeded, atoms were elastically scattered into a narrow band of states k_1 and k_2, where both energy and momentum were conserved. However, the population in neither state was large enough for amplification to be observed. When the process was seeded, amplification occurred when the quasimomentum was tuned such that energy and momentum were conserved for the states k_0, k_1, and the conjugate momentum k_2. In our experiment, the difference $\Delta k = k_0 - k_1$ between the quasimomenta of the condensate k_0 and seed k_1 was set by the angle of the initial Bragg pulse. For a given Bragg angle, there is only one set of quasimomenta k_0, k_1, and k_2 where the phase-matching condition is fulfilled. To find this point, we varied the velocity of the moving lattice for fixed hold times. Results for $k_{\mathrm{Bragg}} = 0.43k_L$ are shown in Fig. 2. The phase-matched value for k_2 is at $1.08k_L$, beyond the boundary of the first Briollouin zone. Therefore, the atoms are observed with a momentum $k_2 = -0.92k_L$. For $k_{\mathrm{Bragg}} = 0.43k_L$, $0.34k_L$, and $0.28k_L$, we observed resonances at $\delta\nu = 5450$ Hz, 5750 Hz, and 6100 Hz, respectively. For these Bragg angles and our lattice depth, the expected values were 5350 Hz, 5700 Hz, and 6050 Hz.

In Fig. 3, 5% of the initial condensate containing $N_0 = 1.3(3) \times 10^5$ atoms was outcoupled with $k_{\mathrm{Bragg}} = 0.43k_L$. The gain for the process is determined by the strength of the nonlinear interaction $U = \frac{4\pi\hbar^2 a}{m}$ between atoms in the condensate, where a is the s-wave scattering length. We can estimate the maximum amplification rate to be $\eta = 2n_0U/\hbar$ [3], with $\dot{N}_{1(2)} = \eta N_{2(1)}$, where $N_{1(2)}$ is the number of atoms in the momentum state $k_{1(2)}$, and n_0 is the condensate density. For $N_0 = 1.3(3) \times 10^5$, the maximum growth rate should be $\eta = 540$ Hz. The amplification rate will decrease as the state k_0 is depleted. However, for our small seeds, the amplification was limited by the loss of overlap between the condensate and the amplified pulses. The Thomas-Fermi radius (R_{TF}) of the condensate in the axial direction was 33 μm, and the recoil velocity (v_{rec}) for the final states k_1 and k_2 with respect to the initial condensate was $v_{\mathrm{rec}} = 1.8$ μm/ms and 6.8 μm/ms, respectively. The overlap integral between the amplified atoms and the initial condensate can be approximated as a Gaussian with time constant $\tau_c \approx 0.75R_{\mathrm{TF}}/v_{\mathrm{rec}}$, which for our parameters is 3.75 ms. We compare our results to the modified rate equation

$$\dot{N}_{2(1)} = \eta N_{1(2)} e^{-t^2/\tau_c^2}. \quad (1)$$

Since atoms are scattered into states k_1 and k_2 in pairs, one would expect that the final atom number in the two states (minus the initial seed) are equal. Instead, we observe a smaller number in state k_2 which we ascribe to the proximity of k_2 to the boundary of Brillouin zone. This leads to instabilities, where atoms in state k_2 are scattered into other momentum states or into higher bands. If we allow a variable scale factor in our model to correct for the loss of atoms in N_2, as shown in Fig. 3, the gain for $N_{1,2}$ is in agreement with the experimental data.

Amplification was also observed when atoms were seeded in state k_2. Because of the geometry of our experimental setup, we were unable to load atoms directly into $k_2 = -0.92k_L$. However when atoms with quasimomentum $k = 1.08k_L$ were loaded into the lattice, the ramp-up was no longer adiabatic due to their proximity to the boundary of the first Brillouin zone. Because of this, atoms from the seed were loaded into both the second Bloch band (with $k = 1.08k_L$) and the ground state (with $k = -0.92k_L = k_2$). As shown in Fig. 3(b), the gain for this process was almost identical to when atoms were seeded in state k_1.

The loss of overlap could be alleviated by using a more extreme trap geometry in which the condensate is more elongated, e.g., by confining atoms in a tight transverse optical lattice. In this configuration, it may be possible to observe the parametric scattering dynamics for longer time scales, which may allow for the observation of Rabi oscillations between k_0 and k_1, k_2 as predicted in Ref. [14]. For longer coherence times, parametric amplification could also be an efficient means of producing pairs of momentum entangled atoms for quantum information applications [12,13], but the issue of secondary collisions out of states k_1 and k_2 has to be carefully addressed.

For high atom numbers, and for large values of k_0, the condensate became unstable and scattered into a broad band of final momentum states [Fig. 2(e)]. For $k_{\mathrm{Bragg}} = 0.43k_L$, the energy of atoms outcoupled by the Bragg beams was ≈ 370 Hz, whereas the chemical potential of the condensate was ≈ 300 Hz. Because of this, if the atom number was increased significantly the momentum peaks were no longer distinguishable. When the chemical potential of the condensate was larger than the separation between the phase-matched momentum states, the process was self-seeded; i.e., the momentum spread of the initial condensate contained atoms with momentum k_0, k_1, and k_2, and considerable scattering occurred. Similarly, if the atom number was kept constant, and the value of k_0 was increased, the phase-matched momentum states moved closer together until they were no longer distinguishable. This occurred at values of k_0 above $\approx 0.75k_L$, and we observed a dynamic instability. For larger atom numbers, the critical value of k_0 decreases. For values of k_0 less than $0.55k_0$ elastic scattering cannot occur, and the system should be stable for all atom numbers. Instabilities of condensates in optical lattices has attracted much attention recently, both theoretically [21–28] and experimentally [29–33]. Most recently, dynamic instabilities of condensates in moving lattices were observed in Refs. [29,30]. In Ref. [30], the chemical potential was a factor of 3 higher than in our experiment, leading to a dynamic instability for all values of k_0 above $0.55k_L$. Although discrete momentum states could not be observed in those experiments, it is possible that the mechanism for the dynamic instability is self-seeded parametric amplification. Indeed, the phase-matching condition for parametric amplification is identical to the resonance condition for dynamic instability in the noninteracting limit [21]. After the submission of this Letter, recent work on period-doubling instabilities in a shaken optical lattice [34] was reinterpreted as parametric amplification [35].

In conclusion, we have demonstrated a matter-wave analogue of both optical parametric generation and optical parametric amplification using a condensate moving in a one-dimensional optical lattice. The optical lattice modified the dispersion curve and ensured phase matching. If the separation of the phase-matched momentum states becomes less than the speed of sound, a condensate will self-seed the process and become dynamically unstable.

The authors thank K. Mølmer for pointing out this physical process to us, M. Inguscio and M. Modugno for insightful discussions, M. Saba for helpful discussions and a critical reading of the manuscript, and P. Medley for experimental assistance. This work was supported by NSF and ARO.

*Electronic address: http://cua.mit.edu/ketterle_group/

[1] G. Lenz, P. Meystre, and E. M. Wright, Phys. Rev. Lett. **71**, 3271 (1993).
[2] L. Deng *et al.*, Nature (London) **398**, 218 (1999).
[3] J. M. Vogels, K. Xu, and W. Ketterle, Phys. Rev. Lett. **89**, 020401 (2002).
[4] J. Denschlag *et al.*, Science **287**, 97 (2000).
[5] S. Burger *et al.*, Phys. Rev. Lett. **83**, 5198 (1999).
[6] B. P. Anderson *et al.*, Phys. Rev. Lett. **86**, 2926 (2001).
[7] K. E. Strecker *et al.*, Nature (London) **417**, 150 (2002).
[8] R. Wynar *et al.*, Science **287**, 1016 (2000).
[9] J. R. Abo-Shaeer *et al.*, Phys. Rev. Lett. **94**, 040405 (2005).
[10] P. D. Lett *et al.*, Phys. Rev. Lett. **71**, 2200 (1993).
[11] J. D. Miller, R. A. Cline, and D. J. Heinzen, Phys. Rev. Lett. **71**, 2204 (1993).
[12] L.-M. Duan *et al.*, Phys. Rev. Lett. **85**, 3991 (2000).
[13] H. Pu and P. Meystre, Phys. Rev. Lett. **85**, 3987 (2000).
[14] K. M. Hilligsøe and K. Mølmer, Phys. Rev. A **71**, 041602(R) (2005).
[15] E. Rosencher, *Optoelectronics* (Cambridge University Press, Cambridge, England, 2002).
[16] P. G. Savvidis *et al.*, Phys. Rev. Lett. **84**, 1547 (2000).
[17] B. Eiermann *et al.*, Phys. Rev. Lett. **91**, 060402 (2003).
[18] B. Eiermann *et al.*, Phys. Rev. Lett. **92**, 230401 (2004).
[19] J. Stenger *et al.*, Phys. Rev. Lett. **82**, 4569 (1999).
[20] D. Schneble *et al.*, Science **300**, 475 (2003).
[21] B. Wu and Q. Niu, Phys. Rev. A **64**, 061603(R) (2001); New J. Phys. **5**, 104 (2003).
[22] A. Smerzi *et al.*, Phys. Rev. Lett. **89**, 170402 (2002); C. Menotti, A. Smerzi, and A. Trombettoni, New J. Phys. **5**, 112 (2003).
[23] M. Machholm *et al.*, Phys. Rev. A **69**, 043604 (2004).
[24] V. V. Konotop and M. Salerno, Phys. Rev. A **65**, 021602(R) (2002).
[25] R. G. Scott *et al.*, Phys. Rev. Lett. **90**, 110404 (2003).
[26] Y. Zheng, M. Kostrun, and J. Javanainen, Phys. Rev. Lett. **93**, 230401 (2004).
[27] M. Modugno, C. Tozzo, and F. Dalfovo, Phys. Rev. A **70**, 043625 (2004).
[28] C. Tozzo, M. Kramer, and F. Dalfovo, Phys. Rev. A **72**, 023613 (2005).
[29] L. Fallani *et al.*, Phys. Rev. Lett. **93**, 140406 (2004).
[30] L. De Sarlo *et al.*, Phys. Rev. A **72**, 013603 (2005).
[31] S. Burger *et al.*, Phys. Rev. Lett. **86**, 4447 (2001).
[32] F. S. Cataliotti *et al.*, New J. Phys. **5**, 71 (2003).
[33] M. Cristiani *et al.*, Opt. Express **12**, 4 (2004).
[34] N. Gemelke *et al.*, cond-mat/0504311.
[35] N. Gemelke *et al.*, Phys. Rev. Lett. **95**, 170404 (2005).

Appendix C

Imaging the Mott Insulator Shells using Atomic Clock Shifts

This appendix contains a reprint of Ref. [12]: G.K. Campbell, J. Mun, M. Boyd, P. Medley, A.E. Leanhardt, L. G. Marcassa, D.E. Pritchard, and W. Ketterle *Imaging the Mott Insulator Shells by Using Atomic Clock Shifts*, Science **313**, 649 (2006).

29. L. Fu, H. Pelicano, J. Liu, P. Huang, C.-C. Lee, *Cell* **111**, 41 (2002).
30. K. Unsal-Kacmaz, T. E. Mullen, W. K. Kaufmann, A. Sancar, *Mol. Cell. Biol.* **25**, 3109 (2005).
31. T. Matsuo *et al.*, *Science* **302**, 255 (2003).
32. N. A. Krucher, L. Meije, M. H. Roberts, *Cell. Mol. Neurobiol.* **17**, 495 (1997).
33. L. E. Anderson, J. E. Morris, L. B. Sasser, R. G. Stevens, *Cancer Lett.* **148**, 121 (2000).
34. J. Hansen, *Epidemiology* **12**, 74 (2001).
35. W. J. Hrushesky, *J. Control. Release* **74**, 27 (2001).
36. G. A. Bjarnason, R. Jordan, *Prog. Cell Cycle Res.* **4**, 193 (2000).
37. www.fgsc.net/fgn47/lgi.htm.
38. S. Gery, N. Komatsu, L. Baldjyan, A. Yu, D. Koo, H. P. Koeffler, *Mol. Cell* **22**, 375 (2006).
39. Supported by grants from the NIH (MH44651 to J.C.D. and J.J.L. and R37GM34985 to J.C.D.), NSF (MCB-0084509 to J.J.L.), and the Norris Cotton Cancer Center core grant to Dartmouth Medical School. We thank R. Rothstein for yeast strain W2105-7b, S. Elledge for plasmid pMH267, and both for helpful discussions.

Supporting Online Material
www.sciencemag.org/cgi/content/full/1121716/DC1
Materials and Methods
Figs. S1 and S2
References

24 October 2005; accepted 11 May 2006
Published online 29 June 2006;
10.1126/science.1121716
Include this information when citing this paper.

Imaging the Mott Insulator Shells by Using Atomic Clock Shifts

Gretchen K. Campbell,[1]* Jongchul Mun,[1] Micah Boyd,[1] Patrick Medley,[1] Aaron E. Leanhardt,[2] Luis G. Marcassa,[1]† David E. Pritchard,[1] Wolfgang Ketterle[1]

Microwave spectroscopy was used to probe the superfluid–Mott insulator transition of a Bose-Einstein condensate in a three-dimensional optical lattice. By using density-dependent transition frequency shifts, we were able to spectroscopically distinguish sites with different occupation numbers and to directly image sites with occupation numbers from one to five, revealing the shell structure of the Mott insulator phase. We used this spectroscopy to determine the onsite interaction and lifetime for individual shells.

The Mott insulator (MI) transition is a paradigm of condensed matter physics, describing how electron correlations can lead to insulating behavior even for partially filled conduction bands. However, this behavior requires a commensurable ratio between electrons and sites. If this condition for the density is not exactly fulfilled, the system will be conductive. For neutral bosonic particles, the equivalent phenomenon is the transition from a superfluid to an insulator for commensurable densities. In inhomogeneous systems, as in atom traps, the condition of commensurability no longer applies: For sufficiently strong interparticle interactions, it is predicted that the system should separate into MI shells with different occupation number, separated by thin superfluid layers (*1*–*3*).

The recent observation of the superfluid-to-MI transition with ultracold atoms (*4*) has stimulated a large number of theoretical and experimental studies [(*5*) and references therein]. Atomic systems allow for a full range of control of the experimental parameters, including tunability of the interactions and defect-free preparation, making them attractive systems for studying condensed matter phenomena. The MI phase in ultracold atoms has been characterized by studies of coherence, excitation spectrum, noise correlations (*4*, *6*, *7*), and molecule formation (*8*). Recently, by using spin-changing collisions, Gerbier *et al*. selectively addressed lattice sites with two atoms and observed the suppression of number fluctuations (*9*).

In this study, we combined atoms in the MI phase with the high-resolution spectroscopy used for atomic clocks and used density-dependent transition frequency shifts to spectroscopically resolve the layered structure of the Mott shells with occupancies from $n = 1$ to $n = 5$ and to directly image their spatial distributions.

Bosons with repulsive interactions in an optical lattice can qualitatively be described by the Hamiltonian (*10*, *1*),

$$\hat{H} = -J\sum_{\langle i,j\rangle} \hat{a}_i^\dagger a_j + {}^1\!/_2\, U\sum_i \hat{n}_i(\hat{n}_i - 1) + \sum_i (\varepsilon_i - \mu)\hat{n}_i \qquad (1)$$

where the first two terms are the usual Hamiltonian for the Bose-Hubbard model, the last term adds in the external trapping potential, and J is the tunneling term between nearest neighbors, $\hat{a}_i^\dagger$ and $\hat{a}_i$ are the boson creation and destruction operators at a given lattice site. $U = (4\pi\hbar^2 a/m)\int |w(x)|^4 d^3x$ is the repulsive onsite interaction, where $\hbar$ is Planck's constant divided by 2π, m is the atomic mass, a is the s-wave scattering length, $w(x)$ is the single particle Wannier function localized to the ith lattice site, and $\hat{n}_i = \hat{a}_i^\dagger \hat{a}_i$ is the number operator for bosons at site i. The last term in the Hamiltonian is due to the external trapping confinement of the atoms, where $\varepsilon_i = V_{\mathrm{ext}}(r_i)$ is the energy offset at the ith site due to the external confinement and μ is the chemical potential.

The behavior of this system is determined by the ratio J/U. For low lattice depths, the ratio is large and the system is superfluid. For larger lattice depths, the repulsive onsite energy begins to dominate, and the system undergoes a quantum phase transition to a MI phase. For deep lattices, the atoms are localized to individual lattice sites with integer filling factor n. This filling factor varies locally depending on the local chemical potential $\mu_i = \mu - \varepsilon_i$ as

$$n = Mod(\mu_i/U) \qquad (2)$$

where *Mod* is the modulo and decreases from the center to the edge of the trap.

To prepare the atoms in the Mott insulating phase, we first created a ^{87}Rb Bose-Einstein condensate in the the $|F = 1, m_F = -1\rangle$ state (where F and m_F are the quantum numbers for the total spin and its t component, respectively) by using a combination of an Ioffe-Pritchard magnetic trap and an optical dipole trap. The optical trap was oriented perpendicular to the long axis of the magnetic trap, creating a more isotropic trapping potential that was better matched to the optical lattice. The laser beam for the optical trap had a $1/e^2$ waist ≈ 70 μm and was retroreflected. However, the polarization of the retroreflected beam was rotated such that the interference between the two beams had minimal contrast. The resulting trap had radial and axial trap frequencies of $\omega = 2\pi \times 70$ Hz and $\omega = 2\pi \times 20$ Hz, respectively, where the axial direction is now parallel to the optical trap. A three-dimensional (3D) optical lattice was created by adding two additional retroreflected laser beams derived from the same laser at $\lambda = 1064$ nm. The lattice was adiabatically ramped up by rotating the polarization of the retroreflected optical trapping beam to increase the interference contrast along that axis and by increasing the laser power in the other two axes. The lattice depth was increased by using an exponential ramp with a 40-ms time constant. After ramping on the lattice, all three beams were linearly polarized orthogonal to each other and

[1]MIT-Harvard Center for Ultracold Atoms, Research Laboratory of Electronics, Department of Physics, Massachusetts Institute of Technology, Cambridge, MA 02139, USA. [2]JILA, Boulder, CO 80309, USA.

*To whom correspondence should be addressed. E-mail: gcampbel@mit.edu

†Permanent address: Instituto de Fisica de São Carlos, University of São Paulo, São Paulo 13560-970, Brazil.

had different frequency detunings generated by using acousto-optic modulators. The lattice depth was up to $40E_{rec}$, where $E_{rec} = \hbar^2k^2/2m$ is the recoil energy and $k = 2\pi/\lambda$ is the wave vector of the lattice light. At $40E_{rec}$, the lattice trap frequency at each site was $\omega_{lat} = 2\pi \times 25$ kHz, and the external trap frequencies increased to $\omega = 2\pi \times 110$ Hz and $\omega = 2\pi \times 30$ Hz in the radial and axial directions, respectively.

Zeeman shifts and broadening of the clock transition from the $F = 1$ to the $F = 2$ state were avoided by using a two photon transition between the $|1, -1\rangle$ state and the $|2, 1\rangle$ state, where at a magnetic bias field of ~ 3.23 G both states have the same first-order Zeeman shift (*11*). The two-photon pulse was composed of one microwave photon at a fixed frequency of 6.83 GHz and one radio frequency (rf) photon at a frequency of around 1.67 MHz. The pulse had a duration of 100 ms, and when on resonance the fraction of atoms transferred to the $|2, 1\rangle$ state was less than 20%. After the pulse, atoms in the $|2, 1\rangle$ state were selectively detected with absorption imaging by using light resonant with the $5^2S_{1/2}|2, 1\rangle \rightarrow 5^2P_{3/2}|3, 1\rangle$ transition. For observing the spatial distribution of the Mott shells, we imaged the atoms in the trap. For recording spectra, we released the atoms from the trap and imaged them after 3 ms of ballistic expansion in order to reduce the column density.

When the two-photon spectroscopy is performed on a trapped condensate without a lattice, the atoms transferred to the $|2, 1\rangle$ state have a slightly different mean field energy because of the difference between a_{21} and a_{11} scattering lengths, where a_{21} is the scattering length between two atoms in states $|2, 1\rangle$ and $|1, -1\rangle$ and a_{11} is the scattering length between two atoms in the $|1, -1\rangle$ state. This difference in scattering lengths leads to a density-dependent shift to the resonance frequency, $\Delta\nu \propto \rho(a_{21} - a_{11})$, where ρ is the condensate density (*11*). This collisional shift is commonly referred to as the clock shift (*12*) because of its importance in atomic clocks, where cold collisions currently limit the accuracy (*13*, *14*). When performed on a condensate with peak density ρ_0 in a harmonic trap in the limit of weak excitation, the line shape for the two-photon resonance is given by (*15*):

$$I(\nu) = \frac{15h(\nu - \nu_0)}{4\rho_0\Delta E}\sqrt{1 - \frac{h(\nu - \nu_0)}{\rho_0\Delta E}} \quad (3)$$

where ν_0 is the hyperfine transition frequency and the mean field energy difference is

$$\Delta E = \frac{h^2}{\pi m}(a_{21} - a_{11}) \quad (4)$$

In the case of ^{87}Rb, $a_{21} = 5.19$ nm and $a_{11} = 5.32$ nm (*16*). Both the frequency shift and the linewidth increase with the condensate density. As the lattice is ramped on, the peak density of the condensate in a given lattice site increases as

$$\rho_0(r) = \left(\mu - {}^1\!/_2\, m\omega_{trap}^2 r^2\right)1/U \quad (5)$$

where ω_{trap} is the external trap frequency for the combined magnetic and optical trap, and, by using the Thomas-Fermi approximation μ, the chemical potential, is given by

$$\mu = \left[{}^{15}\!/_{16}\,\frac{(\lambda/2)^3 m^{3/2} NU\omega_{trap}^3}{\sqrt{2}\pi}\right]^{2/5} \quad (6)$$

where N is the total atom number. For low lattice depths, the system is still a superfluid, delocalized over the entire lattice. However, the two-photon resonance line is shifted and broadened because of the increased density, with the center of the resonance at $\nu = \nu_0 + 2\rho_0\Delta E/3h$. For deep lattices in the MI regime, the repulsive onsite interaction dominates, number fluctuations are suppressed, and each lattice site has a sharp resonance frequency determined by the occupation number in the site. The separation between

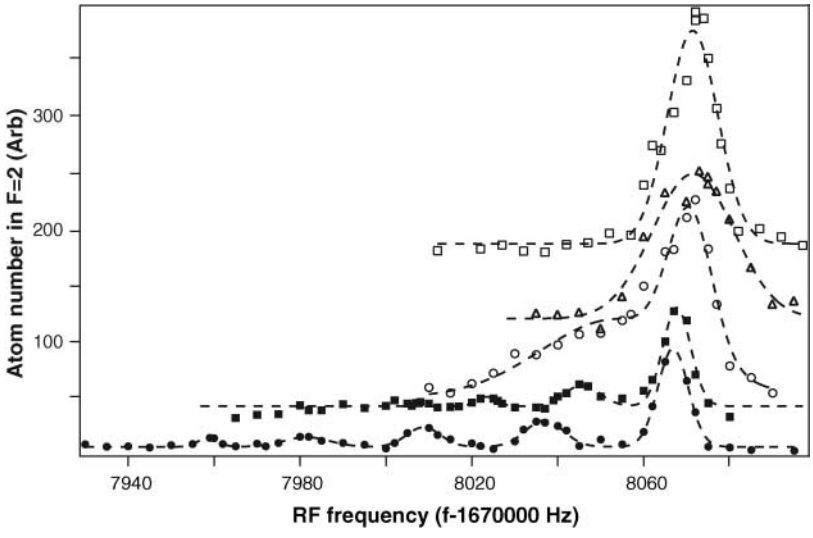

Fig. 1. Two-photon spectroscopy across the superfluid-to-MI transition. Spectra for 3D lattice depths of $0E_{rec}$ (open squares), $5E_{rec}$ (open triangles), $10E_{rec}$ (open circles), $25E_{rec}$ (solid squares), and $35E_{rec}$ (solid circles) are shown. The spectra are offset for clarity. The shift in the center of the $n = 1$ peak as the lattice depth is increased is due to the differential AC Stark shift from the lattice. The dotted lines show Gaussian fits of the peaks.

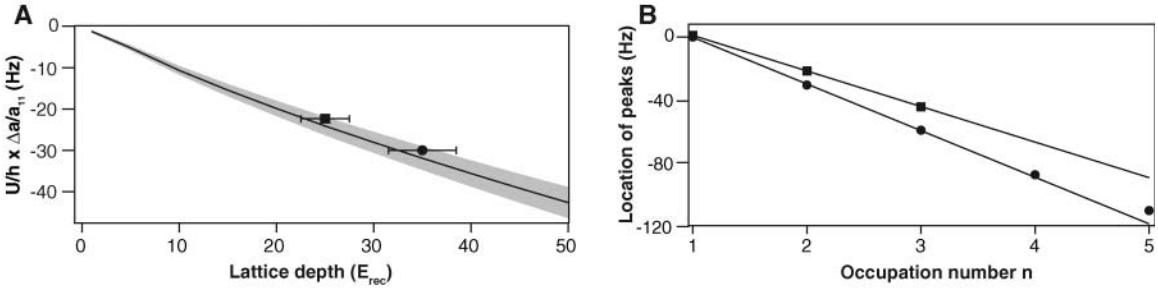

Fig. 2. Probing the onsite interaction energy. (**A**) The separation between the $n = 1$ and $n = 2$ peaks is shown for lattice depths of $V = 25E_{rec}$ (square) and $V = 35E_{rec}$ (circle). As the lattice depth was increased, the separation increased from 22(1) Hz to 30(1) Hz. The shaded area gives the expected value determined from a band structure calculation, including the uncertainty in the scattering lengths. The uncertainty in the measured separation is indicated by the size of the points. (**B**) Location of resonances for all MI phases relative to the $n = 1$ phase for $V = 25E_{rec}$ and $V = 35E_{rec}$. For low site occupation (n values from 1 to 3), the separation between the resonances is roughly constant, implying constant U. For $V = 35E_{rec}$, the separation between the $n = 4$ and $n = 5$ peaks was 22(2) Hz, a 27% decrease from the 30(1) Hz separation between the $n = 1$ and $n = 2$ peaks. The slope of the lines is fit to the separation between the $n = 1$ and $n = 2$ peaks.

the resonance frequencies for the n and $n - 1$ MI phases is given by

$$\delta\nu = \frac{U}{h}(a_{21} - a_{11})/a_{11} \qquad (7)$$

The linewidth of the resonances is no longer broadened by the inhomogeneous density and should be limited only by the bandwidth of the two-photon pulse.

The resonance transitioned from a broadened line to several sharp lines as the lattice depth was increased (Fig. 1). At a lattice depth of $V = 5E_{rec}$, the line was broadened and the line center was shifted slightly because of the increased density. At $V = 10E_{rec}$, the line was shifted and broadened further, and in addition the line shape became asymmetric as the atom number in lattice sites with small occupation was squeezed. For deeper lattice depths, the system underwent a phase transition to a MI phase, and discrete peaks appeared, corresponding to MI phases with different filling factors; for $V = 35E_{rec}$, MI phases with occupancies of up to five were observed.

When the lattice depth was increased inside the MI regime (from $V = 25E_{rec}$ to $V = 35E_{rec}$), the separation between the resonance peaks increased, presumably because of the larger onsite interaction energy as the lattice trap was increased. As given in Eq. 7, the separation between the peaks provides a direct measurement of the onsite interaction energy, U. Our results are in good agreement with calculated values of U (Fig. 2A). Although the separation between the $n = 1$, $n = 2$, and $n = 3$ peaks is roughly constant, for higher filling factors the separation between the peaks decreases; the effective onsite interaction energy becomes smaller for higher filling factors (Fig. 2B). This result shows that for low occupation numbers the atoms occupy the ground state wave function of the lattice site, whereas for larger occupation numbers, the repulsive onsite interaction causes the wave function to spread out, lowering the interaction energy. From a variational calculation of the wave function similar to (*17*), we find that the onsite energy for the $n = 5$ shell should be ~20% smaller than that for the $n = 1$ shell, in agreement with the measured value (Fig. 2B).

The peaks for the different occupation numbers were spectrally well separated. Therefore, on resonance, only atoms from a single shell were transferred to the $|2, 1\rangle$ state. An image of these atoms (without any time of flight) shows the spatial distribution of this shell. Figure 3B shows absorption images for $n = 1$ to $n = 5$ shells. As predicted (*1*), the $n = 1$ MI phase appears near the outer edge of the cloud. For larger n, the radius of the shell decreases, and the $n = 5$ sites form a core in the center of the cloud. The expected radius for each shell was obtained from Eq. 2 by using the measured values for the onsite interaction. The observed radii were in good agreement except for the $n = 1$ shell, which may have been affected by anharmonicities in the external trap. Absorption images taken with rf values between the peaks show a small signal, which may reflect the predicted thin superfluid layers between the insulating shells; however, this needs be studied further with improved signal-to-noise ratio. The expected absorption image of a shell should show a column density with a flat distribution in the center and raised edges. However, because of limitations (resolution and residual fringes) in our imaging system, these edges were not resolved.

Because we were able to address the different MI phases separately, we could determine the lifetime for each shell. For this, the atoms were first held in the lattice for a variable time τ before applying the 100-ms two-photon pulse. For the $n = 1$ MI phase and ignoring technical noise, the lifetime should only be limited by spontaneous scattering from the lattice beams. Even for the deepest lattices, the spontaneous scattering rate is less than 10^{-2} Hz. For the $n = 2$ MI phase, the lifetime is limited by dipolar relaxation, which for ^{87}Rb is slow, with a rate $< 10^{-2}$ Hz. For sites with $n \geq 3$, the lifetime is limited by three-body recombination with a rate equal to $\gamma n(n - 1)(n - 2)$ (*18*), with $\gamma = 0.026$ Hz for our parameters. This gives three-body lifetimes of τ_{3B} of 6.2 s, 1.6 s, and 0.6 s for the $n = 3$, $n = 4$, and $n = 5$ MI phases, respectively. This calculation of γ assumes for the density distribution the ground state of the harmonic oscillator potential, so for higher filling factors the actual lifetime could be higher. We

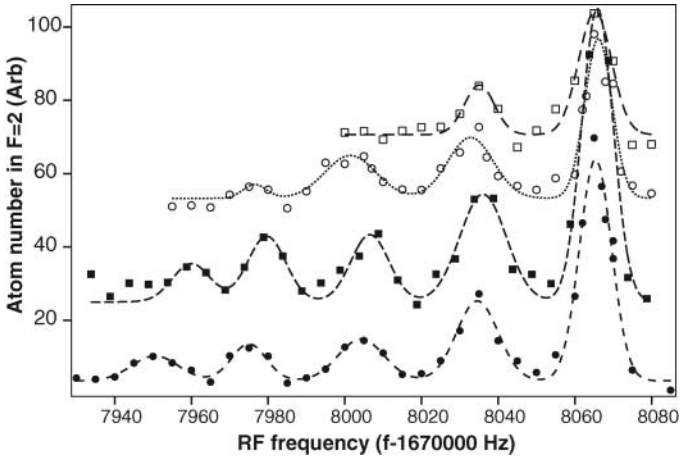

Fig. 4. Lifetime of individual MI shells. The lifetime for each MI phase can be measured independently by adding a hold time before applying the two-photon pulse. Spectra are shown for hold times of 0 ms (solid circles), 100 ms (solid squares), 400 ms (open circles), and 2000 ms (open squares). The lattice depth was $V = 35E_{rec}$ except for the 100-ms hold time, for which it was $V = 34E_{rec}$. The lines show Gaussian fits to the peaks, and the spectra were offset for clarity.

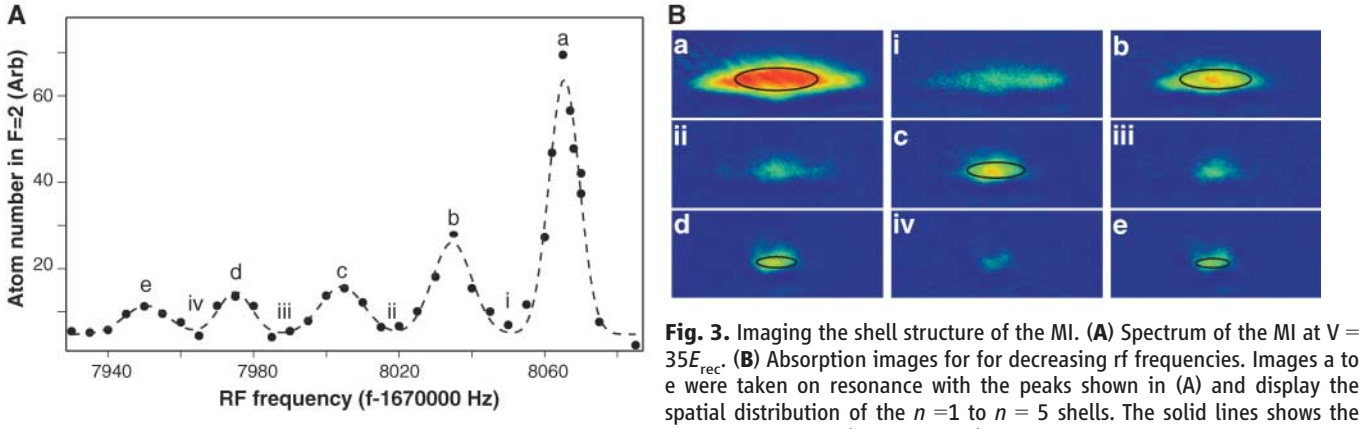

Fig. 3. Imaging the shell structure of the MI. (**A**) Spectrum of the MI at $V = 35E_{rec}$. (**B**) Absorption images for for decreasing rf frequencies. Images a to e were taken on resonance with the peaks shown in (A) and display the spatial distribution of the $n = 1$ to $n = 5$ shells. The solid lines shows the predicted contours of the shells. Absorption images taken for rf frequencies between the peaks (images i to iv) show a much smaller signal. The field of view was 185 μm by 80 μm.

show relative populations as a function of the hold time and derive lifetimes as τ almost equal to 1 s, 0.5 s, and 0.2 s for the $n = 3$, $n = 4$, and $n = 5$ MI phases, respectively (Fig. 4); this is shorter than predicted, which is possibly due to secondary collisions. For $n = 1$ and $n = 2$, lifetimes of over 5 s were observed.

We expect that this method can be used to measure the number statistics as the system undergoes the phase transition. One would expect that the spectral peaks for higher occupation number become pronounced only at higher lattice depth; an indication of this can be seen already in Fig. 1. For low lattice depths, the tunneling rate is still high, but one can suddenly increase the lattice depth and freeze in populations (*19*), which can then be probed with high-resolution spectroscopy. Fluctuations in the atom number could identify the superfluid layers between the Mott shells. In addition, by applying a magnetic gradient across the lattice, tomographic slices could be selected, combining full 3D resolution with spectral resolution of the site occupancy. These techniques may address questions about local properties that have been raised in recent theoretical simulations (*20*). The addressability of individual shells could be used to create systems with only selected occupation numbers (e.g., by removing atoms in other shells). Such a preparation could be important for the implementation of quantum gates, for which homogenous filling is desirable. For atoms other than rubidium, atomic clock shifts are much larger, e.g., for sodium, larger by a factor of 30. Therefore, it should be easier to resolve the MI shells, unless the collisional lifetime of the upper state of the clock transition sets a severe limit to the pulse duration.

Note added in proof: After submission of this work, the vertical profile of an $n = 2$ MI shell was obtained by using spin-changing collisions and a magnetic resonance imaging technique (*21*).

References and Notes

1. D. Jaksch, C. Bruder, J. I. Cirac, C. W. Gardiner, P. Zoller, *Phys. Rev. Lett.* **81**, 3108 (1998).
2. G. G. Batrouni *et al.*, *Phys. Rev. Lett.* **89**, 117203 (2002).
3. B. Marco, C. Lannert, S. Vishveshwara, T. C. Wei, *Phys. Rev. A.* **71**, 063601 (2005).
4. M. Greiner, O. Mandel, T. Esslinger, T. W. Hänsch, I. Bloch, *Nature* **415**, 39 (2002).
5. I. Bloch, *Nature Phys.* **1**, 23 (2005).
6. T. Stöferle, H. Moritz, C. Schori, M. Köhl, T. Esslinger, *Phys. Rev. Lett.* **92**, 130403 (2004).
7. S. Fölling *et al.*, *Nature* **434**, 481 (2005).
8. T. Volz *et al.*, published online 8 May 2006 (http://arxiv.org/abs/cond-mat?papernum=0605184).
9. F. Gerbier, S. Fölling, A. Widera, O. Mandel, I. Bloch, *Phys. Rev. Lett.* **96**, 090401 (2006).
10. M. P. A. Fisher, P. B. Weichman, G. Grinstein, D. S. Fisher, *Phys. Rev. B* **40**, 546 (1989).
11. D. M. Harber, H. J. Lewandowski, J. M. McGuirk, E. A. Cornell, *Phys. Rev. A.* **66**, 053616 (2002).
12. K. Gibble, S. Chu, *Phys. Rev. Lett.* **70**, 1771 (1993).
13. C. Fertig, K. Gibble, *Phys. Rev. Lett.* **85**, 1622 (2000).
14. Y. Sortais *et al.*, *Phys. Scr.* **T95**, 50 (2001).
15. J. Stenger *et al.*, *Phys. Rev. Lett.* **82**, 4569 (1999).
16. E. G. M. van Kempen, S. J. J. M. F. Kokkelmans, D. J. Heinzen, B. J. Verhaar, *Phys. Rev. Lett.* **88**, 093201 (2002).
17. G. Baym, C. J. Pethick, *Phys. Rev. Lett.* **76**, 6 (1996).
18. M. W. Jack, M. Yamashita, *Phys. Rev. A* **67**, 033605 (2005).
19. M. Greiner, O. Mandel, T. W. Hänsch, I. Bloch, *Nature* **419**, 51 (2002).
20. O. Gygi, H. G. Katzgraber, M. Troyer, S. Wessel, G. G. Batrouni, *Phys. Rev. A.* **73**, 063606 (2006).
21. S. Fölling, A. Widera, T. Mueller, F. Gerbier, I. Bloch, published online 23 June 2006 (http://arxiv.org/abs/cond-mat?papernum=0606592).

22. The authors thank I. Bloch and S. Fölling for insightful discussions. This work was supported by NSF. L.G.M. also acknowledges support from Fundação de Apoio a Pesquisa do Estrado de São Paulo.

23 May 2006; accepted 7 July 2006
10.1126/science.1130365

Evidence for a Past High-Eccentricity Lunar Orbit

Ian Garrick-Bethell,* Jack Wisdom, Maria T. Zuber

The large differences between the Moon's three principal moments of inertia have been a mystery since Laplace considered them in 1799. Here we present calculations that show how past high-eccentricity orbits can account for the moment differences, represented by the low-order lunar gravity field and libration parameters. One of our solutions is that the Moon may have once been in a 3:2 resonance of orbit period to spin period, similar to Mercury's present state. The possibility of past high-eccentricity orbits suggests a rich dynamical history and may influence our understanding of the early thermal evolution of the Moon.

The Moon is generally thought to have accreted close to the Earth and migrated outwards in a synchronously locked low-eccentricity orbit. During the early part of this migration, the Moon was cooling and continually subjected to tidal and rotational stretching. The principal moments of inertia $A < B < C$ of any satellite are altered in a predictable way by deformation due to spin and tidal attraction. The moments are typically characterized by ratios that are easier to measure, namely, the libration parameters $\beta = (C - A)/B$ and $\gamma = (B - A)/C$, and the degree-2 spherical-harmonic gravity coefficients $C_{20} = (2C - B - A)/(2Mr^2)$ and $C_{22} = (B - A)/(4Mr^2)$, where M and r are the satellite mass and radius. Of these four values β, γ, and C_{20} can be taken as independent. Using the ratio $(C - A)/A$, Laplace was the first to observe that the lunar moments are not in equilibrium with the Moon's current orbital state (*1*). He did not, however, address the possibility of a "fossil bulge," or the frozen remnant of a state when the Moon was closer to the Earth. Sedgwick examined the lunar moments in 1898, as did Jeffreys in 1915 and 1937, and both authors effectively showed that β is too large for the current orbit, suggesting that the Moon may carry a fossil bulge (*2*–*5*). However, Jeffreys showed that the fossil hypothesis might be untenable because the ratio of $\gamma/\beta = 0.36$ does not match the predicted ratio of 0.75 for a circular synchronous orbit (equivalently, $C_{20}/C_{22} = 9.1$, instead of the predicted ratio of 3.33). Indeed, using data from (*6*), none of the three independent measures of moments represent a low-eccentricity synchronous-orbit hydrostatic form; $C_{20} = 2.034 \times 10^{-4}$ is 22 times too large for the current state, and $\beta = 6.315 \times 10^{-4}$ and $\gamma = 2.279 \times 10^{-4}$ are 17 and 8 times too large, respectively (*7*, *8*).

The inappropriate ratio of γ/β or C_{20}/C_{22} has led some to dismiss the fossil bulge hypothesis as noise due to random density anomalies (*9*, *10*). However, the power of the second-degree harmonic gravity field is anomalously high when compared to the power expected from back extrapolating the power of higher harmonics (*7*, *11*). This suggests that the bulge may be interpreted as a signal of some process. Degree-2 mantle convection has been proposed as a means of deforming the Moon (*12*, *13*), but the dissimilarity of all three principal moments violates the symmetry of any simple degree-2 convection model (*12*). The Moon's center-of-mass/center-of-figure offset influences the moment parameters slightly, but that problem is geophysically separate and mathematically insignificant to the degree-2 problem (*8*, *14*).

Because C_{20} is due primarily to rotational flattening, and C_{22} is due to tidal stretching, the high C_{20}/C_{22} ratio seems to imply that the Moon froze in its moments while rotating faster than synchronous. However, in such cases no constant face would be presented to the Earth for any C_{22} power to form in a unique lunar axis. This apparent dilemma can be avoided by considering that in any eccentric orbit with an orbit period to spin period ratio given by n:2, with $n = 2, 3, 4, \ldots$, the passage through pericenter results in higher C_{22} stresses throughout a single elongated axis (hereafter called the pericenter axis). When the stresses experienced over one orbit period are time-averaged, the highest stresses

Department of Earth, Atmospheric and Planetary Sciences, Massachusetts Institute of Technology, 77 Massachusetts Avenue, Cambridge, MA 02139, USA.

*To whom correspondence should be addressed. E-mail: iang@mit.edu

Appendix D

Raman amplification of Matter Waves

This appendix contains a reprint of Ref. [99]: D. Schneble, G.K. Campbell, E.W. Streed, M. Boyd, D.E. Pritchard, and W. Ketterle, *Raman amplification of matter waves*, Phys. Rev. A **69**, 041601(R) (2004).

PHYSICAL REVIEW A **69**, 041601(R) (2004)

Raman amplification of matter waves

Dominik Schneble,* Gretchen K. Campbell, Erik W. Streed, Micah Boyd, David E. Pritchard, and Wolfgang Ketterle
MIT-Harvard Center for Ultracold Atoms, Research Laboratory of Electronics and Department of Physics, Massachusetts Institute of Technology, Cambridge, Massachusetts 02139, USA
(Received 6 November 2003; published 14 April 2004)

We demonstrate a Raman amplifier for matter waves, where the amplified atoms and the gain medium are in two different hyperfine states. This amplifier is based on a form of superradiance that arises from self-stimulated Raman scattering in a Bose-Einstein condensate.

DOI: 10.1103/PhysRevA.69.041601 PACS number(s): 03.75.−b, 42.50.Ct, 42.50.Gy

With the realization of coherent, laserlike atoms in the form of Bose-Einstein condensates it has become possible to explore matter-wave amplification, a process in which the number of atoms in a quantum state is amplified due to bosonic stimulation. Stimulation has been observed in the formation of condensates [1,2] and, more directly, has been used to realize coherent matter-wave amplifiers [3,4] based on superradiant Rayleigh scattering [5–13] in which the atomic momentum of the gain medium and the amplified atoms differ by a photon recoil. In these cases the atoms remained in the same internal state, a fact that severely limited the performance of superradiant atom amplifiers since the amplified atoms were scattered out of the final state or served as a gain medium for higher-order processes (superradiant cascades [7]).

In this Rapid Communication we demonstrate a Raman atom amplifier in which the gain medium and the amplified atoms are in different internal states. Such a system has analogies to an optical laser in which different transitions are used for pumping and lasing, thus circumventing the above limitations. The gain mechanism for this amplifier is stimulated Raman scattering in a Λ-type atomic level structure which occurs in a superradiant way. This system also acts as a Stokes Raman laser for optical radiation.

The amplification scheme is similar to that explored in previous work on Rayleigh superradiance in Bose-Einstein condensates [7,12] [cf. Fig. 1(a)]. A linearly polarized laser beam with wave vector $\mathbf{k}$ is incident on a magnetically trapped, cigar-shaped condensate, perpendicular to its long axis. Each scattering event creates a scattered photon with momentum $\hbar(\mathbf{k}-\mathbf{q})$ and a recoiling atom with corresponding momentum $\hbar\mathbf{q}$. This scattering process is bosonically stimulated by atoms that are already present in the final state $\hbar\mathbf{q}$.

For Rayleigh scattering, the mode with the highest gain is the so-called endfire mode, in which the scattered photons propagate along the long axis of the condensate, while the scattered atoms recoil at an angle of 45° [7]. Rayleigh superradiance is strongest when the electric-field vector of the incident beam is perpendicular to the long axis of the condensate and is suppressed when the field vector is parallel to it [7]. This parallel configuration is the experimental situation considered in this Rapid Communication.

*Electronic address: schneble@mit.edu

The angular distribution of spontaneously emitted light is dependent on its polarization. If we take the quantization axis $\hat{z}$ along the long axis of the condensate (which is also the direction of the bias field in the magnetic trap), the incident beam is π polarized. If the emitted light is also π polarized (Rayleigh scattering) its angular distribution is that of an oscillating dipole, $f_\pi(\theta)=(3/8\pi)\sin^2\theta$, where θ is the angle between $\hat{z}$ and the direction of propagation of the scattered light. The suppression of Rayleigh superradiance in this configuration is reflected in the fact that f_π vanishes along $\hat{z}$, such that the endfire mode cannot be populated. If the emitted light is σ polarized, the angular characteristics are those of a rotating dipole, $f_\sigma(\theta)=(3/16\pi)(1+\cos^2\theta)$ and emission into the endfire mode is favored. The absorption of π light followed by the emission of σ light corresponds to a Raman transition in which the z component of the atomic angular momentum changes by $\hbar$.

We now discuss the existence of superradiant gain for such a Raman process. For Rayleigh scattering an expression has been derived both semiclassically and quantum mechanically, using descriptions based on either atomic or optical stimulation [7,12,14]:

$$\dot{N}_q = N_0\,\Gamma_{sc} f(\theta)\Omega_q(N_q+1) \equiv G(N_q+1). \qquad (1)$$

Here, $N_0(N_q)$ is the number of atoms in the condensate (recoil mode), Γ_{sc} is the rate for spontaneous Rayleigh scatter-

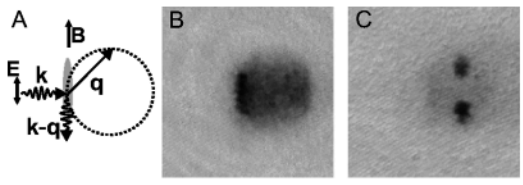

FIG. 1. Observation of superradiant Rayleigh scattering. (a) Experimental configuration. A laser beam (wave vector $\mathbf{k}$) is incident perpendicularly to the long axis of the condensate; its electric-field vector $\mathbf{E}$ is parallel to it and the applied magnetic field $\mathbf{B}$. Each scattering event results in a recoiling atom (momentum $\hbar\mathbf{q}$) and a scattered photon [momentum $\hbar(\mathbf{k}-\mathbf{q})$]. The recoiling atoms lie on a shell of radius $\hbar k$. (b) Spontaneous Rayleigh scattering. The absorption image shows a halo of atoms. The intensity of the beam was 1.0 mW/cm^2; the pulse duration was 1 ms. (c) Superradiant Raman scattering as observed for a beam intensity of 18 mW/cm^2 and a pulse duration of 100 μs (the original condensate was fully depleted after $\sim$10 μs. In both cases the field of view was 1.05 $\times$ 1.05 mm^2.

ing (which is proportional to the beam intensity I), $f(\theta) = f_\pi(\theta)$ is the angular distribution of the spontaneously emitted light, and $\Omega_q \sim \lambda^2/A$ is the phase-matching solid angle for superradiance in an extended sample, where λ is the wavelength of the scattered light and A is the cross-sectional area perpendicular to $\hat{z}$. It is straightforward to generalize Eq. (1) to the case of Raman scattering by interpreting Γ_{sc} as the rate for spontaneous Raman scattering and replacing $f(\theta) = f_\sigma(\theta)$. The transition from spontaneous to superradiant (Rayleigh or Raman) scattering occurs when the gain exceeds the losses (see below), or $N_q > 1$. The angular distribution is then no longer the familiar dipole pattern $f(\theta)$, but becomes highly directional.

To demonstrate superradiant Raman scattering experimentally, a cigar-shaped ^{87}Rb condensate was produced in a cloverleaf-type Ioffe-Pritchard magnetic trap with the procedure described in Ref. [12]. The condensate contained $N_0 = 10 \times 10^6$ atoms in the state $|1\rangle \equiv |5^2S_{1/2}, F=1, m_F=-1\rangle$, where F and m_F are the quantum numbers for the total spin and its $\hat{z}$ component, and had Thomas-Fermi radii of 165 μm and 13.3 μm in the axial and radial directions, respectively. The trapped condensate was illuminated with a horizontal π polarized laser beam for a variable duration τ, and the magnetic trap was switched off immediately afterwards. The beam had a detuning of $\Delta/(2\pi) = -340$ MHz from the $5^2S_{1/2}, F=1 \rightarrow 5^2P_{3/2}, F=1$ transition at $\lambda = 780$ nm. The atomic momentum distribution was analyzed by imaging the atomic ensemble after 32 ms of ballistic expansion. Absorption images were obtained with a vertical probe beam after the atoms had been optically pumped to the state $5^2S_{1/2}, F=2$.

Results obtained for light scattering in this situation are shown in Figs. 1(b) and 1(c). For laser beam intensities I of up to $I \sim 1$ mW/cm^2, a scattering halo consistent with a dipolar emission pattern was visible in the absorption images [cf. Fig. 1(b)], in agreement with earlier results [7] (for comparison, the threshold for Rayleigh superradiance was below $I = 100$ μW/cm^2 when the beam was polarized perpendicular to the long axis). However, when the intensity of the beam was increased to much larger values, the scattering became highly directional and two distinct peaks of recoiling atoms appeared into which the condensate was rapidly transferred [Fig. 1(c)]. In contrast to the appearance of a fan pattern observed in Rayleigh superradiance due to higher-order scattering [7], the atoms remained localized in these two peaks, even when the light was left on. A Stern-Gerlach-type analysis using ballistic expansion in a magnetic-field gradient revealed that the atoms in the recoiling peaks had been transferred to the upper hyperfine state $|2\rangle \equiv |5^2S_{1/2}, F=2, m_F=-2\rangle$, corresponding to the emission of σ^+ polarized light, Stokes-shifted by -6.8 GHz from the incident beam. Due to the change in the internal state the recoiling atoms were $\sim$6.5 GHz out of resonance with the pump laser light, which explains the suppression of higher-order scattering. Previous experiments with sodium [7] used a large detuning which coincided with the ground-state hyperfine splitting; thus the Raman scattered atoms were in resonance with the pump light. It is most likely for this reason that superradiant Raman scattering has not been observed before.

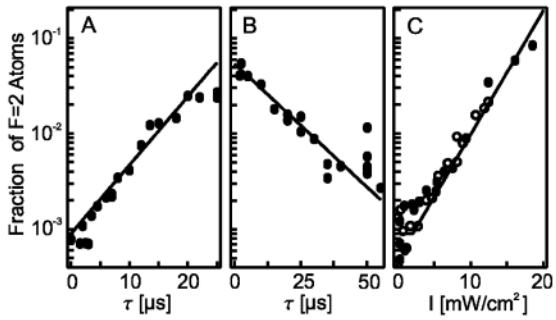

FIG. 2. Characterization of superradiant Raman scattering. The number of atoms in a single recoil peak is shown for three different situations. (a) Dependence on the pulse duration τ, with constant beam intensity ($I = 7.6$ mW/cm^2). The solid line describes an exponential growth according to Eq. (2) with $G - L = (1.7 \pm 0.1) \times 10^5$ s^{-1}. (b): Dependence on τ for a constant gain $G(I\tau = 140$ mW/cm^2 μs). The atom number decays exponentially with the rate $L = (6.2 \pm 0.5) \times 10^4$ s^{-1} (solid line). (c) Dependence on the laser intensity for a constant pulse duration ($\tau = 10$ μs). The solid line is calculated from Eq. (2) with parameters L and $G/I = 3.0 \times 10^4$ cm^2/mW s as obtained in a and b, predicting a threshold at 2.1 mW/cm^2. The open circles represent the measurement of Fig. 4, rescaled for the intensity of the electric-field component along the long axis of the condensate.

The time evolution of the number N_q of atoms in the recoil peaks in the perturbative regime $N_q \ll N_0$ (cf. Fig. 2) showed exponential growth as predicted by Eq. (1). In the presence of a loss mechanism with a rate L, the rate equation for $N_q \gg 1$ is modified to

$$\dot{N}_q = (G - L) N_q. \tag{2}$$

To determine L, the condensate was illuminated with the beam for variable pulse durations τ while keeping the pulse area $I\tau \propto G\tau$ constant. In this case the number of recoiling Raman-scattered atoms should scale as $N_q(\tau) \propto \exp(-L\tau)$. The experimental result, shown in Fig. 2(b), shows an exponential decay with a rate constant $L = 1/(16$ μs).

The loss rate L observed here is a factor of 25 faster than the corresponding rate for superradiant Rayleigh scattering (i.e., the width of the two-photon Bragg resonance [7,15]). To explain this difference we first note that, as in superradiant Rayleigh scattering, the term $N_0 N_q$ in Eq. (1) describes an interference between the initial and final atomic states. This interference pattern constitutes a dynamic grating that diffracts the pump light into the endfire mode. As in the Rayleigh case, losses will occur when the overlap between the recoiling atoms and the condensate decreases. However, for Raman superradiance there is an important difference. The internal states are orthogonal, and therefore the spatial modulation is not in the atomic density but rather in the coherences (off-diagonal elements of the density matrix) [16] between the atomic states. Atomic coherences between different hyperfine states are sensitive to magnetic fields, leading to additional loses. In our case, there is a difference in the Zeeman shifts of states $|1\rangle (m_F g_F = 1/2)$ and $|2\rangle (m_F g_F = -1)$. In an inhomogeneous magnetic field the coherences

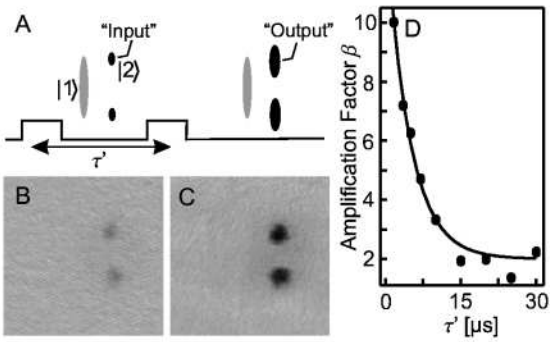

FIG. 3. (a) Realization of a Raman amplifier for matter waves. The first laser pulse prepares a cloud of N_q recoiling atoms in state $|2\rangle$ (input). After a wait time τ', these atoms are amplified by a second, identical pulse to a number $N_q'=\beta N_q$ (output), where β is the amplification factor. (b) and (c) Input and output ($\beta=6$) for a pulse duration $\tau=1.65$ μs and a wait time $\tau'=5$ μs. The intensity of the laser beam was 60 mW/cm^2. The absorption images were taken without optical pumping from $|1\rangle$ to $|2\rangle$ and therefore do not show the condensate in the center of the field of view. (d) Dependence of the amplification factor β on the wait time τ'. The line represents an exponential decay with a decay rate of $(2.2\pm0.2)\times10^5$ s^{-1}.

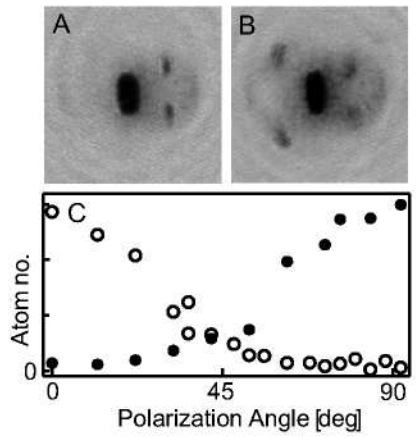

FIG. 4. Tuning between superradiant modes. (a) Raman superradiance (b) Rayleigh superradiance (Kapitza-Dirac regime) for polarization parallel and orthogonal to the condensate axis, respectively. (c) Variation of the atom number in the Raman peaks (open circles) and in the Rayleigh backward peaks (filled circles) with the polarization angle. The angle had a systematic uncertainty of $\sim10°$ from the orientation of the condensate with respect to the axis of the magnetic trap. The measurements were done for a laser intensity of 12 mW/cm^2 and a pulse duration of 10 μs.

evolve at locally varying frequencies, resulting in dephasing and thus in a decay of the grating. In a magnetic trap, the gravitational force is balanced by a magnetic-field gradient. For the parameters of our trap, the variation of the magnetic field is 10 mG within the condensate, corresponding to an inhomogeneous broadening of the splitting between $|1\rangle$ and $|2\rangle$ of 2×10^5 s^{-1}. This simple estimate for L agrees with the measured value to within a factor of 3.

The fast loss mechanism can also be explained by considering the population of the recoil state $\hbar\mathbf{q}$. In contrast to the atoms in the condensate the recoiling atoms are accelerated in the magnetic-field gradient. After the dephasing time L^{-1} their momentum has changed by $\hbar/d$, where d is the vertical size of the condensate. This momentum transfer is comparable to the momentum uncertainty associated with d and leads to a state distinct from the recoil state. This population loss in $\hbar\mathbf{q}$ could be decreased by avoiding magnetic-field gradients, e.g., in an optical trap or by using free falling condensates.

The dependence of the atom number in the recoil peaks on the intensity of the laser beam is shown in Fig. 2(c). The atom number increased exponentially according to $N_q(\tau)\propto\exp(G-L)\tau$ above threshold, with parameters that are consistent with those found in the measurements shown in Figs. 2(a) and 2(b). The experimentally determined gain G agrees with the value predicted by Eq. (1) ($G_{th}=1\times10^6$ s^{-1} for a beam intensity of 7.6 mW/cm^2 [17]) to within a factor of 4.

Raman superradiance can be considered as amplification of the first, spontaneous scattering event into the endfire mode. However, if a coherent input is applied to the system this input will get amplified as well. In analogy to the work on Rayleigh scattering [3,4] we have used superradiant Raman scattering as a mechanism for the amplification of matter waves, as illustrated in Fig. 3. To prepare the input, a short laser pulse was first applied to the trapped condensate, preparing a small cloud of N_q recoiling atoms in state $|2\rangle$. A second, identical pulse was then applied after a wait time τ'. This led to a significant increase of the atom number to an output value $N_q'=\beta N_q$, where β is the amplification factor. Values up to $\beta=10$ were observed (Fig. 3), which is a clear signature for Raman amplification in state $|2\rangle$.

In agreement with the loss mechanism discussed above, the matter-wave amplification factor β was found to depend on the wait time τ' between the pulses. During this time, the input atoms were accelerated out of the narrow bandwidth of the amplifying pulse. The observed amplification factor [cf., Fig. 3(d)] decayed with a rate of 2.2×10^6 s^{-1} to a value of $\beta=2$ in which case the number of atoms in the output was simply the sum of two independent superradiant pulses. This decay rate is in good agreement with the estimate for L given above and agrees with the result of Fig. 2(b) to within a factor of 3.5. Both rates should agree according to Eq. (2), but we note that our simple model does not account for the depletion of the condensate and optical propagation effects (note that for the measurement shown in Fig. 2(b) the pump light was on, while it was off between the two pulses).

Superradiant Rayleigh and Raman scattering can be regarded as two modes of an atom laser. Just as in a multimode optical laser one mode can be selected by introducing mode-selective elements, the relative gain of the two matter-wave modes can be controlled by the polarization of the incident light, as is shown in Fig. 4. When the polarization was rotated from parallel to the long axis of the condensate to perpendicular, the three-peaked Raman pattern of recoiling atoms (a) changed into the X-shaped pattern (b) characteristic for the Kapitza-Dirac regime of superradiant Rayleigh scattering [12,13]. The polarization angle dependence is shown in Fig. 4(c). The transition was almost symmetric about an angle of 45°, around which both types of superradiance were active. Note, however, that this symmetry is not universal but depends on the particular choice of parameters. The thresh-

olds (loss rates) for the two kinds of superradiance differ by a factor of 25, and the transition matrix element for Raman scattering is 6.5 times smaller than that for Rayleigh scattering at our detuning. The fact that the superradiant rates at the optimum angles were almost the same is due to the fact that at short pulses, the superradiant Rayleigh gain is suppressed due to the presence of backward peaks [12]. In the present case, which is far above threshold and near the end of the short-pulse regime [12], this effect resulted in a gain suppression by a factor ~6.5 for Rayleigh superradiance.

The Raman transition from $|1\rangle$ to $|2\rangle$ involves the absorption of π light and emission of σ^+ light. One can therefore regard the angular dependence of superradiant Raman scattering as a dependence on the intensity of the π component of the incident light, which scales as $\cos^2\alpha$, where α is the angle between the electric-field vector and the axis. Indeed, the rescaled data of Fig. 4 nicely matches the other data shown in Fig. 2(c) for which the total intensity of the light was varied.

The comparison of these two amplification modes also illustrates that the observed Raman superradiance does not have a short-pulse (or Kapitza-Dirac) regime, unlike the Rayleigh process for which endfire mode photons are scattered back into the laser beam [12]. This process violates energy conservation by the recoil frequency and therefore can happen only at times shorter or comparable to the inverse recoil frequency. For the observed Raman scattering, the energy mismatch (divided by h) is ~6.5 GHz, corresponding to subnanosecond time scales on which backscattering might happen. Similarly, the absence of higher-order forward peaks reflects the fact that the laser light is too far out of resonance with the atoms in the recoil state to drive further Raman transitions (e.g., back to $F=1$) on the experimental time scale.

Finally, we mention that superradiant Raman scattering is also possible between sublevels of the same hyperfine state. For a detuning of $\Delta/(2\pi)=-140$ MHz, the transition matrix elements for Raman transitions to $5^2S_{1/2}, F=2, m_F=-2$ and to $5^2S_{1/2}, F=1, m_F=0$ are almost the same. Indeed we observed strong Raman superradiance with a $F=1, m_F=0$ first-order peak and a $F=1, m_F=1$ second-order peak (this was observed also for -340 MHz detuning, but was much less pronounced). Further peaks (orders higher than 2 or backward peaks) were not observed. For longer pulse length, the $F=1$ peaks disappeared, unlike the $F=2$ peaks, since subsequent spontaneous Rayleigh scattering is much stronger for $F=1$ atoms due to the much smaller detuning.

In conclusion, we have studied a new phenomenon in the interaction of a Bose-Einstein condensate with a single strong laser beam. The cloud can spontaneously create not only density gratings [7] and phase gratings [12], but also periodic modulations of coherences. Whereas an atomic density grating is accompanied by a standing light wave formed by the pump light and the endfire mode, the coherence grating is driven by an optical field with a polarization grating formed by two beams of orthogonal polarization. The exponential growth of coherence gratings provides a mechanism to amplify matter waves in an internal state different from the one of the amplifying medium. In principle, all these superradiant phenomena could also be observed in noncondensed clouds, but lower density and Doppler broadening lead to much higher thresholds in the laser power.

We would like to thank J. M. Vogels and J. Steinhauer for fruitful discussions, and A. E. Leanhardt for a critical reading of the manuscript. We acknowledge financial support by NSF and the MIT-Harvard Center for Ultracold Atoms.

[1] H.-J. Miesner, D. M. Stamper-Kurn, M. R. Andrews, D. S. Durfee, S. Inouye, and W. Ketterle, Science **279**, 1005 (1998).

[2] M. Köhl, M. J. Davis, C. Gardiner, T. W. Hänsch, and T. Esslinger, Phys. Rev. Lett. **88**, 080402 (2002).

[3] S. Inouye, T. Pfau, S. Gupta, A. P. Chikkatur, A. Görlitz, D. E. Pritchard, and W. Ketterle, Nature (London) **402**, 641 (1999).

[4] M. Kozuma, Y. Suzuki, Y. Torii, T. Sugiura, T. Kuga, E. W. Hagley, and L. Deng, Science **286**, 2309 (1999).

[5] R. H. Dicke, Phys. Rev. **93**, 99 (1954).

[6] M. Gross and S. Haroche, Phys. Rep. **93**, 301 (1982).

[7] S. Inouye, A. P. Chikkatur, D. M. Stamper-Kurn, J. Stenger, D. E. Pritchard, and W. Ketterle, Science **285**, 571 (1999).

[8] M. G. Moore and P. Meystre, Phys. Rev. Lett. **83**, 5202 (1999).

[9] Ö. E. Müstecaplioglu and L. You, Phys. Rev. A **62**, 063615 (2000).

[10] N. Piovella, R. Bonifacio, B. W. J. McNeil, and G. R. M. Robb, Opt. Commun. **187**, 165 (2001).

[11] E. D. Trifonov, Zh. Eksp. Teor. Fiz. **120**, 1117 (2001) [JETP **93**, 969 (2001)].

[12] D. Schneble, Y. Torii, M. Boyd, E. Streed, D. E. Pritchard, and W. Ketterle, Science **300**, 475 (2003).

[13] H. Pu, W. Zhang, and P. Meystre, Phys. Rev. Lett. **91**, 150407 (2003).

[14] W. Ketterle and S. Inouye, in *Bose-Einstein Condensates and Atom Lasers*, edited by A. Aspect and J. Dalibard, C. R. Acad. Sci., Ser IV (Elsevier, Paris, 2001), pp. 339–380.

[15] J. Stenger, S. Inouye, A. P. Chikkatur, D. M. Stamper-Kurn, D. E. Pritchard, and W. Ketterle, Phys. Rev. Lett. **82**, 4569 (1999).

[16] A. Kumarakrishnan, S. B. Cahn, U. Shim, and T. Sleator, Phys. Rev. A **58**, R3387 (1998).

[17] The spontaneous Raman scattering rate was calculated as $\Gamma_{sc} \sim (\omega_R^2)/(4\Delta^2)\Gamma'$ for a Λ-type level structure, where $\omega_R = dE/\hbar$ is the Rabi frequency of the laser beam and $\Gamma' = 4\pi\omega d'^2/3\epsilon_0\hbar c\lambda^2$ is the rate for spontaneous decay from the intermediate state to the final state, resulting in a dependency $\Gamma_{sc} \propto (dd'/\Delta)^2$. In this expression d and d' are the dipole matrix elements for the Raman transition. The couplings to the various states i of the excited-state manifold were included by performing a coherent summation, $\Gamma_{sc} \propto (\Sigma d_i d_i'/\Delta_i)^2$.

Bibliography

[1] J. R. Abo-Shaeer, D. E. Miller, J. K. Chin, K. Xu, T. Mukaiyama, and W. Ketterle. Coherent molecular optics using ultracold sodium dimers. *Phys. Rev. Lett*, 94:040405, 2005.

[2] M. Abraham. *Rend.Pal*, 28:1, 1909.

[3] M. Abraham. *Rend.Pal*, 30:33, 1910.

[4] B. P. Anderson, P. C. Haljan, C. A. Regal, D. L. Feder, L. A. Collins, C. W. Clark, and E. A. Cornell. Watching dark solitons decay into vortex rings in a bose-einstein condensate. *Phys. Rev. Lett*, 86:2926, 2001.

[5] A. Ashkin. Acceleration and trapping of paricles by radiation pressure. *Phys. Rev. Lett*, 24:156, 1970.

[6] R. Battesti, P. Cladé, S. Guellati-Khèlifa, C. Schwob, B. Grémaud, F. Nez, L. Julien, and F. Biraben. Bloch oscillations of ultracold atoms: A tool for a metrological determination of h/m_{Rb}. *Phys. Rev. Lett.*, 92:253001, 2004.

[7] S. Bize, Y. Sortais, M. S. Santos, C. Mandache, A. Clairon, and C. Salomon. High accuracy measurement of the ^{87}rb ground state hyperfine splitting in an atomic fountain. *Europhys. Lett.*, 45:588, 1999.

[8] I. Bloch. Ultracold quantum gases in optical lattices. *Nature Physics*, 1:23, 2005.

[9] E. L. Bolda, E. Tiesinga, and P. S. Julienne. Effective-scattering-length model of ultracold atomic collisions and feshbach resonances in tight harmonic traps. *Phys. Rev. A*, 66:013403, 2002.

[10] S. Burger, K. Bongs, S. Dettmer, W. Ertmer, and K. Sengstock. Dark solitons in bose-einstein condensates. *Phys. Rev. Lett*, 83:5198, 1999.

[11] S. Burger, F. S. Cataliotti, C. Fort, F. Minardi, M. Inguscio, M. L. Chiofalo, and M. P. Tosi. Superfluid and dissipative dynamics of a bose-einstein condensate in a periodic optical potential. *Phys. Rev. Lett.*, 86:4447, 2001.

[12] G. K. Campbell, J. Mun, M. Boyd, P. Medleyand A. E. Leanhardt, L. G. Marcassa, D. E. Pritchard, and W. Ketterle. Imaging the mott insulator shells by using atomic clock shifts. *Science*, 313:649, 2006.

[13] G.K. Campbell, J. Mun, M. Boyd, E. W. Streed, W. Ketterle, and D. E. Pritchard. Parametric amplification of scattered atom pairs. *Phys. Rev. Lett.*, 96:020406, 2006.

[14] F.S. Cataliotti, L. Fallani, F. Ferlaino, C. Fort, P. Maddaloni, and M. Inguscio. Superfluid current disruption in a chain of weakly coupled Bose-Einstein condensates. *New Journal of Physics*, 5:71, 2003.

[15] A. P. Chikkatur. *Colliding and Moving Bose-Einstein Condensates: Studies of superfluidity and optical tweezers for condensate transport.* Ph.D. Thesis, Massachusetts Institute of Technology, 2002.

[16] J. K. Chin, D. E. Miller, Y. Liu, C. Stan, W. Setiawan, C. Sanner, K. Xu, and W. Ketterle. Superfluidity of Ultracold Fermions in an Optical Lattice. *Arxiv preprint cond-mat/0607004*, 2006.

[17] S. Chu, J. E. Bjorkholm, A. Ashkin, and A. Cable. Experimental observation of optically trapped atoms. *Phys. Rev. Lett*, 57:314, 1986.

[18] E. A. Cornell and C. E. Wieman. Nobel lecture: Bose-Einstein condensation in a dilute gas, the first 70 years and some recent experiments. *Rev. Mod. Phys.*, 74:875, 2002.

[19] M. Cristiani, O. Morsch, N. Malossi, M. Jona-Lasinio, M. Anderlini, E. Courtade, and E. Arimondo. Instabilities of a Bose-Einstein condensate in a periodic potential: an experimental investigation. *Optics Express*, 12:4, 2004.

[20] F. Dalfovo, S. Giorgini, L. P. Pitaevskii, and S. Stringari. Theory of Bose-Einstein condensation in trapped gases. *Rev. Mod. Phys.*, 71:463, 1998.

[21] S. R. de Groot and L. G. Suttorp. *Foundations of electrodynamics*. Noord-Hollandsche U.M., Amsterdam, 1972.

[22] B. DeMarco, C. Lannert, S. Vishveshwara, and T.-C. Wei. Structure and stability of mott-insulator shells of bosons trapped in an optical lattice. *Phys. Rev. A*, 71:063601, 2005.

[23] L. Deng, E. W. Hagley, J. Wen, M. Trippenbach, Y. Band, P. S. Julienne, J. E. Simsarian, K. Helmerson, S. L. Rolston, and W. D. Phillips. Four-wave mixing with matter waves. *Nature*, 398:218, 1999.

[24] J. Denschlag, J. E. Simsarian, D. L. Feder, Charles W. Clark, L. A. Collins, J. Cubizolles, L. Deng, E. W. Hagley, K. Helmerson, W. P. Reinhardt, S. L. Rolston, B. I. Schneider, and W. D. Phillips. Generating solitons by phase engineering of a bose-einstein condensate. *Science*, 287:97, 2000.

[25] J. H. Denschlag, J. E. Simsarian, H. Haeffner, C. McKenzie, A. Browaeys, D. Cho, K. Helmerson, S. L. Rolston, and W. D. Phillips. A Bose-Einstein condensate in an optical lattice. *Journal of Physics B Atomic Molecular and Optical Physics*, 35:3095, 2002.

[26] R.H. Dicke. Coherence in spontaneous radiation processes. *Physical Review*, 93:99, 1954.

[27] L.-M. Duan, A. Sørensen, J.I. Cirac, and P. Zoller. Squeezing and entanglement of atomic beams. *Phys. Rev. Lett*, 85:3991, 2000.

[28] M. Boyd et.al. A mott insulator atomic clock. *In preparation.*

[29] L. Fallani, JE Lye, V. Guarrera, C. Fort, and M. Inguscio. Onset of a Bose-Glass of ultracold atoms in a disordered crystal of light. *Arxiv preprint cond-mat/0603655*, 2006.

[30] L. Fallani, L. De Sarlo, J. E. Lye, M. Modugno, R. Saers, C. Fort, and M. Inguscio. Observation of dynamical instability for a bose-einstein condensate in a moving 1d optical lattice. *Phys. Rev. Lett*, 93:140406, 2004.

[31] C. Fertig and K. Gibble. Measurement and cancellation of the cold collision frequency shift in an ^{87}Rb fountain clock. *Phys. Rev. Lett.*, 85:1622, 2000.

[32] M. P. A. Fisher, P. B. Weichman, G. Grinstein, and D. S. Fisher. Boson localization and the superfluid-insulator transition. *Phys. Rev. B*, 40:546, 1989.

[33] S. Fölling, F. Gerbier, A. Widera, O. Mandel, T. Gericke, and I. Bloch. Spatial quantum noise interferometry in expanding ultracold atom clouds. *Nature*, 434:481, 2005.

[34] S. Fölling, A. Widera, T. Müller, F. Gerbier, and I. Bloch. Formation of spatial shell structure in the superfluid to mott insulator transition. *Phys. Rev. Lett.*, 97:060403, 2006.

[35] F. Gerbier, S. Fölling, A. Widera, O. Mandel, and I. Bloch. Spatial quantum noise interferometry in expanding ultracold atom clouds. *Phys. Rev. Lett.*, 96:090401, 2006.

[36] F. Gerbier, A. Widera, S. Fölling, O. Mandel, T. Gericke, and I. Bloch. Interference pattern and visibility of a mott insulator. *Phys. Rev. A*, 72:053606, 2005.

[37] F. Gerbier, A. Widera, S. Fölling, O. Mandel, T. Gericke, and I. Bloch. Phase coherence of an atomic mott insulator. *Phys. Rev. Lett.*, 95:050404, 2005.

[38] K. Gibble and S. Chu. Laser-cooled cs frequency standard and a measurement of the frequency shift due to ultracold collisions. *Phys. Rev. Lett.*, 70:1771, 1993.

[39] M. Girardeau. Relationship between Systems of Impenetrable Bosons and Fermions in One Dimension. *Journal of Mathematical Physics*, 1:516, 1960.

[40] J. P. Gordon. Radiation forces and momenta in dielectric media. *Phys. Rev. A*, 8:14, 1973.

[41] P. L. Gould, G. A. Ruff, and D. E. Pritchard. Diffraction of atoms by light: The near-resonant kapitza-dirac effect. *Phys. Rev. Lett.*, 56:827, 1986.

[42] M. Greiner. *Ultracold quantum gases in three-dimensional optical lattice potentials*. Ph.d., Ludwig-Maximilians-Universität München, 2003.

[43] M. Greiner, O. Mandel, T. Esslinger, T. W. Hänsch, and I. Bloch. Quantum phase transition from a superfluid to a mott insulator in a gas of ultracold atoms. *Nature*, 415:39, 2002.

[44] M. Greiner, O. Mandel, T.W. Hänsch, and I. Bloch. Collapse and revival of the matter wave field of a Bose-Einstein condensate. *Nature*, 419:51, 2002.

[45] S. Gupta, K. Dieckmann, Z. Hadzibabic, and D. E. Pritchard. Contrast interferometry using bose-einstein condensates to measure h/m and α. *Phys. Rev. Lett*, 89:140401, 2002.

[46] S. Gupta, A. E. Leanhardt, A. D. Cronin, and D. E. Pritchard. Coherent manipulation of atoms with standing light waves. *C.R. Acad. Sci. IV-Phys.*, 2:479, 2001.

[47] T. Gustavson, A. P. Chikkatur, A. Leanhardt, A. Görlitz, S. Gupta, D. E. Pritchard, and W. Ketterle. Transport of bose-einstein condensates with optical tweezers. *Phys. Rev. Lett*, 88:020401, 2002.

[48] D. M. Harber, H. J. Lewandowski, J. M. McGuirk, and E. A. Cornell. Effect of cold collisions on spin coherence and resonance shifts in a magnetically trapped ultracold gas. *Phys. Rev. A*, 66:053616, 2002.

[49] M. P. Haugan and F. V. Kowalski. Spectroscopy of atoms and molecules in gases: Corrections to the doppler-recoil shift. *Phys. Rev. A*, 25:2102, 1982.

[50] K. M. Hilligsøe and K. Mølmer. Phase-matched four wave mixing and quantum beam splitting of matter waves in a periodic potential. *Phys. Rev. A*, 71:041602, 2005.

[51] V. W. Hughes and T. Kinoshita. Anomalous g values of the electron and muon. *Rev. Mod. Phys*, 71:S133, 1999.

[52] S. Inouye, MR Andrews, J. Stenger, HJ Miesner, DM Stamper-Kurn, and W. Ketterle. Observation of Feshbach resonances in a Bose-Einstein condensate. *Nature*, 392:151, 1998.

[53] S. Inouye, A. P. Chikkatur, D. M. Stamper-Kurn, J. Stenger, D. E. Pritchard, and W. Ketterle. Superradiant Rayleigh Scattering from a Bose-Einstein Condensate. *Science*, 285:571, 1999.

[54] S. Inouye, A. P. Chikkatur, D.M Stamper-Kurn, D. E. Pritchard, and Ketterle W. Superradiant rayleigh scattering from a bose-einstein condensate. *Science*, 285:571, 1999.

[55] Shin Inouye. *Manipulating Bose-Einstein condensates with laser light.* Ph.d., Massachusetts Institute of Technology, 2001.

[56] Michael W. Jack and Makoto Yamashita. Signatures of the quantum fluctuations of cold atoms in an optical lattice in the three-body loss rate. *Phys. Rev. A*, 67:033605, 2003.

[57] D. Jaksch. *Bose-Einstein condensation and applications.* Ph.d., Leopold-Franzens-Univ., Innsbruck, 1999.

[58] D. Jaksch, C. Bruder, J. I. Cirac, C. W. Gardiner, and P. Zoller. Cold bosonic atoms in optical lattices. *Phys. Rev. Lett.*, 81:3108, 1998.

[59] D. Jaksch and P. Zoller. The cold atom Hubbard toolbox. *Annals of Physics*, 315:52, 2005.

[60] RV Jones and B. Leslie. The Measurement of Optical Radiation Pressure in Dispersive Media. *Proceedings of the Royal Society of London. Series A, Mathematical and Physical Sciences*, 360:347, 1978.

[61] RV Jones and JCS Richards. The Pressure of Radiation in a Refracting Medium. *Proceedings of the Royal Society of London. Series A, Mathematical and Physical Sciences*, 221:480, 1954.

[62] R. S. Van Dyck Jr., P. B. Schwinberg, and H. G. Dehmelt. New high-precision comparison of electron and positron g factors. *Phys. Rev. Lett*, 59:26, 1987.

[63] Campbell G. K., Leanhardt A. E., Mun J., Boyd M., E. W. Streed, Ketterle W., and Pritchard D. E. Photon recoil momentum in dispersive media. *Phys. Rev. Lett.*, 94:170403, 2005.

[64] W. Ketterle. Nobel lecture: When atoms behave as waves: Bose-Einstein condensation and the atom laser. *Rev. Mod. Phys.*, 74:1131, 2002.

[65] W. Ketterle, D. S. Durfee, and D. M. Stamper-Kurn. Making, probing and understanding Bose-Einstein condensates. In M. Inguscio, S. Stringari, and C. E. Wieman, editors, *Bose-Einstein Condensation in Atomic Gases*, page 67, Amsterdam, 1999. IOS Press.

[66] T. Kinoshita. New value of the α^3 electron anomalous magnetic moment. *Phys. Rev. Lett*, 75:4728, 1995.

[67] T. Kinoshita, T. Wenger, and D.S. Weiss. Observation of a One-Dimensional Tonks-Girardeau Gas. *Science*, 305:1125, 2004.

[68] M. Köhl, H. Moritz, T. Stöferle, K. Günter, and T. Esslinger. Fermionic Atoms in a Three Dimensional Optical Lattice: Observing Fermi Surfaces, Dynamics, and Interactions. *Phys. Rev. Lett.*, 94:080403, 2005.

[69] V. V. Konotop and M. Salerno. Modulational instability in bose-einstein condensates in optical lattices. *Phys. Rev. A*, 65:021602, 2002.

[70] M. Kozuma, L. Deng, E. W. Hagley, J. Wen, R. Lutwak, K. Helmerson, S. L. Rolston, and W. D. Phillips. Coherent splitting of bose-einstein condensed atoms with optically induced bragg diffraction. *Phys. Rev. Lett.*, 82:871, 1999.

[71] Y. Le Coq, J.A. Retter, S. Richard, A. Aspect, and P. Bouyer. Coherent matter wave inertial sensors for precision measurements in space. *Arxiv preprint cond-mat/0501520*, 2005.

[72] A. J. Leggett. Bose-Einstein condensation in the alkali gases: Some fundamental concepts. *Rev. Mod. Phys.*, 73:307, 2001.

[73] G. Lenz, P. Meystre, and E. M. Wright. Nonlinear atom optics. *Phys. Rev. Lett.*, 71:3271, 1993.

[74] P. D. Lett, K. Helmerson, W. D. Phillips, L. P. Ratliff, S. L. Rolston, and M. E. Wagshul. Spectroscopy of na_2 by photoassociation of laser-cooled na. *Phys. Rev. Lett*, 71:2200, 1993.

[75] M. Machholm, A. Nicolin, C. J. Pethick, and H. Smith. Spatial period doubling in bose-einstein condensates in an optical lattice. *Phys. Rev. A*, 69:043604, 2004.

[76] M. P. Marder. *Condensed Matter Physics*. Wiley Interscience, New York, 2000.

[77] P. J. Martin, B. G. Oldaker, A. H. Miklich, and D. E. Pritchard. Bragg scattering of atoms from a standing light wave. *Phys. Rev. Lett.*, 60:515, 1988.

[78] J. D. Miller, R. A. Cline, and D. J. Heinzen. Photoassociation spectrum of ultracold rb atoms. *Phys. Rev. Lett*, 71:2204, 1993.

[79] H. Minkowski. *Nachr. Ges. Wiss. Gottingen*, page 53, 1908.

[80] H. Minkowski. *Math. Ann*, 68:472, 1910.

[81] M. Modugno, C. Tozzo, and F. Dalfovo. Role of transverse excitations in the instability of bose-einstein condensates moving in optical lattices. *Phys. Rev. A*, 70:043625, 2004.

[82] O. Morice, Y. Castin, and J. Dalibard. Refractive index of a dilute bose gas. *Phys. Rev. A.*, 51:3896, 1995.

[83] O. Morsch, J. H. Müller, M. Cristiani, D. Ciampini, and E. Arimondo. Bloch oscillations and mean-field effects of bose-einstein condensates in 1d optical lattices. *Phys. Rev. Lett.*, 87:140402, 2001.

[84] O. Morsch and M. Oberthaler. Dynamics of Bose-Einstein condensates in optical lattices. *Reviews of Modern Physics*, 78:179, 2006.

[85] C. Orzel, AK Tuchman, ML Fenselau, M. Yasuda, and MA Kasevich. Squeezed States in a Bose-Einstein Condensate. *Science*, 291:2386, 2001.

[86] Yu. B. Ovchinnikov, J. H. Müller, M. R. Doery, E. J. D. Vredenbregt, K. Helmerson, S. L. Rolston, and W. D. Phillips. Diffraction of a released bose-einstein condensate by a pulsed standing light wave. *Phys. Rev. Lett.*, 83:284, 1999.

[87] B. Paredes, A. Widera, V. Murg, O. Mandel, S. Fölling, I. Cirac, G.V. Shlyapnikov, and T.W. Hänsch. Tonks- Girardeau gas of ultracold atoms in an optical lattice. *Nature*, 429:277, 2004.

[88] A. S. Parkins and D. F. Walls. The physics of trapped dilute-gas Bose-Einstein condensates. *Phys. Rep.*, 303:1, 1997.

[89] P. Pedri, L. Pitaevskii, S. Stringari, C. Fort, S. Burger, F. S. Cataliotti, P. Maddaloni, F. Minardi, and M. Inguscio. Expansion of a coherent array of bose-einstein condensates. *Phys. Rev. Lett.*, 87:220401, 2001.

[90] R. Peierls. The Momentum of Light in a Refracting Medium. *Proceedings of the Royal Society of London. Series A, Mathematical and Physical Sciences*, 347:475, 1976.

[91] P. Penfield and H. HausF. *Electrodynamics of Moving Media*. The MIT Press, Cambridge, Ma, 1967.

[92] C. J. Pethick and H. Smith. *Bose-Einstein Condensation in Dilute Gases*. Cambridge University Press, New York, 2002.

[93] H. Pu and P. Meystre. Creating macroscopic atomic einstein-podolsky-rosen states from bose-einstein condensates. *Phys. Rev. Lett.*, 85:3987, 2000.

[94] E. Rosencher. *Optoelectronics*. Cambridge University Press, Cambridge, UK, 2002.

[95] S. Sachdev. *Quantum phase transitions*. Cambridge University Press, Cambridge, 1999.

[96] J.J. Sakurai. *Modern Quantum Mechanics*. Addison Wesley, Redwood City, 1994.

[97] L. De Sarlo, L. Fallani, J. E. Lye, M. Modugno, R. Saers, C. Fort, and M. Inguscio. Unstable regimes for a bose-einstein condensate in an optical lattice. *Phys. Rev. A*, 72:013603, 2005.

[98] C. M. Savage and M. P. Das, editors. *Bose-Einstein Condensation*. World Scientific, London, 2000.

[99] D. Schneble, G. K. Campbell, E. W. Streed, M. Boyd, W. Ketterle, and D. E. Pritchard. Raman amplification of matter waves. *Phys. Rev. A*, 69:041601(R), 2004.

[100] D. Schneble, Y. Torii, M. Boyd, E. Streed, D. E. Pritchard, and W. Ketterle. The onset of matter-wave amplification in a superradiant bose-einstein condensate. *Science*, 300:475, 2003.

[101] Y. Schneble, D. Torii, M. Boyd, , E. W. Streed, D. E. Pritchard, and W. Ketterle. The onset of matter-wave amplification in a superradiant bose-einstein condensate. *Science*, 300:475, 2003.

[102] R. G. Scott, A. M. Martin, T. M. Fromhold, S. Bujkiewicz, F. W. Sheard, and M. Leadbeater. Creation of solitons and vortices by bragg reflection of bose-einstein condensates in an optical lattice. *Phys. Rev. Lett.*, 90:110404, 2003.

[103] A. Smerzi, A. Trombettoni, P. G. Kevrekidis, and A. R. Bishop. Dynamical superfluid-insulator transition in a chain of weakly coupled bose-einstein condensates. *Phys. Rev. Lett.*, 89:170402, 2002.

[104] Y. Sortais, S. Bize, M. Abgrall, S. Zhang, C. Nicolas, C. Mandache, P. Lemonde, P. Laurent, G. Santarelli, N. Dimarcq, et al. Cold atom clocks. *Physica Scripta*, 95:50, 2001.

[105] Dan Stamper-Kurn. *Peeking and poking at a new quantum fluid: Studies of gaseous Bose-Einstein condensates in magnetic and optical traps.* Ph.d., Massachusetts Institute of Technology, 1999.

[106] J. Stenger, S. Inouye, A. P. Chikkatur, D. M. Stamper-Kurn, D. E. Pritchard, and W. Ketterle. Bragg spectroscopy of a bose-einstein condensate. *Phys. Rev. Lett*, 82:4569, 1999.

[107] T. Stöferle, H. Moritz, C. Schori, M. Köhl, and T. Esslinger. Transition from a Strongly Interacting 1D Superfluid to a Mott Insulator. *Phys. Rev. Lett.*, 92:130403, 2004.

[108] T. Stöferle, H. Moritz, C. Schori, M. Köhl, and T. Esslinger. Transition from a strongly interacting 1d superfluid to a mott insulator. *Phys. Rev. Lett.*, 92:130403, 2004.

[109] K. E. Strecker, G. B. Partridge, A. G. Truscott, and R. G. Hulet. Formation and propagation of matter-wave soliton trains. *Nature (London)*, 417:150, 2002.

[110] E. W. Streed, A. P. Chikkatur, T.L. Gustavson, M. Boyd, Y. Torii, D. Schneble, G. K. Campbell, D. E. Pritchard, and W. Ketterle. Large atom number bose-einstein condensate machines. *Rev. Sci. Instr.*, 77:023106, 2006.

[111] Erik W. Streed. ^{87} *Rubidium Bose-Einstein condensates: Machine Construction and Quantum Zeno Experiments*. Ph.d., Massachusetts Institute of Technology, 2006.

[112] B. Taylor. Determining the avogadro constant from electrical measurements. *Metrologia*, 31:181, 1994.

[113] M. Theis, G. Thalhammer, K. Winkler, M. Hellwig, G. Ruff, R. Grimm, and J.H. Denschlag. Tuning the Scattering Length with an Optically Induced Feshbach Resonance. *Phys. Rev. Lett.*, 93:123001, 2004.

[114] B. L. Tolra, K. M. OHara, J. H. Huckans, W. D. Phillips, S. L. Rolston, and J. V. Porto. Observation of Reduced Three-Body Recombination in a Correlated 1D Degenerate Bose Gas. *Phys. Rev. Lett.*, 92:190401, 2004.

[115] C. Tozzo, M. Kramer, and F. Dalfovo. Stability diagram and growth rate of parametric resonances in bose-einstein condensates in one-dimensional optical lattices. *Phys. Rev. A*, 72:023613, 2005.

[116] M. Trippenbach, Y. B. Band, M. Edwards, M. Doery, P. S. Julienne, E. W. Hagley, L. Deng, M. Kozuma, K. Helmerson, S. L. Rolston, and W. D. Phillips. Coherence properties of an atom laser. *J. Phys. B*, 33:47, 2000.

[117] E. G. M. van Kempen, S. J. J. M. F. Kokkelmans, D. J. Heinzen, and B. J. Verhaar. Interisotope determination of ultracold rubidium interactions from three high-precision experiments. *Phys. Rev. Lett*, 88:093201, 2002.

[118] J.M. Vogels, K. Xu, and W. Ketterle. Generation of macroscopic pair-correlated atomic beams by four-wave mixing in bose-einstein condensates. *Phys. Rev. Lett.*, 89:020401, 2002.

[119] D. S. Weiss, B.C. Young, and S. Chu. Precision measurement of the photon recoil of an atom using atomic interferometry. *Phys. Rev. Lett*, 70:2706, 1993.

[120] A. Wicht, J. M. Hensley, E. Sarajlic, and S. Chu. A preliminary measurement of the fine structure constant based on atom interferometry. *Physica Scripta*, 102:82, 2002.

[121] B. Wu and Q. Niu. Landau and dynamical instabilities of the superflow of bose-einstein condensates in optical lattices. *Phys. Rev. A*, 64:061603, 2001.

[122] R. Wynar, R. S. Freeland, D. J. Han, C. Ryu, and D. J. Heinzen. Molecules in a bose-einstein condensate. *Science*, 287:1016, 2000.

[123] K. Xu, Y. Liu, D. E. Miller, J. K. Chin, W. Setiawan, and W. Ketterle. Observation of strong quantum depletion in a gaseous bose-einstein condensate. *Phys. Rev. Lett*, 96:180405, 2006.

[124] Kaiwen Xu. *Effects of Interaction in Bose-Einstein Condensates*. Ph.d., Massachusetts Institute of Technology, 2006.

[125] Y. Zheng, M. Kostrun, and J. Javanainen. Low-acceleration instability of a bose-einstein condensate in an optical lattice. *Phys. Rev. Lett.*, 93:230401, 2004.